

AD-A206 626

SEMICONDUCTOR SURFACE EMITTING LASER DIODES

DRAFT FINAL REPORT

MARCH 30, 1989



Contract Number: N00014-87-C-0492

For:

OFFICE OF NAVAL RESEARCH
Department of the Navy
800 N. Quincy Street, Alington, Virginia 22217

By:

S. C. Wang and T. G. Dziura

Approved for Public Release. Distribution
Unlimited.
Per Dr. Hershel S. Pilloff, ONR/Code 1112LO

LOCKHEED MISSILES & SPACE COMPANY, INC.
Research and Development Division
3251 Hanover Street, Palo Alto, California 94304

89 4 03 086

CONTENT

Chapter 1	Introduction	1
Chapter 2	Technical concepts and approaches	3
2.1	Key design considerations	3
2.2	Basic surface emitting laser configurations	4
Chapter 3	Progress	6
3.1	Device design and fabrication	6
3.1.1	DFB type SEL structure	
3.1.2	Fabrication procedure	
3.2	Laser performance characterization	9
3.2.1	Device test apparatus	
3.2.2	Electrical characteristics	
3.2.3	Near- and far-field radiation patterns	
3.2.4	L-I characteristics	
3.2.5	Emission spectrum	
3.3	Laser array development	16
3.3.1	Array design and configuration	
3.3.2	Array performance	
3.4	Theoretical modeling and analysis	19
3.4.1	Bloch wave analysis of SELs	
3.4.2	Discrete propagation model for DFB and DBR lasers	
Chapter 4	Summary and discussion	27
Chapter 5	Recommendations	28
Appendix		



Availability Codes	
Dist	Avail and/or Special
A-1	



per cal

CHAPTER 1 INTRODUCTION

The conventional edge emitting laser diode uses either a single-stripe or multiple stripe structure consisting of an active layer in a plane parallel to the semiconductor surface; two cleaved facets, functioning as laser cavity mirrors, are perpendicular to this active layer. It is relatively difficult to fabricate and diagnose in situ, and only one-dimensional laser arrays have been monolithically fabricated. The surface emitting laser (SEL), on the other hand, utilizes both surfaces of the wafer as laser mirrors and the light output is perpendicular to the wafer plane. This makes planar fabrication and diagnosis easier, and more importantly, allows for two-dimensional (2-D) monolithic integration and array formation. This 2-D SEL array can be scaled in number and size while maintaining a high filling factor. The SEL array diodes can also be individually addressed and controlled, and the output beam can be easily accessed from both the front and back surfaces of the wafer. These features are very important and desirable when a large array of coherent emission semiconductor lasers is needed. — ()

In addition, the SEL is typically very short in active length in comparison to an edge emitting laser diode (about 10 μm versus 200 to 300 μm). As a result, single mode or single frequency operation can be achieved relatively easily from SELs. Because the optical cavity is small, the photon round trip time is short (about 0.2 psec), making very high frequency modulation possible. Because of the large emitting area of SELs (typically 10 μm diameter, as compared with 1 μm in conventional edge emitting laser diodes), the output beam divergence of a SEL is expected to be smaller than that of an edge emitting laser. These are all favorable factors for application in high data rate optical communication and signal processing.

Although the SEL promises to be very attractive for 2-D arrays and for various applications that require fast response and single frequency operation, the SEL device technology is still relatively young and not fully established. So far most of the SEL device development effort has been conducted in Japan by K. Iga and coworkers, and few research efforts had been conducted in the United States until recently, after our research team at LMSC began development work in collaboration with the University of California at Berkeley.

The SEL structure reported by the Japanese group utilized a vertical junction similar to that in edge emitting laser diodes, without any transverse current confinement and with relatively poor optical confinement. As a result, the device exhibited a very high threshold current (about a few hundred mA). In addition, the laser cavity is formed by an etched mirror and ring electrode, which has relatively poor optical quality. Therefore, new and novel device structures and configurations are needed to improve the SEL performance both in output efficiency and threshold current.

The realization of a 2-D SEL array by the Japanese group was limited to a 2 x 2 array with only 75 percent yield, and a larger SEL array has so far not been demonstrated. In order to prove the concept that SELs can be easily scaled into a 2-D array, a research effort in this area is needed.

The main objective of this program, therefore, is to develop a novel SEL design and structure with improved performance characteristics, and to demonstrate the feasibility of scaling the SEL to a 2-D array. This report summarizes accomplishments and progress toward this objective during the previous 18-month period. Chapter 2 describes the technical concepts and approaches we have taken in designing and fabricating the SEL. Chapter 3 presents the results in device design and fabrication, laser characterization, array development and theoretical analysis. Chapter 4 summarizes the overall progress and accomplishments and discusses the technical issues remaining to be solved. In the last chapter, we recommend a follow-on program that allows these remaining technical issues to be fully investigated. This effort will bring SEL technology to a more mature stage, and allow its true potential and practicality to be further explored.

CHAPTER 2 TECHNICAL CONCEPTS AND APPROACHES

2.1 Key design considerations

The two prerequisites for efficient operation of a laser diode are good optical and current confinement. These two features have been successfully implemented in the conventional edge emitting laser diodes. However, the SEL diodes reported so far do not provide either type of confinement. Therefore a special structure must be devised to implement these confinement features. We chose a transverse buried heterojunction structure, in which the current is injected laterally into the active region. This structure not only improves the current and optical confinement but also provides a longer and more uniform active length to assure higher gain and power output.

Another consideration for this new transverse junction SEL is the optical cavity structure. The need for a low loss optical cavity is quite evident from a threshold gain calculation. The threshold gain of a laser is given by

$$g_{th} = \alpha + (1/L)\ln(1/R)$$

where α is the internal losses due to the free carrier absorption and scattering, L is the active-layer length, and R is the reflectivity of the laser cavity (assume both facets have equal reflectance). For a conventional edge emitting laser diode of $L = 250 \text{ } \mu\text{m}$, $R = 0.32$, and $a = 10 \text{ cm}^{-1}$, the threshold gain is estimated to be about 60 cm^{-1} . To keep g_{th} low in an SEL with a short active length, we require a cavity mirror reflectance of $R \sim 0.95$ (cavity length $L = 10 \text{ mm}$, $g_{th} = 60 \text{ cm}^{-1}$, and same internal losses).

To achieve this high a mirror reflectance in the SEL cavity, two approaches were explored. One approach was to form alternate layers of GaAs and AlGaAs material with quarter-wavelength thickness within the laser active region, or on the top and bottom portion of the laser with the active region in between. Another approach was to deposit dielectric coatings on the output end of the SEL instead of the alternate quarter-wavelength GaAs/AlGaAs multilayer. Either approach can in theory form a laser cavity with a reflectivity as high as 99 percent.

For SELs, it is extremely important that the lasers can be made of uniform quality in layer thickness, doping concentration, and cavity length. The first two requirements can be met, and the third requirement can be facilitated by using either the molecular beam epitaxy (MBE) or metal organic chemical vapor deposition (MOCVD) growth technique. Uniform cavity length is achieved by using a selective etching technique that stops at a clearly defined GaAs/AlGaAs interface. These approaches will assure formation of a mirror-like flat surface upon which dielectric coatings can be deposited to give superior mirror quality.

2.2 Basic surface emitting laser configurations

Based on the design considerations discussed previously, we conceived a SEL utilizing a transverse buried heterojunction (TBH) structure with a vertical laser cavity. Two basic SEL configurations of this TBH structure are shown schematically in Fig. 1. One is a distributed feedback (DFB) type and another is a distributed Bragg reflector (DBR) type resonator configuration.

The DFB type SEL has a smaller gain volume that can operate at low threshold current. It also requires no dielectric mirror and has good mode selectivity. However this structure can have nonuniform spatial gain and its performance is relatively sensitive to the DFB layer thickness. The DBR type SEL on the other hand is easy to design, is less sensitive to fluctuations in layer thickness, and it can be adjusted for maximum gain or output by varying the active region volume. It also has a more uniform spatial gain profile. However, the DBR structure requires a high reflectivity dielectric mirror coating or multiple layers of GaAs/AlGaAs, and typically needs a high operating current.

We chose the DFB type structure as the main approach during this project because of the encouraging results obtained from this structure earlier, and because of the relative simplicity in device fabrication. The detailed design and fabrication process of this DFB type SEL and its array are described in the following section.

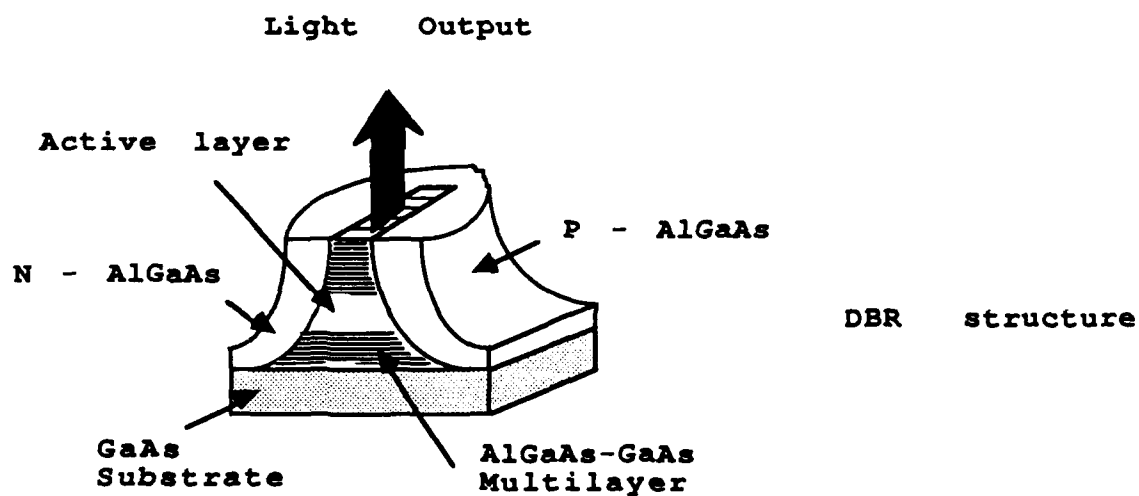
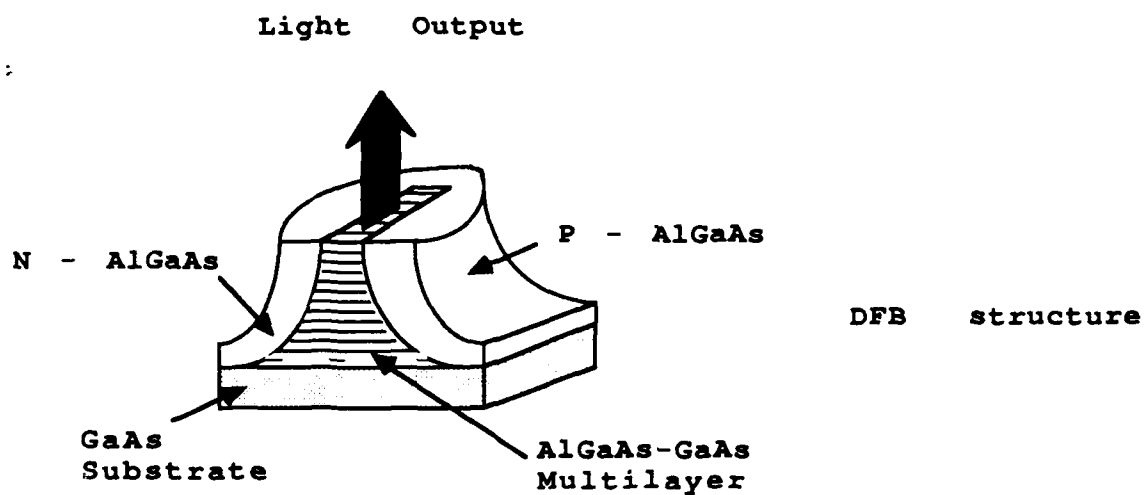


Figure 1. Schematic diagram of DFB and DBR surface emitting laser

CHAPTER 3 PROGRESS

3.1. Device design and fabrication

The successful fabrication of any new device usually requires utilizing well-developed processing technology but often involves combining several processing steps in a new sequence. The initial processing steps must be compatible with and must not be affected by the processing to follow. Because a semiconductor laser requires the synergistic action of electronic and optical structures, the demands on performance and on the nature of the fabrication steps is even greater. The following sections describe the complex series of steps required to fabricate our SELs, discuss the issues involved in our choice of electro-optical structure, and present the results from our fabricated samples.

3.1.1. DFB type SEL structure

As we described previously, the main SEL structure we developed during this project is a DFB type cavity as shown in Fig. 1. In this case, the performance of the optical cavity is determined by the sequencing of the epitaxially grown multilayer. The effective reflectance of the cavity structure increases with the number of pairs of layers, and with the refractive index difference between the two layers within a pair. Each of the layers is nominally one quarter wave of optical thickness at the design (Bragg) wavelength. The resonator loss is least at the Bragg mode, and increases for wavelengths greater or less than this mode. Since a symmetric DFB structure with a periodic real refractive index modulation will not lase precisely at the Bragg wavelength, an asymmetry must be introduced into the resonator to induce oscillation of the Bragg mode. The "phase shift layer", which in our structure is an additional quarter-wave layer of GaAs located 20 pairs from the output facet, serves to provide this asymmetry. It forces single frequency oscillation at the design Bragg wavelength, and also increases the ratio of forward to backward emitted power.

We chose an index guided waveguide structure for confinement of the optical mode. Index guided structures have several advantages over gain guided structures for laser diodes, including a lower threshold current, a sharper turn-on at threshold, and a more stable near and far field radiation pattern. Most other SEL designs (with the exception of in plane surface emitters relying on second order distributed Bragg reflection to eject the beam perpendicular to the wafer plane) have utilized gain guiding for optical mode confinement. The buried heterojunction structure created by the LPE-regrowth process serves to provide this real refractive index waveguiding.

Finally, we chose a transverse buried heterostructure (TBH) type of pn junction for electron and hole confinement. This type of charge carrier control has been used quite successfully in edge emitting lasers, and it is easy in principle to implement. The biggest advantage a TBH type of junction for SELs is its compatibility with other planar processing technology.

3.1.2. Fabrication procedure

The starting point for the fabrication of a SEL is the epitaxially grown multilayer structure. MOCVD was used to deposit the alternating layers of GaAs and $\text{Al}_{0.3}\text{Ga}_{0.7}\text{As}$ on a semi-insulating GaAs substrate. The wafer surface was then masked and a wet chemical etch was applied to create a mesa. This mesa forms the core of the optical waveguide as well as the active region of the laser. The wet etch typically results in a tapered profile. The mesa as shown in the scanning electron microscope (SEM) photo (Fig. 2) is about 4 mm by 20 mm, with the smaller dimension increasing to about 12 mm at the base .

Liquid phase epitaxy (LPE) is then used to regrow an n-type $\text{Al}_{0.4}\text{Ga}_{0.6}\text{As}$ cladding layer around the mesa, completing the optical waveguide structure. The silicon nitride on the top of the mesa acts as a mask for the regrowth, allowing selective epitaxy to occur only around the islands. Another nitride mask is then applied, and a lateral pn junction is formed by zinc diffusion through an opening in the n-type cladding region. The diffusion is timed so that the diffusion front stops in the active region, providing for carrier confinement in the waveguide core.

In the final steps, ohmic contacts are applied; Au/Cr is used to contact the p side of the junction, and Au-Ge-Ni is used for the n contact. The wafer is diced into chips roughly 1.5 mm on a side, and the individual chips are mounted in a chip carrier with either a thermal epoxy or indium solder. Finally, ultrasonically bonded aluminum wire is used to connect the chip carrier pads to the bonding pads on the laser array.

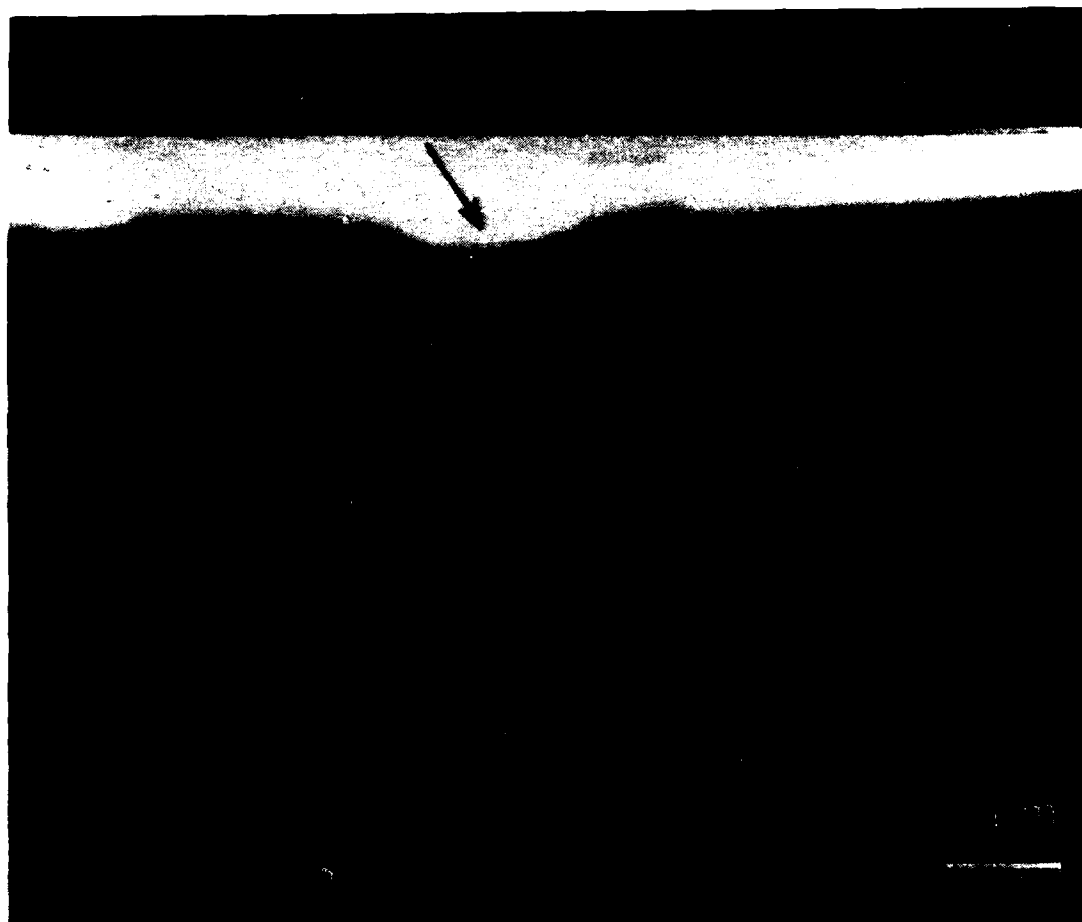


Figure 2. SEM picture of the cross-section of a DFB type SEL

Two fabrication issues should be discussed at this time. The proper timing of the zinc diffusion for the p side of the junction is rather crucial to the successful performance of the laser. The diffusion front must stop in the center of the multilayer, so that the carriers are confined in the center of the waveguide core and maximum gain is provided to the optical mode. The position of the zinc front varies from laser to laser, depending on the local wafer temperature and the local crystal quality. The poor rectifying performance of some of the lasers may be attributable to the diffusion front stopping on the interface between the multilayer and the regrown AlGaAs cladding, increasing the likelihood that carriers will leak through the junction via interfacial defects.

A second issue is the problem we have encountered with the adhesion of the ohmic contact metallization. This is caused by two competing requirements; the window in the silicon nitride mask must be small to restrict the area of the zinc diffusion, but must be large enough to provide a sufficient area for adhesion to the GaAs surface (the adhesion to the nitride is poor). We expect to eliminate this problem with a different choice of contact metallurgy. These two issues also affect the fabrication yield of our SELs and SEL array, leaving only a limited number of SEL array samples available for performance characterization.

3.2. Laser performance characterization

3.2.1. Device test apparatus

The first test that was performed on the newly fabricated SELs was to record the current versus voltage response (I-V) as a check of the quality of the pn junction and of the carrier confinement. A Tektronix curve tracer was used for this measurement. Next the near field radiation pattern and the optical output power versus current input (L-I) were recorded. A manual semiconductor probe station was useful for examining the near field at magnifications to 500x; we modified a Vickers Instruments microscope to allow probe testing of our SELs and SEL array samples, visual inspection of the near field pattern, and recording of the L-I data. This microscope had an accessory that utilized shearing techniques to measure image features with roughly 1 μm accuracy and was used to make dimensional measurements on the fabricated samples. The near field pattern was recorded using an RCA infrared vidicon with an image digitizer.

Lastly, the spectral emission profile was measured for selected lasers. A McPherson monochromator was used in combination with a cooled germanium pin detector (North Coast Model EO-817L). The germanium detector was chosen for its low noise equivalent power as well as reasonably flat spectral response near 900 nm. A helium cryostat was also used to take temperature-dependent data.

3.2.2. Electrical characteristics

For all the devices fabricated on a wafer, the uniformity in the I-V response was generally quite good. A typical example of the DC electrical response is shown in Fig. 3. The turn-on voltage is about 1.3-1.5 volts, and the breakdown voltage is about -7 volts. This result indicates that the pn junction is formed properly in the device. However, some junctions exhibit a large amount of leakage, and others show no rectifying behavior at all. We have also observed a long term degradation of the pn junction and laser performance; this may be caused by migration of defects into the active region.

3.2.3. Near and far field radiation patterns

The refractive index difference between the active region and cladding layer of our SEL waveguide structure is about 0.12 and therefore should be more than adequate for providing strong mode confinement. This is exemplified by a typical well-confined near field radiation pattern as shown in Fig. 4. All of the lasers that we examined have exhibited this strongly confined emission pattern, which also indicates that the TBH-type pn junction is providing good carrier confinement. The light emission is restricted to the rectangular surface emitting area in both directions.

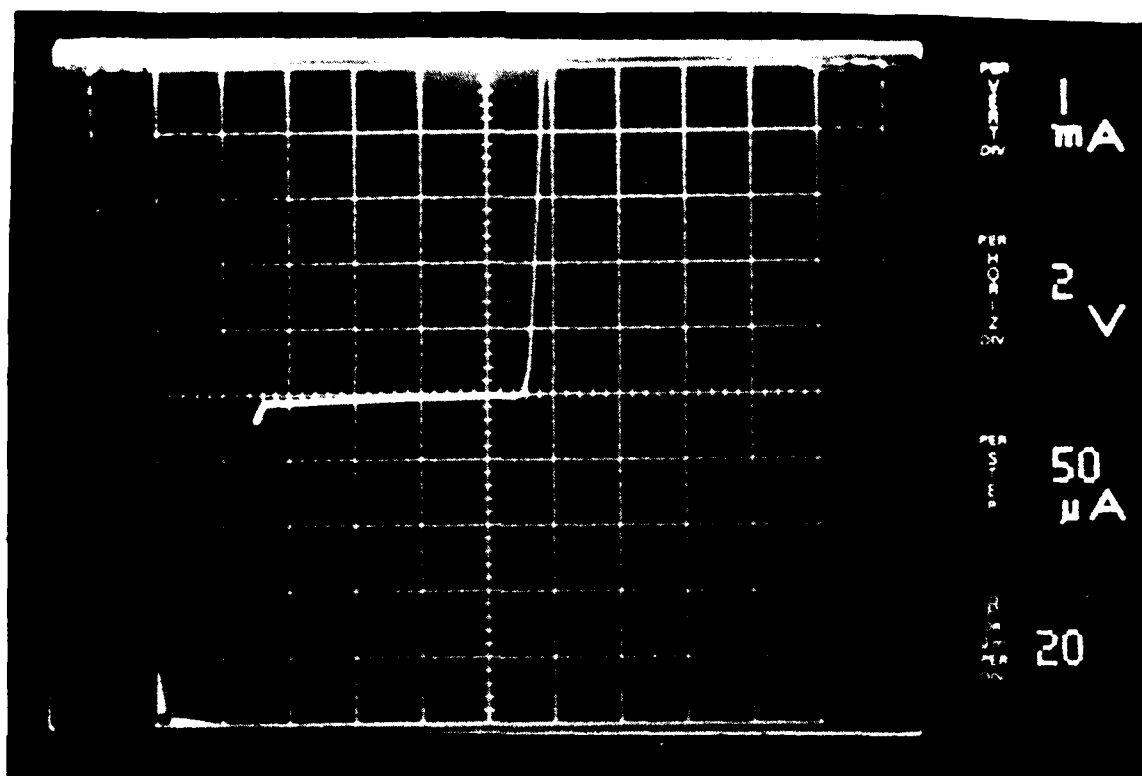


Figure 3. Typical I-V response of the SEL diode

The far field emission pattern observed by a video camera shows a near circular pattern with a divergence angle of about 8 degrees as shown in Fig. 5. However, some laser diodes show a quite different far field when measured with a rotating slit method. The emission is quite broad in extent, which could be due to the strong spontaneous emission component observed at high operating currents.

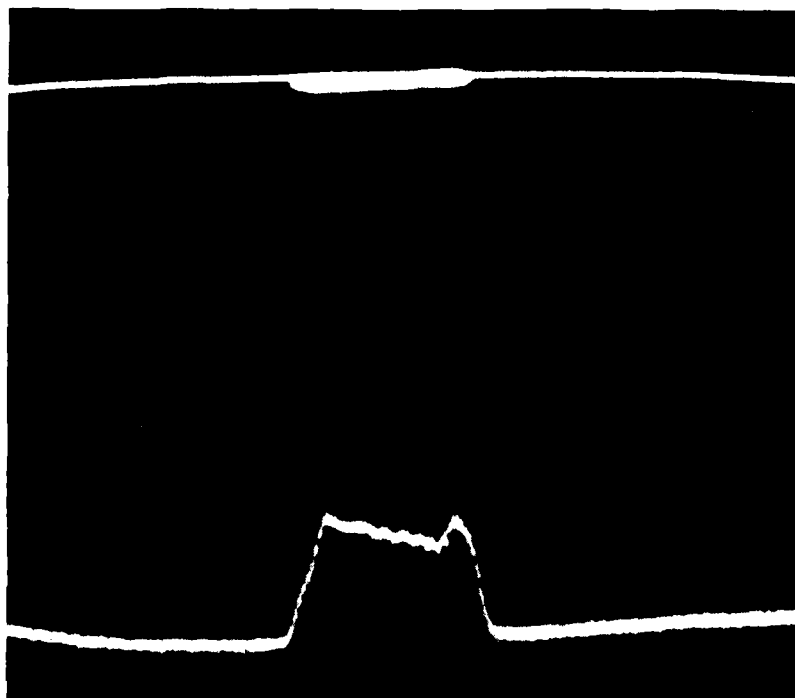


Figure 4. Typical near-field emission pattern of SEL

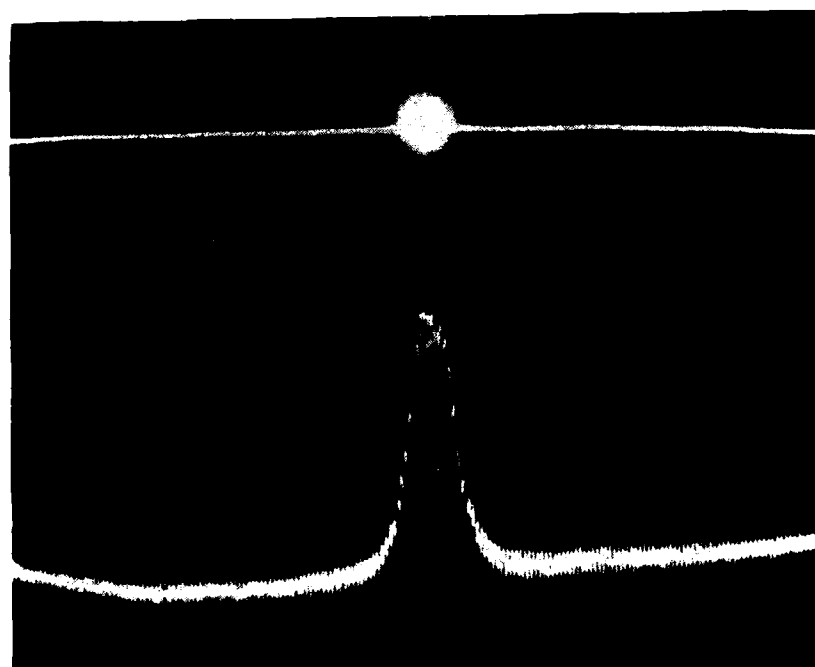


Figure 5. Typical far-field emission pattern of SEL

3.2.4. L-I characteristics

For semiconductor lasers of any type the variation in optical performance from one laser to the next can be rather large. This is caused by the differences in crystal quality, layer uniformity, processing steps, and in the quality of heat-sinking. As a result the SEL diodes exhibited a broad range of optical performance. We show in Fig. 6 a set of L-I curves for an arbitrarily chosen group of lasers. We have measured a best case output efficiency just under 1%, and have observed powers as high as 0.5 mW from many emitters. In measurements of the polarization of the output from several lasers, we have observed only a slight difference in the relative power in the two orthogonal polarization directions. This result is not completely unexpected; Because the equivalent active layer thickness of the SEL is about 5 mm, which is well within the regime in which TE and TM mode reflectances are comparable. It is possible, however, that residual birefringence could act to select one preferable polarization.

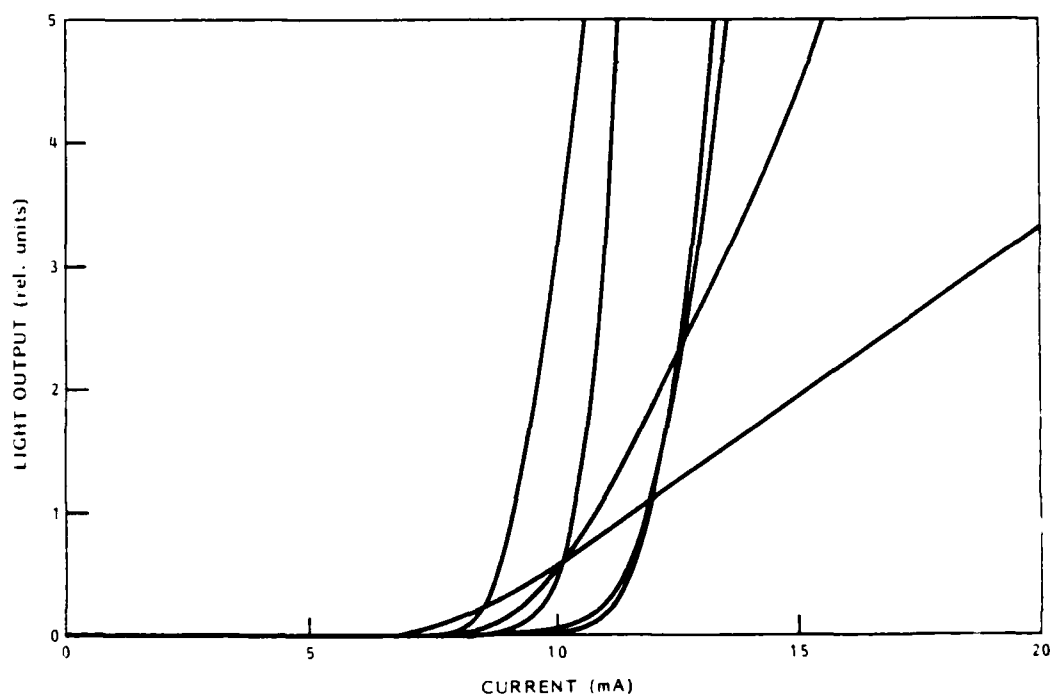


Figure 6. Typical L-I curves of SELs

The temperature dependence of the L-I response has also been measured and the result is shown in Fig. 7. The "characteristic temperature" is a quantity that is usually quoted to quantify the performance of the laser at various temperatures, where it is assumed that the threshold current $I_{th} \sim \exp(T/T_0)$ (T is the temperature and T_0 is the characteristic temperature). From this data we determine that $T_0 \approx 190K$.

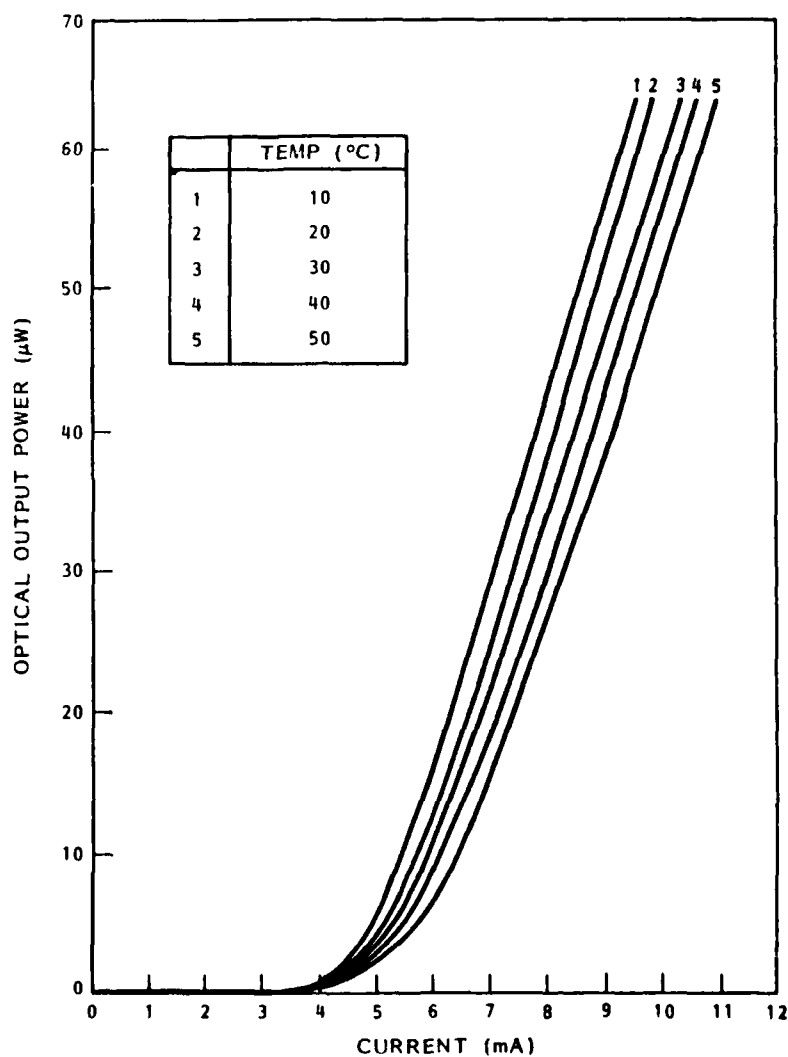


Figure 7. Temperature dependence of L-I response

3.2.5. Emission spectrum

The spectral emission from these lasers has several components as shown in Fig. 8. At very low currents (typically just a few mA) a narrow peak appears above the background, centered at about 884 nm. This mode corresponds to the fundamental Bragg mode as designed, and it grows in relative intensity until much higher currents are reached (50-100 mA), when the modes at shorter wavelength begin to compete for the gain. The linewidth of this mode is somewhat broader than expected, and it is difficult if not impossible to diagnose the reason for this broad emission width. Possible explanations include thickness errors in the epitaxially grown multilayer as well as carrier-induced shifts in the refractive index, which both degrade the finesse of the resonator, thus broadening the emission linewidth.

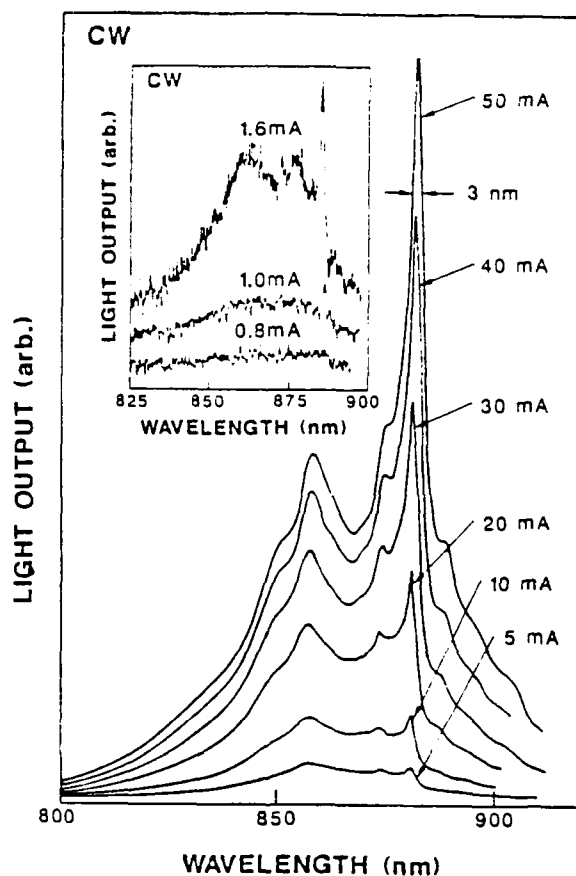


Figure 8. Typical SEL emission spectrum

Additional modes appear at shorter and longer wavelengths; the theoretical model described below predicts the positions of these longitudinal modes with reasonable accuracy. From an examination of the axial intensity profile of all the modes it seems likely that these modes can contribute to the output because they can utilize the spatial gain that is unused by the main Bragg mode. This envelope spatial hole burning effect is predicted to be less severe in distributed Bragg reflector (DBR) lasers.

3.3. Laser array development

3.3.1. Array design and configuration

Because of the planar structure and surface emission of SELs, formation of 1-D and 2-D arrays is relatively simple to accomplish; a 3×3 SEL array might look like that shown in Fig. 9. By proper design of the photolithographic masks, the SEL array can be fabricated using the same sequence of processing steps that is used in the fabrication of individual SELs.

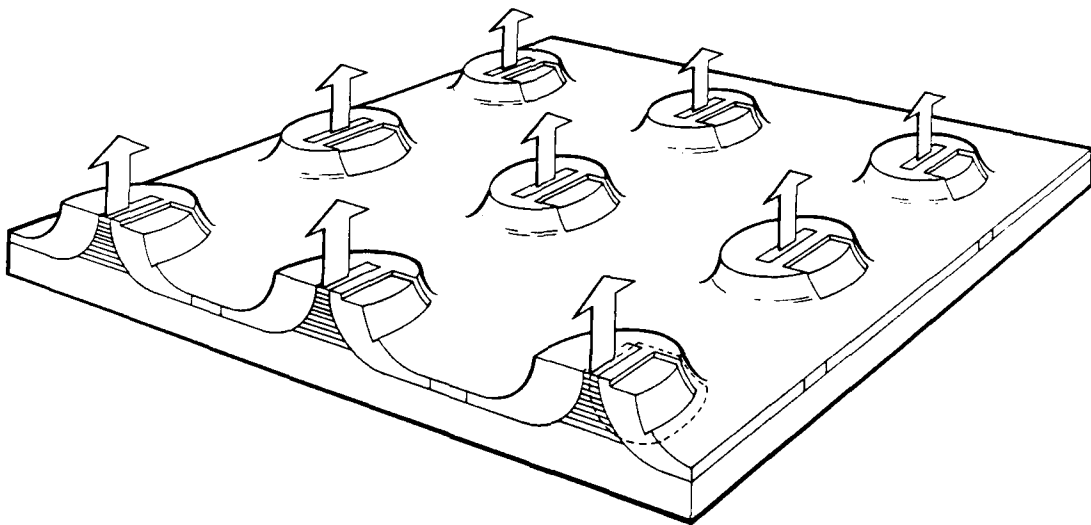


Figure 9. Schematic of a 3×3 SEL array configuration

Using the DFB type SEL diode structure described previously, we fabricated a number of arrays with 1-D and 2-D configurations. The array chip was mounted on a standard multiple pin chip carrier for testing as shown in Fig. 10.



Figure 10. Picture of a SEL array mounted on a chip carrier

Fig. 11 shows the photomicroscopic picture of a 2-D SEL array with 6 x 16 elements on a GaAs chip of about 2 mm x 2 mm. The light emitting area is adjacent to the shiny rectangular region, which is a gold electrode pad. The spacing between each SEL element is about 100 μ m, limited by the electrode pad size (about 80 μ m by 80 μ m). The pad size was chosen for reasons of reliability; a smaller pad delaminates from the substrate during ultrasonic wire bonding. The light emitting area varies from 3 mm x 15 mm to 3 mm x 20 mm.

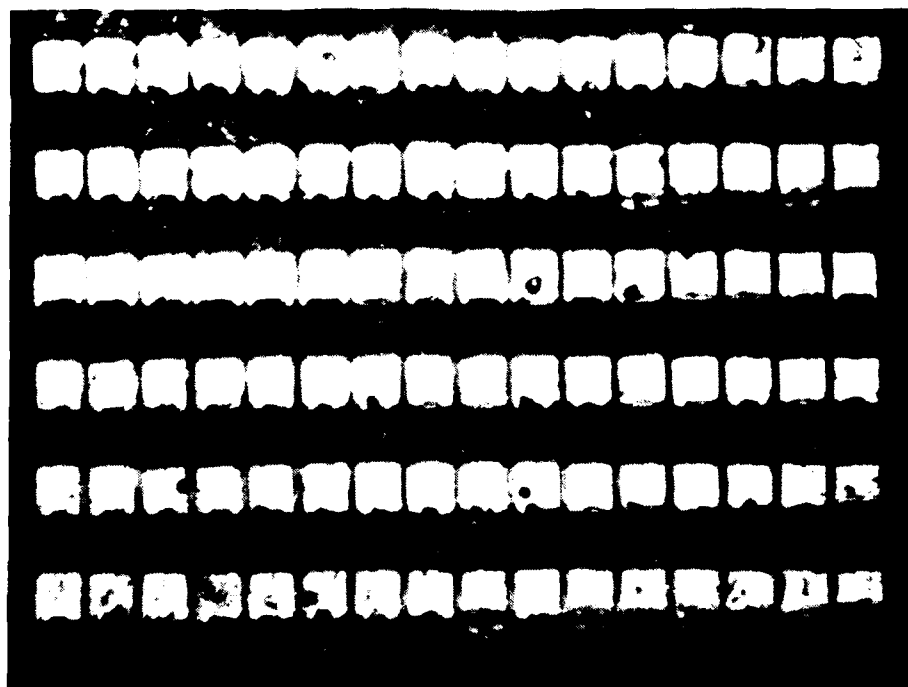


Figure 11. Photomicroscopic view of a 6 x 16 SEL array

3.3.2. Array performance

Fig. 12 shows the emission pattern of the SEL array under cw operation. Because of the different emission areas of SEL elements in the array and possible nonuniformity in the wafer fabrication process, the threshold current for each SEL varies widely between a few mA to a few tens of mA. Therefore, the array emission pattern was taken by adjusting the driving current of each SEL to provide a nearly uniform emission intensity.

As can be seen from the emission pattern, the overall array has a fairly good yield with about 95% of the SELs in the array emitting radiation, and only a few SELs out of about a hundred do not emit light. The non-emitting devices often exhibited no rectifying behavior, indicating that the lack of light emission was due to little or no carrier confinement. The carrier confinement is strong in all lasers that do emit light, as evidenced by the tight optical mode confinement.

This result is very encouraging for future array development. Additional improvements in array uniformity will be forthcoming as the wafer quality and fabrication technology are refined.

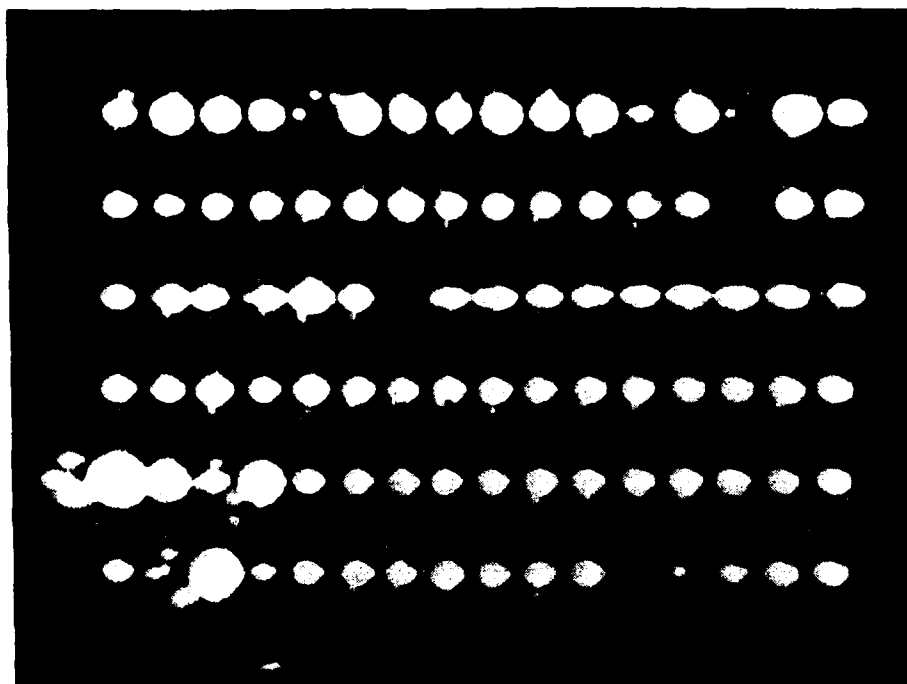


Figure 12. Emission pattern of a 6 x 16 SEL array

3.4. Theoretical modeling and analysis

In conjunction with the experimental work an effort of theoretical modeling was undertaken. The objective was twofold: (1) to aid in interpreting the experimental data on fabricated SELs, and (2) to provide guidance in the design of the laser optical resonator. An eigenmode theory based on a Bloch wave expansion of the electric field was developed and applied to the analysis of DFB type SELs. This treatment was restricted to the below threshold regime. An alternative formalism, using thin film discrete propagation techniques, was also constructed. This model is capable of describing strong mode coupling between the counter-propagating waves in the resonator as well as treating gain saturation and laser operation above threshold. These models are described in detail in the sections that follow.

3.4.1. Bloch wave analysis of surface emitting lasers

The distributed feedback laser can be described quite simply if one assumes that the solutions of Maxwell's equations for an infinite periodic structure approximate the solutions for the finite laser structure. The laser electric field must satisfy the Helmholtz equation

$$\frac{d^2 E(z, \lambda)}{dz^2} - [g(z, \lambda) - i \beta(z, \lambda)]^2 E(z, \lambda) = 0 \quad (1-1)$$

where $E(z, \lambda)$ is the electric field, g is the material gain coefficient, and β is the propagation constant. If the gain and refractive index are assumed periodic with period Λ ,

$$g(z, \lambda) - i \beta(z, \lambda) = g_0(\lambda) - i \beta_0(\lambda) + \sum_{q=-\infty}^{q=\infty} (g_q(\lambda) - i \beta_q(\lambda)) \exp(i 2 q \pi z / \Lambda) \quad (1-2)$$

then the solutions for the electric field are of the Floquet-Bloch type:

$$E(z) = A(z) \exp(\Gamma z) + B(z) \exp(-\Gamma z) \quad (1-3)$$

where

$$\Gamma = G - iK \quad (1-4)$$

G is the "effective gain" and K is the "effective propagation constant," and $A(z)$ and $B(z)$ are periodic functions of z . $A(z)$ corresponds to a forward propagating mode and $B(z)$ corresponds to a backward propagating mode. When the condition for Bragg reflection is satisfied, i.e. when β_0 is approximately K_b (the Bragg propagation constant), the waves scattered at each interface between dissimilar media constructively interfere and the overall reflectivity becomes high. If we further expand A and B in a Fourier series

$$A(z, \lambda) = A_0 + \sum_{q=-\infty}^{q=\infty} A_q(\lambda) \exp(i2q\pi z/\Lambda) \quad (1-5)$$

$$B(z, \lambda) = B_0 + \sum_{q=-\infty}^{q=\infty} B_q(\lambda) \exp(i2q\pi z/\Lambda) \quad (1-6)$$

we can derive first order expressions for the amplitude components

$$A_{+p}(\lambda) = \frac{iK_{+p}}{G + g_0 + i(\delta + \delta_{\text{eff}})} A_0 \quad (1-7)$$

$$B_{-p}(\lambda) = \frac{iK_{-p}}{G + g_0 + i(\delta + \delta_{\text{eff}})} B_0 \quad (1-8)$$

where

$$\delta = K_b - \beta_0(\lambda) \quad (1-9)$$

$$\delta_{\text{eff}} = K_b - K \quad (1-10)$$

$$K_{+p} = \beta_{+p} + ig_{+p} \quad (1-11)$$

$$K_{-p} = \beta_{-p} + ig_{-p} \quad (1-12)$$

We also obtain a characteristic equation

$$(G + i\delta_{\text{eff}})^2 = (g_0 + i\delta)^2 + K_{+p}K_{-p} \quad (1-13)$$

which is used to determine eigenmode solutions for the pair of quantities (G, δ_{eff}) . If we apply the above to our DFB surface emitter, we obtain the results shown in Fig.13, where G , δ_{eff} , and δ are plotted as a function of wavelength for the case when the material gain coefficient $g = 2000 \text{ cm}^{-1}$. It is seen that the effective gain is a maximum in the region of the Bragg wavelength, indicating that the structure is working properly to provide maximum feedback at the Bragg wavelength.

We have also used this model to predict the emission spectrum of the DFB type SEL. Briefly, the laser was modeled as a spontaneous emission-driven resonator; the formalism described above was used to determine the amount of wavelength-dependent feedback, and the spectral variation of the spontaneous emission power was included. As shown in Fig.14 the computed mode positions and the shift of emission wavelength with temperature agree quite well with the experimental data, but the estimate of the relative emission intensities is rather poor. This may be due to the linear nature of the model, which neglects gain saturation and is therefore applicable only below laser threshold. For analysis of laser emission properties above laser threshold we developed an alternative model described below.

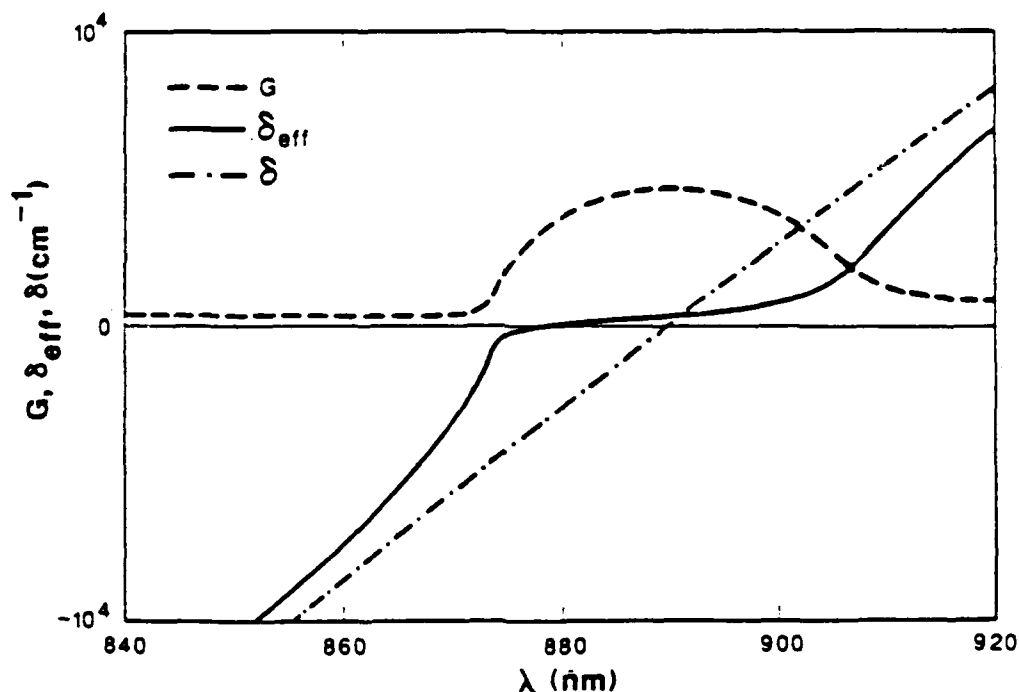


Figure 13. Wavelength dependence of G and δ_{eff}

3.4.2. Discrete propagation model for DFB and DBR lasers

Coupled mode theory is the standard approach to modelling distributed feedback (DFB) lasers, and it has proved to be useful in the first-order design of a variety of semiconductor laser structures. It should strictly be used to analyze edge-emitting lasers, since the coupled-mode propagation equations include an implicit assumption of weak interaction between the forward and backward travelling waves in the resonator. SELs operate in the strong coupling regime; typically the distributed feedback coefficient $K \sim 5000-10000 \text{ cm}^{-1}$ for surface emitters, and $K \sim 50 \text{ cm}^{-1}$ for edge emitters. Thus some loss in accuracy would ensue in applying the methods of coupled-mode theory directly to SELs. In order to take this strong-coupling effect into consideration and to include the effects of gain saturation, we have extended the discrete propagation techniques of Björk and Nilsson¹ and have used this model to analyze SELs with a DFB vertical cavity and with a distributed Bragg reflector (DBR) cavity. The methods of Ref. 1 are particularly amenable to computer calculation and well suited to analyzing resonators having a multilayer structure. They are also flexible enough to be used in cases involving facet reflections, phase shift layers, amplifying regions, and dielectric coatings.

The equations we used to model these lasers comprise two sets. The first set treats the free propagation of the forward and backward waves within a layer according to

$$A_i(z_i + l_i) = A_i(z_i) \exp[i\beta_i l_i + (1/2) g_i(A_i, B_i) l_i] \quad (2-1)$$

$$B_i(z_i + l_i) = B_i(z_i) \exp[-i\beta_i l_i - (1/2) g_i(A_i, B_i) l_i] \quad (2-2)$$

$$g_i(A_i, B_i) = g_0 / (1 + |A_i(z_i)|^2 + |B_i(z_i)|^2) \quad (2-3)$$

where A_i and B_i are the normalized forward and backward wave amplitudes in the i -th layer, z_i is the axial position of layer i , β_i is the propagation constant, l_i is the i -th layer thickness, and g_i and g_0 are the saturated and unsaturated intensity gain coefficients respectively. The fields are propagated across an interface between layers i and j using the second equation set

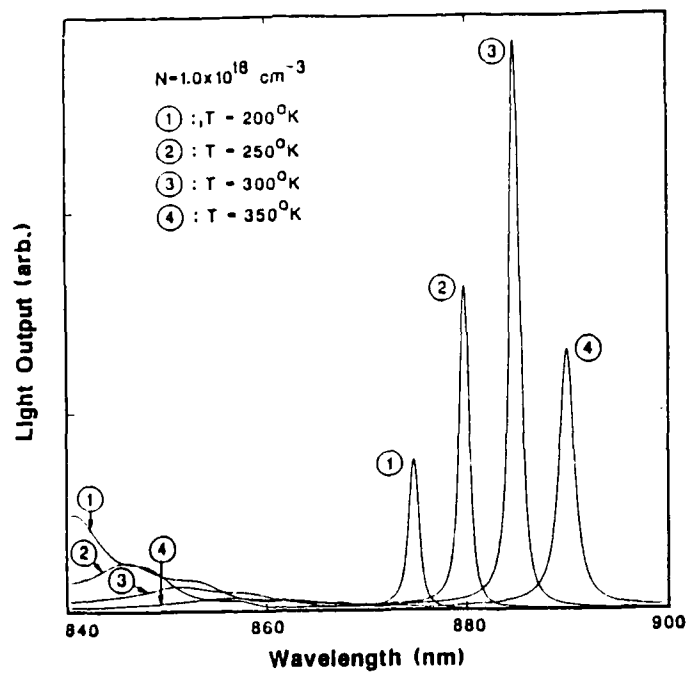


Figure 14. Temperature dependence of emission spectrum

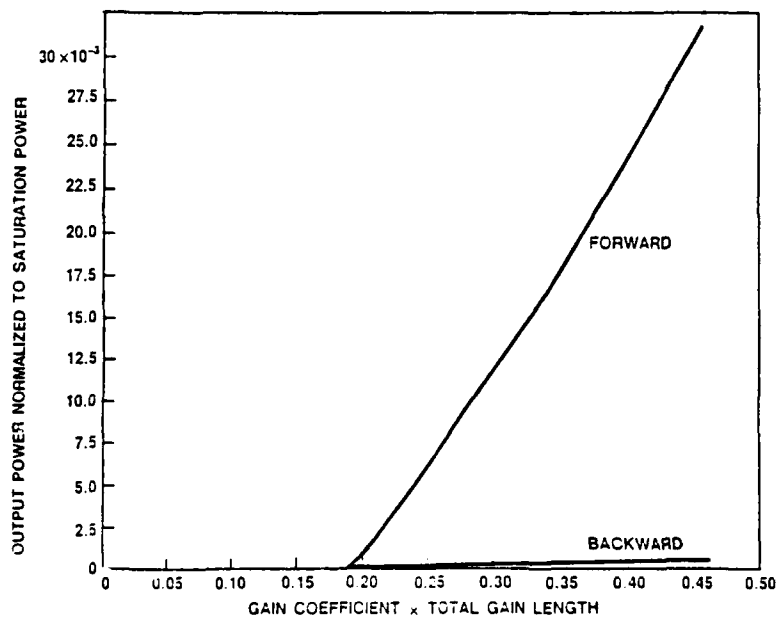


Figure 15. Power output vs pumping parameter

$$A_j = F_{ij} \left[\frac{(\beta_i + \beta_j)}{2\beta_j} A_i + \frac{(\beta_j - \beta_i)}{2\beta_j} B_i \right] \quad (2-4)$$

$$B_j = F_{ij} \left[\frac{(\beta_j - \beta_i)}{2\beta_j} A_i + \frac{(\beta_i + \beta_j)}{2\beta_j} B_i \right] \quad (2-5)$$

$$F_{ij} = \left(\frac{\beta_j}{\beta_i} \right)^{(1/2)} \frac{H_{ij}}{(H_{ii}H_{jj})^{(1/2)}} \quad (2-6)$$

$$H_{ij} = \sum \int \int dx dy w_i w_j^* \quad (2-7)$$

where w_i is the waveguide mode field function in layer i , and the sum in Eq. (2-7) is over polarization. Eqs. (2-4)-(2-7) have been derived following results by Wang². The overlap integrals in Eq. (2-6) account for the mismatch in mode profile between two layers. Eqs. (2-1)-(2-7) are used repetitively to calculate the field amplitude in all layers; the boundary conditions are satisfied only for a particular set of values of g_0 , λ , B_1 , and A_{n+2} (n is the number of layers).

We apply this model to a particular longitudinal mode (at 882.6 nm) of the SEL structure of Fig. 2. Fig. 15 shows the forward and backward output power versus pumping calculated for the design longitudinal mode (at 882.6 nm) of the structure of Fig. 2. The quarter-wave phase shift layer effectively diverts most of the power out of the wafer. It is seen from Fig. 16 that the spatial intensity is maximized at the phase shift layer, and the gain is saturated primarily in the front portion of the resonator. The gain in the back portion of the resonator is available for extraction by the next mode with shorter wavelength (at 860.8 nm), since its intensity is maximized in that section of the structure. For this laser structure the threshold gain of the mode at 860.8 nm is roughly four times that of the main mode at 882.6 nm; therefore its contribution to the output spectrum will be relatively small and likely be as a broad amplified spontaneous emission background. In fact the experimental results obtained from this structure (cf. Fig. 10) seem to agree with this prediction.

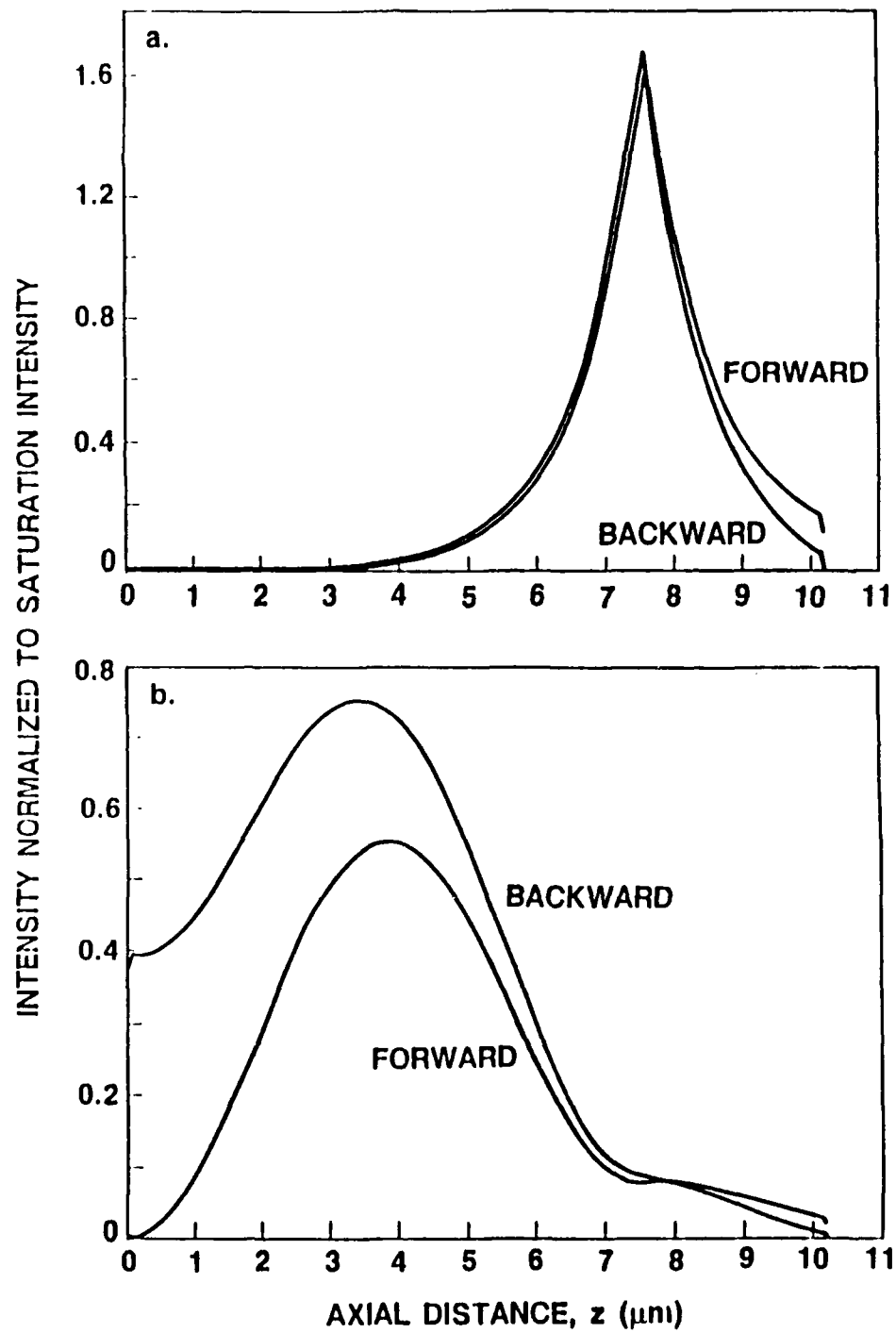


Figure 16. Spatial intensity distribution for (a) the Bragg mode, and (b) next higher order axial mode

CHAPTER 4 SUMMARY AND DISCUSSION

In summary, we have conducted an effort in the development and investigation of SEL diodes and SEL arrays, and have made major progress and accomplishments during this 18-month project. We developed a novel SEL using a transverse buried heterojunction structure and a vertical distributed feedback cavity, and successfully fabricated and demonstrated the operation of such a SEL. The SEL has unique characteristics including a very low threshold current and a short optical cavity that can be modulated at a very high rate, making it important for optical communications and signal processing.

We further extended the single SEL concept to the formation of a 2-D array, and fabricated and demonstrated a SEL array with 6×16 elements. This effort proves the concept that this SEL design configuration can be scaled into a 2-D array easily and has a potential of forming a large 2-D array with very high packing density on a wafer level. These features are very desirable for optical interconnect, optical pumping, and signal processing.

We also undertook a theoretical modeling effort in conjunction with the experimental development effort, with the objective of analyzing and understanding the device performance characteristics as well as providing a design tool and guideline. Two theoretical models were developed. One model is based on the Bloch wave approximation, and another model uses the thin film discrete wave propagation method. Both models have proven to be very useful.

During the course of this project several technical papers were generated. Four papers were presented at the technical conferences and two papers are submitted for publication in refereed journals. The reprints and preprints of these papers are attached in the appendix.

The progress and achievements we have achieved during this project period are very encouraging. However, these results are preliminary, and there remains a number of technical issues regarding the development and understanding of the SEL and its array that need to be addressed.

These issues include (1) the relatively low quantum efficiency, (2) the spatial hole burning of DFB, (3) the broad emission linewidth, (4) the emission beam quality, (5) the array coherence, (6) the power scalability, and (7) the development of DBR type SEL. All these technical issues are very important in understanding the device physics and performance characteristics of the SEL.

CHAPTER 5 RECOMMENDATION

Based on our preliminary findings obtained thus far during the course of this project, we found the SEL technology we developed has a number of desirable features and key functional advantages over the conventional edge emitting laser diodes and other types of SELs. However, because of the remaining technical issues we mentioned previously, the ultimate superiority and potential limitations of this SEL technology cannot be candidly assessed. Therefore, we strongly recommend that a follow-on research effort in this SEL technology be continued. The follow-on effort will investigate those technical issues thoroughly and bring this technology to a more mature stage for further assessment. Such an effort could also make the SEL an enabling technology for many potential DoD applications in the areas of optical signal processing, optical communication, optical interconnect, optical pumping, and optical computing.

REFERENCE:

1. G. Bjork and O. Nilsson, J. Lightwave Tech. LT-5, 140, (1987)
2. S. Wang, J. Appl. Phys. 44, 767 (1973)

APPENDIX

A list of papers either presented or to be published as a result of this project is as follows, and the reprints and preprints of these papers are attached.

I. Conference paper

1. "High modulation rate laser array for microwave optics," SPIE conference, paper 1102-03, March 1989
2. "A single mode model of surface emitting DFB and DBR semiconductor lasers," OSA meeting, paper MJ9, Oct. 1988
3. "Characteristic emission of a transverse buried heterojunction GaAs/AlGaAs surface emitting laser diode," IQEC, paper TuP-43, July 1988
4. "GaAs/AlGaAs surface emitting laser diode with vertical distributed feedback optical cavity and transverse junction buried heterostructure," IEDM paper 34.3, Dec. 1987

II. Journal paper

1. "On the emission properties of surface emitting DFB and DBR semiconductor lasers," to be published in Optics Letters.
2. "Propagation of light in periodic structures with material dispersion and application to the distributed feedback surface emitting laser diode," submitted to J.Quantum Electronics.

III. Internal report

1. "Propagation of light in periodic structures with material dispersion: general theory and application to the DFB surface emitting laser diode," Memorandum No. UCB/ERL M 88/63, Oct. 1988.

GaAs/AlGaAs SURFACE EMITTING LASER DIODE WITH VERTICAL DISTRIBUTED FEEDBACK OPTICAL CAVITY AND TRANSVERSE JUNCTION BURIED HETEROSTRUCTURE

Wei Hsin, Mutsuo Ogura^{a)}, Jean-Pierre Weber, S.C. Wang^{b)}, J.J. Yang^{c)},
M.C. Wu, Shyh Wang, and John R. Whinnery.

Department of Electrical Engineering and Computer Science, and
Electronics Research Laboratory, University of California, Berkeley, CA 94720

ABSTRACT

A threshold current of 2 mA at room temperature CW operation is realized in a vertical distributed feedback surface emitting laser diode (VDFB-SELD) with transverse junction buried heterostructure (TJBH). In this TJBH structure, the vertical distributed feedback active region (AlGaAs/GaAs multilayer) is entirely surrounded by N- and P-type AlGaAs cladding layer for minority carrier confinement. The far field angle is 7 to 8 degrees. The beam shape is nearly circular. However, the lasing spectrum is broad (1.5 to 3 nm) compared with the conventional edge-emitting laser. Theoretical model of the VDFB-SELD-TJBH by using DFB theory and its computer simulation of the spectrum shows good agreement with the experimental measurements.

INTRODUCTION

The vertical distributed feedback surface emitting laser diode (VDFB-SELD) is very advantageous for optoelectronic integration because it does not need cleavage nor a backside substrate etching process to form a vertical optical cavity [1,2]. High reflectivity of the cavity mirrors and high efficiency in the carrier confinement structure are important to realize low threshold current operation of the VDFB-SELD. High reflectivity of the cavity mirrors was already realized by the use of a quarter wavelength stack of AlGaAs and GaAs thin layers [3]; however, carrier confinement was not adequate in the previous structures [1,2]. In this report, we realized a novel transverse junction buried heterostructure (TJBH) by selective liquid phase epitaxy (LPE) and selective zinc diffusion, and achieved a room-temperature, low-threshold current, CW operation of the VDFB-SELD.

DEVICE FABRICATION

Figure 1 depicts the VDFB-SELD-TJBH structure. The active layer is made of a quarter wavelength stack of $\text{Al}_{0.3}\text{Ga}_{0.7}\text{As}$ and GaAs thin layers prepared by metal-organic chemical vapor deposition (MOCVD). The thicknesses of each pair of AlGaAs/GaAs layers are first chosen and then adjusted so that the reflectivity is peaked near the gain maximum of GaAs. The optical cavity, formed by these AlGaAs/GaAs multilayers, consists of 20

pairs at the top, 60 pairs at the bottom, and a phase shifter GaAs layer in between. The thickness of the GaAs phase shifting layer is about half wavelength of the gain maximum, which allows the laser to lase at the Bragg wavelength of the multilayer. This multilayer is etched by a wet etching solution leaving mesas with different dimensions ranging from 2×8 to $3 \times 17 \mu\text{m}$ on the top surface and $10 \mu\text{m}$ in height with the DFB type active region. The N-type $\text{Al}_{0.4}\text{Ga}_{0.6}\text{As}$ cladding layer is formed by selective LPE using silicon nitride on top of the mesa as a selective epitaxial mask. The lateral pn-junction is formed by selective zinc diffusion through an opening in the silicon nitride film at a distance of 3 to $4 \mu\text{m}$ away from the edge of the mesa. Due to lateral diffusion, the zinc diffusion front is inside the multilayer. In this structure, the GaAs/AlGaAs part of the multilayer is completely surrounded by the N- or P-type AlGaAs. Therefore, carrier confinement should be comparable with that of buried heterostructures used with the edge emitting laser diode. The zinc diffusion front spreads along the cladding region as well as along the AlGaAs/GaAs multilayer. However, carriers are injected predominantly into the GaAs part of the multilayer because the turn-on voltage for an AlGaAs pn-junction is higher than for a GaAs pn junction.

DEVICE RESULTS

Figure 2 shows the light output versus dc current (I-L) characteristics of the VDFB-SELD. The laser is operated CW at room temperature. The threshold current is 2 mA as seen in the inset of this figure. The total light output increases linearly up to 25 mA. The output power is $28 \mu\text{W}$ at 10 mA and $87 \mu\text{W}$ at 25 mA.

Figure 3(a) shows the near-field pattern of the VDFB-SELD. The light-emitting region is tightly confined within the rectangular top emission surface. Therefore, carrier confinement by the TJBH structure is very effective. Figure 3(b) shows the far-field pattern at an operating current of 20 mA. It shows a nearly circular pattern with a gaussian-like intensity profile. The estimated beam divergence angle is about 7 to 8 degrees. This indicates a good spatial coherence in this device. However, the circular emission pattern is not expected from a trapezoidal mesa cavity with a rectangular emission surface. We think that the curved boundary between the AlGaAs/GaAs multilayer active region and AlGaAs cladding region may affect the emission beam pattern.

Figure 4 shows the CW electroluminescence spectra

a) also with Electrotechnical Laboratory, Sakuramura, Niihari-gun, Ibaraki 305 Japan b) Research & Development Division, Lockheed Missiles & Space Company, Inc., Palo Alto, CA 94304 1187 c) Space and Technology Group, TRW, One Space Park, Redondo Beach, California 92078

of the VDFB-SELD-TJBH structure. As is seen in the inset of the figure, the onset of sharp emission line at 884 nm becomes obvious at the drive current of 1.6 mA. This current level is consistent with the threshold current deduced from the I-E characteristics. The half width of the lasing spectrum at 884 nm is rather wide (1.5 to 3 nm) compared with an edge emitting (EE) laser diode and there is a large amplified spontaneous emission at the shorter wavelength side. However, there are fundamental differences between the short-cavity SE and long-cavity EE lasers. First, the mode spacing in the SE laser is much wider than the EE laser. For such wide spectral separation, the mode broadening mechanism will be different from that of the EE laser. Second, the spontaneous emission factor in the short-cavity SE laser is expected to be much larger than that in the long-cavity EE laser [4]. Both these factors will affect the behavior of the two types of lasers in terms of lasing spectrum.

THEORETICAL MODELING OF DEVICE

We use Bloch wave theory for the DFB multilayer section [5] and consider the laser as an amplifier driven by spontaneous emission. Figure 5 shows the idealized structure we used for the calculation of the reflectivity curve and emission spectrum. E_1 & E_4 , E_2 & E_3 are the electric fields of the forward- and backward-going waves respectively, at the two interfaces of the phase shifter region (I_3). S_i 's are the equivalent sources at the interfaces due to the random spontaneous emission in each section. R_i 's and T_i 's are the reflection and transmission coefficients of the Bloch waves at the interfaces. R_2 , R_3 and T_2 , T_3 refer to the phase shifter as a whole. The round-trip condition is given by:

$$(1 - R_1 R_2 P_2^2)(1 - R_3 R_4 P_4^2) = R_1 R_4 T_2 T_3 P_2^2 P_4^2 \quad (1)$$

where the P_i 's are the propagation factors in each section [5]. From Eqn.(1), we can calculate the wavelengths and threshold gains of the modes. The output spectral power density is given by:

$$P_{out}(\lambda) = \left| R_1 T_1 P_2^2 \frac{N}{D} + T_1 \right|^2 P_1(\lambda) + \left| T_1 P_2 \frac{N}{D} \right|^2 P_2(\lambda) + \left| T_1 P_2 \frac{T_3}{D} \right|^2 P_3(\lambda) + \left| T_1 T_3 R_4 P_2 \frac{P_4}{D} \right|^2 P_4(\lambda) \quad (2)$$

where

$$N = R_2 + R_4 P_4^2 (T_2 T_3 - R_2 R_3)$$

$$D = (1 - R_1 R_2 P_2^2)(1 - R_3 R_4 P_4^2) - R_1 R_4 T_2 T_3 P_2^2 P_4^2$$

and the $P_i(\lambda)$'s are the spectral power densities of the equivalent spontaneous emission sources S_i 's at the four interfaces. Realistic gain and spontaneous emission spectrum were used for the calculations.

COMPUTER SIMULATION RESULTS

Figure 6 shows the reflectivity curve measured from the top surface and the theoretical calculation based on Bloch wave theory. The agreement is very good in predicting the shape of reflectivity curve. Figure 7 shows the experimental pulsed spectrum and the computer calculated power spectrum from Eqn.(1) and Eqn.(2) above, at

different carrier densities. The agreement is fairly good. The lowest effective threshold power gain mode ($G_{th} \sim 3.0 \text{ cm}^{-1}$) is at 884 nm from calculation, all the other modes which appear as the humps in the spectrum have a much higher effective threshold power gain ($G_{th} \sim 1-2 \times 10^3 \text{ cm}^{-1}$). Thus, only the mode at 884 nm is lasing (i.e. above threshold), all the other modes are still below threshold at these current levels. Therefore, the emission spectrum shows a sharp peak at 884 nm and much broader humps at shorter wavelengths due to the amplified spontaneous emission produced by these high threshold gain modes. In this model, we assume that the carrier density is given and the gain spectrum is then calculated with a semi-empirical model, assuming Fermi-Dirac distributions in the bands. Gain saturation is not taken into account. Therefore, the model is really valid only below threshold and fails to give the exact amplitude of the lasing peak above threshold. The fact that it reproduces the shape of the spectrum above threshold elsewhere indicates that there is inhomogeneous broadening and that the carrier density is not clamped at threshold. The measured FWHM of the lasing peak is probably larger than the real one because of the limited resolution (7 Å) of the measurement (which was incorporated in the simulations).

CONCLUSIONS

In conclusion, the VDFB-SELD-TJBH structure is realized with the combination of MOCVD, selective LPE, and zinc diffusion techniques. In this structure, an MOCVD-grown AlGaAs/GaAs multilayer is surrounded completely by P- and N-type AlGaAs cladding layers, such that lateral carrier injection and carrier confinement are achieved. Nominal threshold current for CW operation is 2 mA. The radiation region is well confined within the active region. The far-field pattern is circular and well defined. However, lasing spectra at 884 nm is broad (1.5 to 3 nm) and there is large amplified spontaneous emission at shorter wavelengths. Computer simulation shows good agreement with the measurement. Further improvement of the spectrum can be realized by proper modifications of the optical cavity and layer thickness of the multilayer and phase shifter.

ACKNOWLEDGEMENTS

The authors acknowledge contributions of Dr. Shih-Yuan Wang and Yu-Min Hwang of Hewlett Packard Laboratory, Palo Alto; and Dr. Michael Rubin of Lawrence Berkeley Laboratory. They also acknowledge Professor A.E. Siegman of Stanford University; Professor A. Dienes of the University of California, Davis; Professor J.S. Smith, and Ghulam Hasnain of the University of California, Berkeley; and T.R. Ranganath of Hewlett Packard Laboratory, Palo Alto, for their helpful discussions. They also appreciate the technical assistance of Lillian Z. Gacusan, and Larry Dries of the Lockheed Missiles & Space Company, Inc., Palo Alto. This work is supported in part by NSF No. ECE-8410838, JSEP No. F49620-84 C-0057, Lockheed Missiles & Space Company, and the Office of Naval Research.

REFERENCES

- [1]. M. Ogura, S. Mukai and S. Wang, Proc. of the device research conference, May 1986
- [2]. M. Ogura, T. Hata, and T. Yao, Jpn. J. Appl. Phys.

- [3]. M. Ogura, I. Hata, N.J. Kawai, and T.Yao, Jpn. J. Appl. Phys. 22, (1983) L112
- [4]. T.P. Lee, C.A. Burrus, J.A. Copeland, A.G. Dentai, and D. Marcuse, IEEE J. Quantum Electron. QE-18, 1101 (1982)
- [5]. Shyh Wang, *Semiconductors and Semimetals*, Vol. 22 Part E, Chap 1., Academic Press, Inc., 1985.

FIGURE CAPTIONS

- Fig.(1) (a) Schematic diagram of the VDFB-SELD-TJBH structure. (b) Cross-sectional SEM picture of the VDFB-SELD-TJBH structure. The white contrasted region at the right side of the multilayer is a zinc diffused P-type AlGaAs cladding layer.
- Fig.(2) Light output versus dc drive current of the VDFB-SELD-TJBH structure.
- Fig.(3) (a) Near-field pattern of the VDFB-SELD. Also shows the line profile of the field intensity across the long edge of the rectangular emission region. (b) Far-field pattern and its intensity line profile across the beam center of the VDFB-SELD.
- Fig.(4) CW electroluminescence spectra of the VDFB-SELD.
- Fig.(5) Schematic diagram of the idealized VDFB-SELD structure used for theoretical model. L_3 is the phase shifter region, L_2 & L_4 & L_5 are the multilayer DFB section.
- Fig.(6) Measured and calculated reflectivity curve of the multilayer from the top surface.
- Fig.(7) Spectrum of the VDFB-SELD. (a) Experimental measurements (400 ns pulse). Resolution of the monochromator is 0.7 nm in the measurement. (b) Computer simulation results for carrier density $N=0.5 \times 10^{18} \text{ cm}^{-3}$ (1), $1 \times 10^{18} \text{ cm}^{-3}$ (2), $2 \times 10^{18} \text{ cm}^{-3}$ (3), $3 \times 10^{18} \text{ cm}^{-3}$ (4).

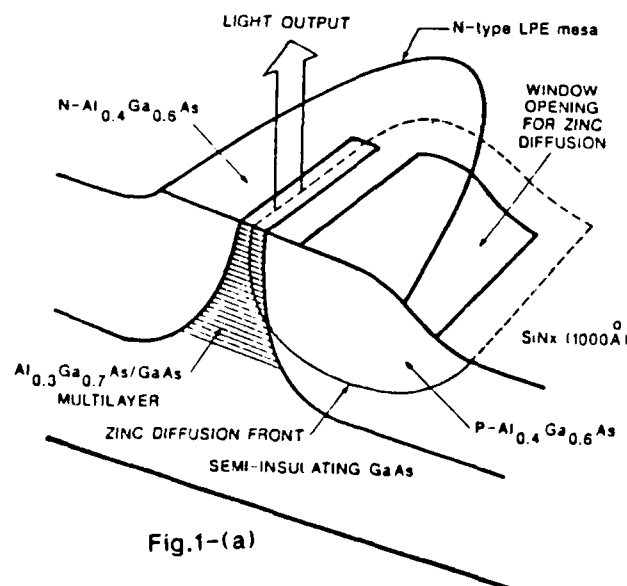


Fig.1-(a)

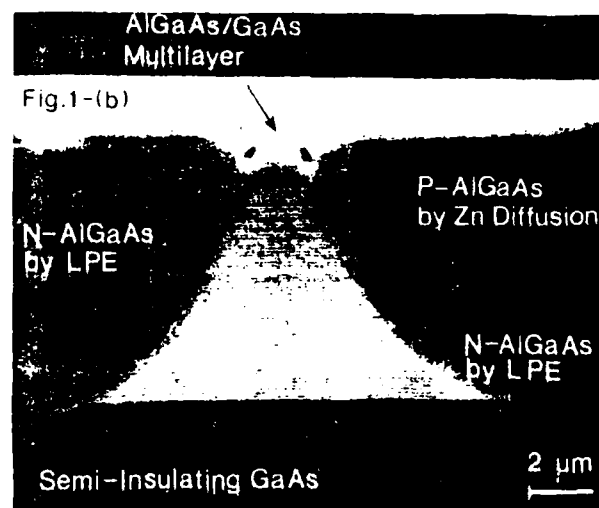


Fig.1-(b)

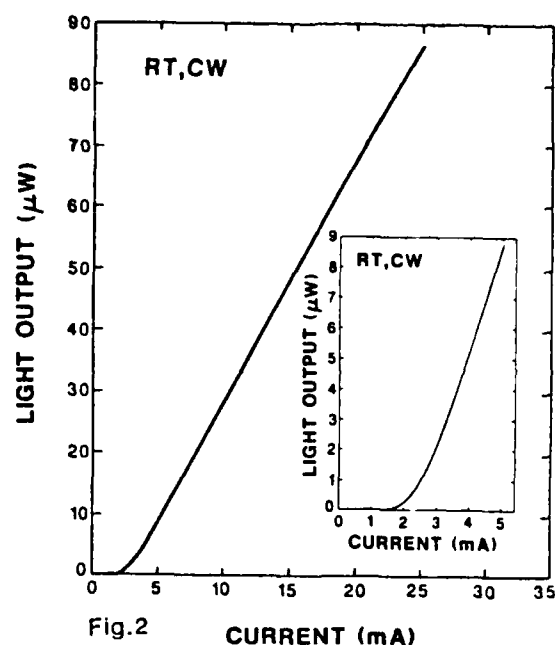


Fig.2

NEAR FIELD

Fig.3-(a)



FAR FIELD Fig.3-(b)

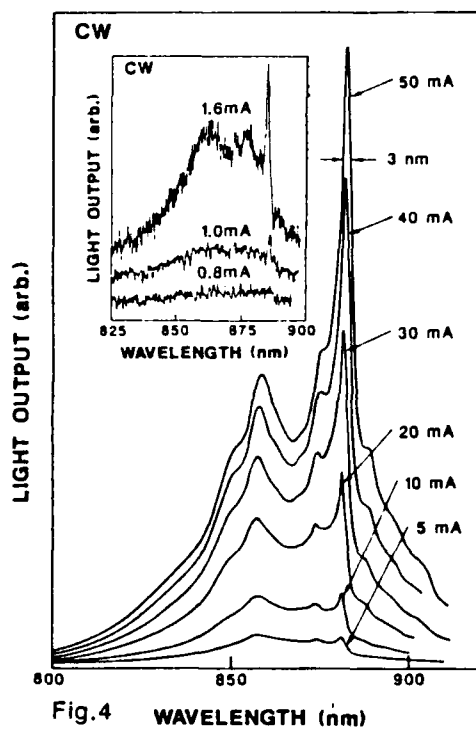
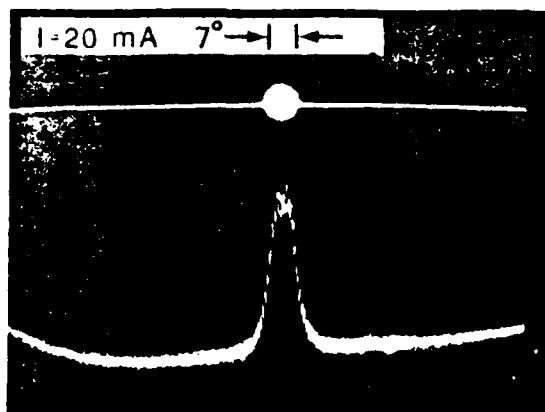


Fig.4 WAVELENGTH (nm)

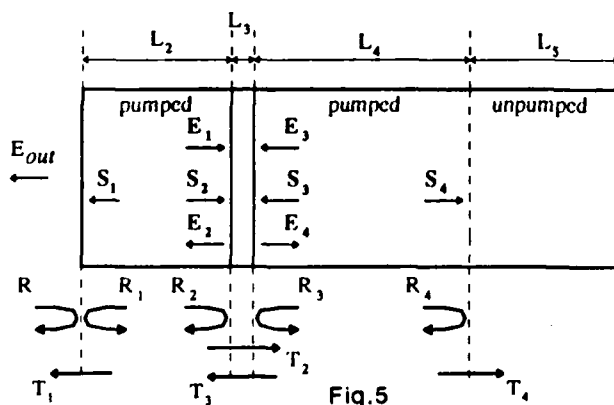


Fig.5

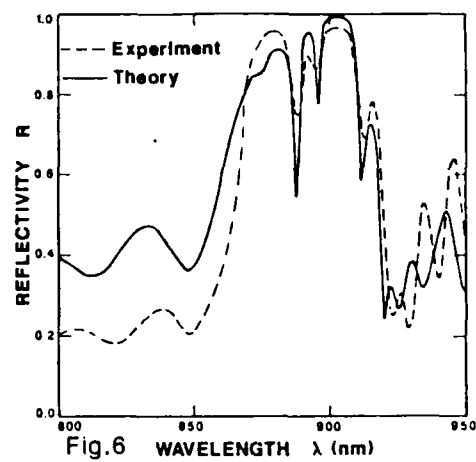


Fig.6 WAVELENGTH λ (nm)

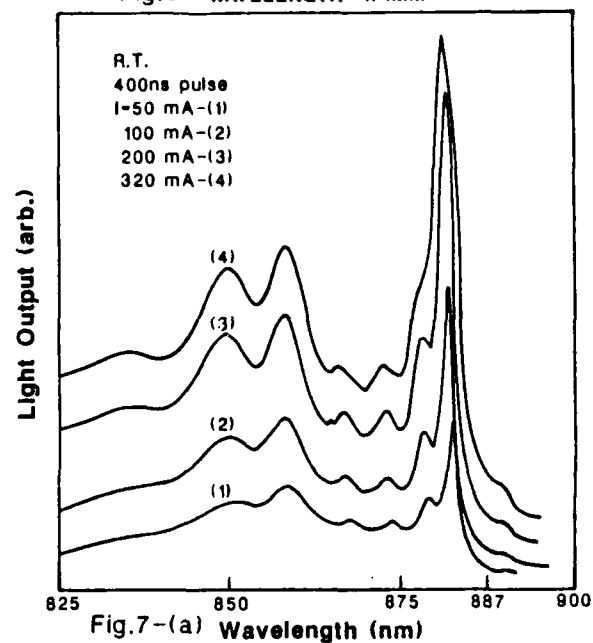


Fig.7-(a) Wavelength (nm)

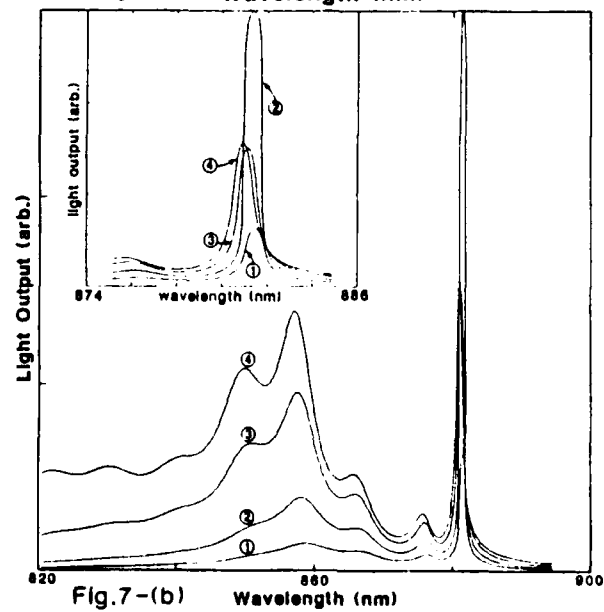


Fig.7-(b) Wavelength (nm)

1988

ANNUAL MEETING
OPTICAL SOCIETY OF AMERICA
TECHNICAL DIGEST

Summaries of papers
presented at the Annual Meeting of the Optical Society of America

30 October–4 November 1988
Santa Clara, California

Conference Edition

Optical Society of America
1816 Jefferson Place, NW
Washington, DC 20036
(202) 223-8130

titation rate can only be achieved in highly doped (50%) crystals where by $^4I_{13/2} \rightarrow ^4I_{15/2}$, $^4I_{13/2} \rightarrow ^4I_{9/2}$ cross relaxation the long-living lower laser level can be depopulated. Highly doped flashlamp-pumped $\text{YAlO}_3:\text{Er}$ has a typical laser threshold of ≈ 30 J for a crystal of 75-mm length and 6.35-mm diameter. 100-Hz operation would thus lead to an average pump power exceeding 3 kW, well beyond the thermal damage threshold. Therefore, a reduction of the threshold is required.

As most of the pump light of a xenon flashlamp is absorbed far above the upper laser level, this excitation leads to cross relaxations, emission of resonance lines, and stimulated multiphonon transitions. These processes can enhance the laser threshold or cause crystal heating. To reduce the threshold, the pump light was spectrally filtered by introducing color filters or dyes in the pump cavity between the flashlamp and the laser rod. Experimentally a reduction of the absorbed energy in the crystal at laser threshold by a factor of ~ 4 and a pulse repetition rate up to 125 Hz could be achieved. (12 min)

MJ3 Optimization of the gain in Nd:Silica single-mode fibers

M. DIGONNET, K. LIU, H. J. SHAW, Stanford U., Ginzton Laboratory, Stanford, CA 94305-4085.

The development of efficient (low pump power) optical amplifiers and sources based on rare-earth doped or other active fibers depends critically on the optical gain of the fiber, especially when three-level or low gain (e.g., nonlinear) processes are involved. In optically end-pumped fibers, the gain depends on optical energy confinement provided by the fiber and consequently on the fiber N.A. and core dimension. These dependences were investigated experimentally and theoretically to establish the range of fiber parameters which optimizes the gain. In $\text{Nd}:\text{SiO}_2$ fibers from different manufacturers, we have measured an optical gain ranging from 0.15 to 0.4 dB/mW. These data were analyzed with a model of gain in fibers accounting for energy confinement through pump and signal mode spatial overlap. It shows that the observed gain differences are largely due to differences in the fiber index profiles as opposed to differences in doping levels. This suggests that the fiber gain can be optimized by selecting the core size and N.A. in a well-defined range, predicted theoretically and supported by gain measurements. As much as a 2-4 gain increase (and equivalent reduction in the required pump power) over what we have observed may be expected from careful fiber design. (12 min)

MJ4 Effect of ion-ion interactions on the lifetimes of the 2900-nm laser levels of Er^{3+}

W. Q. SHI, J. MACHAN, M. BIRNBAUM, U. Southern California, Center for Laser Studies, Los Angeles, CA 90089-1112; M. BASS, U. Central Florida, Orlando FL 32716-0001; M. KOKTA, Union Carbide Corp., Washougal, WA 98671.

The effects of ion-ion interactions in heavily doped $\text{Er}:\text{YAG}$, $\text{Er}:\text{Nd}:\text{YAG}$, and $\text{Er}:\text{Nd}:\text{YALO}$ on the lifetimes of the $^4I_{11/2}$ and $^4I_{13/2}$ levels of Er^{3+} were studied. In $\text{Er}:\text{YAG}$, the $^4I_{13/2}$ lifetime first increases with increasing concentration and then decreases. The increase can be attributed to radiation trapping and the decrease to concentration quenching. In $\text{Nd}(1\%), \text{Er}(15\%):\text{YAG}$, the $^4I_{11/2}$ level lifetime is halved, while the $^4I_{13/2}$ level lifetime suffers an approximately sixty-fold reduction, but $\tau_{11/2} > \tau_{13/2}$. However, study of a YALO crystal (1% Nd, 15% Er) disclosed a $\tau_{11/2}/\tau_{13/2}$ ratio of ≈ 1.7 , indicating the feasibility of four-level laser operation. Ion-ion interaction coefficients were obtained from an analysis using the rate

equation model. Laser operation at 2900 nm with $\text{Nd}:\text{Er}:\text{YAG}$ and $\text{Nd}:\text{Er}:\text{YALO}$ is presented.

(12 min)

MJ5 Semiconductor laser theory with many-body effects

STEPHAN W. KOCH, HARTMUT HAUG, MURRAY SARGENT III, U. Arizona, Optical Sciences Center, Tucson, AZ 85721.

A theory of a semiconductor laser is developed that includes the many-body effects due to Coulomb interactions. The theory is valid for both 3-D bulk semiconductors as well as quasi-2-D quantum well structures. We emphasize plasma density-dependent band gap renormalization, broadening due to intraband scattering, and electron-hole Coulomb enhancement. The very short intraband scattering relaxation time allows us to eliminate the interband polarization adiabatically and to introduce a hydrodynamic description of the intraband kinetics. From this general formulation a diffusion equation for the carrier density is derived. The resulting diffusion coefficient decreases with carrier density and laser intensity due to the reduction of the electron drift. We use our theory in the problem of laser gain, index, and side mode instabilities. We show that near the laser operating point, our many-body theory can be approximated by a simple rate equation formalism. However, in contrast to the usual rate-equation theory, the semiconductor rate constants are functions of temperature, tuning, and carrier density. (12 min)

MJ6 Noise characteristics of nearly single-mode semiconductor lasers

G. GRAY, RAJARSHI ROY, Georgia Institute of Technology, School of Physics, Atlanta, GA 30332.

We have developed a computer model which simulates the nonlinear Langevin equations for a semiconductor laser with one strong mode and one small side mode. With this model we are able to probe the laser dynamics over a wide range of operating powers, from below threshold, when the laser is essentially a thermal noise generator, to way above threshold. The model correctly reproduces the well-known intensity noise spectra and mode partition effects. We further calculate noise variances and intensity autocorrelation and cross-correlation functions for both modes as well as for the total power, and we compare these results to linearized theories. Finally, we calculate the laser field spectrum and investigate the effect of the side mode on the laser linewidth. All the above properties are calculated for many different values of the mode suppression ratio. (12 min)

MJ7 Kinetics of gradual degradation in semiconductor lasers

YU. L. KHAITAL, Technion-Israel Institute of Technology, Haifa 32000, Israel; JOSEPH SALZMAN, Technion-Israel Institute of Technology, Solid State Institute, Haifa 32000, Israel; R. BESERMAN, Technion-Israel Institute of Technology, Department of Electrical Engineering, Haifa, 32000, Israel.

Gradual degradation in semiconductor lasers is caused by the creation and migration of point defects which require jumping of atoms from their initial position to disordered ones (with activation energy E_a of a few electron volts). The injection of a nonequilibrium electron-hole plasma may increase the probability of structural changes and reduce their activation energy by $\delta E \sim E_a - F$, through nonradiative recombination (E_a and F are the quasi-Fermi levels). Such enhancement is possible only if the recombination is synchronized with the atom jump event, and the released energy

δE is localized around this atom. In the present model, such synchronization is inherent: the fluctuating atom forms a transient point defect which behaves as a nonradiative recombination center of lifetime $\Delta\tau \sim 10^{-11} - 10^{-10}$ s. Free carriers are trapped at these centers leading to synchronous release of localized energy δE . This model is based on the kinetic many-body theory of short-lived large energy fluctuations of atoms. The laser degradation rate K is given by $K = K_0 \exp[-(E_a - \delta E)/kT]$ with K_0 and δE expressed in terms of the laser parameters (carrier concentration, energy gap, defect concentration, etc.). Calculated laser lifetimes are in good agreement with experimental data. (12 min)

1. J. D. Weeks, J. C. Tully, and L. C. Kimerling, Phys. Rev. B **12**, 3286 (1975).

2. Yu. L. Khaits, Phys. Rep. **99**, 237 (1983).

3. Yu. L. Khaits and R. Beserman, Phys. Rev. B **33**, 2983 (1986).

MJ8 Degradation of mode discrimination in distributed feedback lasers due to spatial hole burning

WILLIAM S. RABINOVICH, B. J. FELDMAN, U.S. Naval Research Laboratory, Laser Physics Branch, Washington, DC 20375.

Distributed feedback (DFB) lasers have become of increasing interest in fields which require single longitudinal mode (SLM) sources. This SLM behavior occurs because the threshold gain for a longitudinal mode in a DFB laser increases as that mode's frequency moves away from the Bragg frequency. We have derived coupled-mode equations for the above threshold behavior of homogeneously broadened DFB lasers, including the spatial hole burning grating induced by the laser modes. These equations were numerically integrated for boundary conditions appropriate to a variety of DFB structures. To study the mode discrimination of the DFB laser, we allow one longitudinal mode to exceed threshold and induce a spatial hole burning grating. We simultaneously solve for the threshold of a second longitudinal mode in the presence of both this field-induced grating and the externally induced grating. The ratio of the threshold of this second longitudinal mode to the average saturated line center gain available in the laser is defined as the mode discrimination. The higher the discrimination the more likely the laser is to be SLM. Our analysis shows that the mode discrimination of DFB lasers with nonsaturable index coupling, such as semiconductor DFB lasers, is seriously degraded as the laser exceeds output powers a few times above threshold. The same does not hold true for gain coupled DFB lasers, indicating that these types of laser may be more suitable for high output power SLM applications. (12 min)

MJ9 Single-mode model of surface-emitting DFB and DBR semiconductor lasers

THADDEUS G. DZIURA, S. C. WANG, Lockheed Palo Alto Research Laboratory, Palo Alto, CA 94304.

The surface-emitting semiconductor laser^{1,2,3} is expected to be a key component in future optoelectronic and optical signal processing applications. Several designs are under development including electrically excited and photopumped lasers. The requirement of a surface-emitting geometry imposes important constraints on laser design, which must be considered to achieve an efficient emitter. For example, the method of extracting the laser beam must accommodate that part of the structure providing electrical excitation. Also, a model that calculates laser properties only

at threshold is clearly not adequate. We have developed a transfer equation model of short cavity DFB and DBR surface-emitting lasers in which the resonator is defined by multilayer quarter-wavelength semiconductor structures providing distributed feedback. These lasers naturally lend themselves to a description in which the forward and backward waves are propagated from layer to layer by a set of equations detailing the gain and loss due to the material and the feedback and radiation loss due to the Bragg grating. We apply this method to calculate power output, longitudinal modes, and axial intensity profiles for several laser types. In particular, we show that the forward to backward power ratio can depend on mode number as well as pumping level. (12 min)

1. M. Ogura, W. Hsin, M. C. Wu, S. Wang, J. R. Whinnery, and S. C. Wang, *Appl Phys Lett* **51**, 1666 (1987).
2. F. Koyama, K. Tomomatsu, and K. Iga, in *Technical Digest, Conference on Lasers and Electro-Optics* (Optical Society of America, Washington, DC, 1988), paper WO5.
3. Z. L. Liu, J. N. Walpole, and V. Diadiuk, in *Technical Digest, Topical Meeting on Integrated and Guided Wave Optics* (Optical Society of America, Washington, DC, 1988), paper WA1.

Monday

MORNING

31 October 1988

MK

BALLROOM D

10:00 AM Optical Communication

Paul Prucnal, Princeton University, Presider

MK1 Detection of phase-modulated optical signals through two-wave mixing in photorefractive materials

L. BOUTSIKARIS, FRED DAVIDSON, Johns Hopkins U., Electrical Engineering Department, Baltimore, MD 21218

Two-wave mixing in photorefractive crystals has been shown to combine coherently a modulated optical signal beam with a strong pump optical field.¹ For a phase-modulated signal beam, the induced index of refraction phase grating inside the crystal yields a coupling of the optical fields of the pump and signal so that subsequent intensity detection results in apparent intensity modulation of the transmitted signal or pump beams. This provides an easy way to detect phase differences between two optical beams. Some of the advantages the above scheme offers over commonly used coherent optical phase detection schemes are: no loss of 3 dB in the signal beam intensity at the 50/50 beam splitter (used to combine signal and local oscillator fields); automatic alignment of the index of refraction grating with the two incident optical wavefronts; insensitivity to slow random changes in the phases of both beams. Experimental results are given, and a new definition for the resulting mixing gain for the phase-modulated beam is introduced, through which optimal conditions for input beam intensity ratios can be found. Applications to coherent homodyne detection are discussed. (12 min)

1. F. Davidson, L. Boutsikaris, and M. Kralnak, "Coherent Optical Detection Through Two-Wave Mixing in Photorefractive Materials," *Opt. Lett.* **13**, 506 (1988).

MK2 Broadband communication system using a standing wave acoustooptic modulator

R. S. TIAN, CHARLES S. IH, U. Delaware, Electrical Engineering Department, Newark, DE 19716.

There is great need for an all-service communication system by which broadband analog and high speed digital information can be transmitted simultaneously and freely. Such a system can best be implemented with frequency-division-multiplexing (FDM). The effective bandwidth of such a system is in the multigigahertz range. Because of the enormous bandwidth, the optical fiber communication (OFC) system is a good candidate for such applications. However, because of the serious intermodulation problems, it is still difficult to provide such services using OFC. A novel method, now known as double-beam-modulation (DBM) was suggested and demonstrated using a standing-wave acoustooptic modulator (SWAOM) to 216 MHz. The DBM can be implemented in many forms.¹ We describe the experiments of DBM using SWAOM for frequencies beyond 1 GHz. Theoretical analyses and comparisons of DBM with conventional FDM systems are described. (12 min)

1. C. S. Ih, R. G. Hunsperger, J. J. Kramer, R. Tian, X. Wang, K. Kissa, and J. Butler, "A Novel Modulation System for Optical Communications," *Proc. Soc. Photo-Opt. Instrum. Eng.* **876** (1988).

MK3 Novel integrated-optics modulator for optical communications

KARL KISSA, X. L. WANG, CHARLES S. IH, R. G. HUNSPERGER, U. Delaware, Electrical Engineering Department, Newark, DE 19716.

An integrated-optics standing-wave surface-acoustic-wave modulator (SWSAWM) for optical communications is being investigated. This novel modulation method, which has been described previously,¹ was used to upconvert a color TV video signal to TV channel 4 by generating a 70-MHz subcarrier with a Ti:LiNbO₃ modulator. Prisms were used to couple light in and out of the waveguide. A photodetector placed at one of the diffracted beams received the upconverted signal. An ordinary TV receiver recovered the original video signal. Picture quality was good. The phase of the acoustooptically generated subcarrier could be changed by changing the phase relationship between the rf signals driving the two interdigital transducers. The standing wave nature of the modulator was also demonstrated by the frequency dependence of the diffracted optical power. Nonlinearities in surface acoustic wave generation and/or acoustooptic diffraction caused subcarrier distortion on high diffraction efficiencies. This effect is being examined theoretically and experimentally to determine its influence on system performance. Subcarrier generation at higher frequencies (600 MHz and above) is also being explored. (12 min)

1. C. S. Ih, R. G. Hunsperger, J. J. Kramer, R. Tian, X. Wang, K. Kissa, and J. Butler, "A Novel Modulation System for Optical Communications," *Proc. Soc. Photo-Opt. Instrum. Eng.* **876** (1988).

MK4 Use of edge light emitting diodes in signal coherence multiplexing

THEODORE L. HOUK, R. AARON FALK, RAYMOND W. HUGGINS, Boeing Co., P.O. Box 3999, Seattle, WA 98124-2499.

An edge light emitting diode (ELED) emission

spectrum is near Gaussian at 820-nm center wavelength with 33-nm FWHM, promising a short coherence length within the range of feasible titanium indiffused lithium niobate (Ti:LiNbO₃) integrated optics unequal arm Mach-Zehnder interferometer (IOMZ) optical path differences. Interferometric ELED coherence measurements were made in a tilted mirror Michelson interferometer. Fringes were viewed with a near-IR video camera and digital imaging frame store connected to a computer. This apparatus measured all the quantities needed to compute the coherence function (Born and Wolf), which fits a Gaussian function of 6.4- μ m standard deviation (SD) and peak value 0.78. We observed interference fringes in the output light of the second of two Michelson interferometers in series whenever any two of the four possible optical path lengths were equal within 3 SDs, 20 μ m. These fringes are the reconstructed signal for coherence multiplexing. Proton exchange applied to one side of a symmetric Ti:LiNbO₃ IOMZ can form a 2000- μ m optical path difference via changes in the substrate refractive index. From such MZs, we propose to form coherence multiplexing systems of up to ten parallel channels. ELED power attenuated by system Y-junctions, background, and detector noise imposes this channel limit. (12 min)

MK5 All-optical demultiplexing by frequency upconversion

HONG LIN, JOHN STEPHEN SMITH, UC-Berkeley, Electrical Engineering & Computer Sciences, Berkeley, CA 94720.

We propose the use of frequency upconversion for time division demultiplexing. Suppose we receive an N -channel signal at frequency f_1 and make a local short-pulse laser at frequency f_2 have the same repetition rate as one of the channels. Mixing them properly in a nonlinear crystal, we can upconvert only one channel to frequency $f_3 = f_1 + f_2$. We can demultiplex N channels by N such units. The frequency upconversion is a very fast (femtosecond domain or 10E5 GHz) and a low noise process. We show that nearly 80% conversion efficiency of 1.3-0.58 μ m can be expected for 50-W peak power pumping at 1.06 μ m in a 3-mm long barium sodium niobate crystal.¹ The use of waveguide structure or high nonlinear organic materials may relax the pumping power requirement substantially.

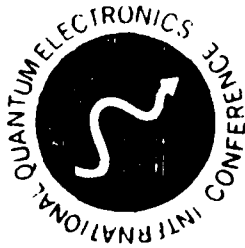
We discuss several techniques for increasing efficiencies of the system and the possibility of using semiconductor lasers as pumps. The problems of on-off ratio and crosstalk should not exist with a properly shaped pulse. In summary, we show that the all-optical demultiplier by frequency upconversion is a very interesting device for a high bit rate time-division-multiplexing optical communication system.² An experiment is under way in our laboratory. (12 min)

1. F. Zernike and J. E. Midwinter, *Applied Nonlinear Optics* (Wiley, New York, 1973).
2. R. S. Tucker et al., in *Photonic Switching*, T. K. Gustafson and P. W. Smith, Eds. (Springer-Verlag, Berlin, 1988), p. 206.

MK6 Free space optical pulse position modulation communication with laser diode transmitter and avalanche photodiode receiver

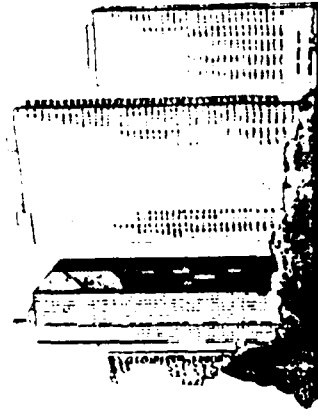
X. SUN, FREDERIC DAVIDSON, Johns Hopkins U., Electrical Engineering Department, Baltimore, MD 21218.

A direct detection optical communication system for use in an intersatellite link was constructed with an AlGaAs laser diode (Hitachi-HL8314E, $\lambda =$



JSAP Catalog Number : AP881215

Technical Digest



XVI International
Conference on
Quantum
Electronics

JULY 18-21, 1988

Keio Plaza Hotel

TOKYO, JAPAN

IQEC'88

CHARACTERISTIC EMISSION OF TRANSVERSE BURIED HETEROJUNCTION GaAs/AlGaAs SURFACE EMITTING LASER DIODE

S. C. Wang

Lockheed Palo Alto Research Laboratory

3251 Hanover Street, Palo Alto, California 94304, U.S.A.

Wei Hsin

Jean-Pierre Weber

Shyh Wang

Department of Electrical Engineering and Computer Science
University of California, Berkeley, California 94720, U.S.A.

SUMMARY

Recently we have reported (1) the achievement of laser action in a novel surface emitting laser (SEL) diode using transverse junction and buried heterostructure. Because of the effect confinement of the injected carriers and optical field of this novel SEL structure, a cw low threshold current operation in the range of a few mA was observed. This SEL has a short distributed feedback-type optical resonator and its emission spectrum showed a distinct characteristic with a seemingly wide mode spacing. In this report we present the results of an experimental investigation on the characteristic emission properties of this SEL, and compare the results with a theoretical model based on the actual device structure. A fairly good agreement between the experimental results and theoretical predictions was obtained.

The schematic of the SEL device structure is shown in Figure 1. The active region of the laser is made of alternative layers of $\text{Al}_{0.3}\text{Ga}_{0.7}\text{As}$ and GaAs with a quarter-wavelength thickness grown by the metal-organic chemical vapor deposition (MOCVD) process. The layers were grown on top of the semi-insulated GaAs substrate. A phase shifter GaAs layer, which has a thickness about a half wavelength of the gain maximum of the GaAs, is added in the middle section to form a distributed feedback laser cavity allowing the laser to lase at the Bragg wavelength. The laser cavity, formed by these AlGaAs/GaAs layers, typically consists of 20 pairs at the top and 60 pairs at the bottom.

A transverse buried heterostructure is formed by a LPE regrowth of N-type $\text{Al}_{0.4}\text{Ga}_{0.6}\text{As}$ cladding layer surrounding the active mesa region in the middle section, which is formed by selective wet etching process. The active area has a rectangular shape with a typical dimension of about 3 um by 12 um. Then a selective time diffusion process is used to form a P region on one side of the

active area, thus creating a transverse buried heterojunction with effective carrier and optical confinements. The injected carriers transversely flow into the multilayer active region, and are predominantly injected into the GaAs layers because of the lower turn-on voltage of the GaAs junction than that of the AlGaAs junction.

The laser action is obtained under cw operation at room temperature with a low threshold current ranging from 2 mA to 8 mA. The highest laser output power observed is about 0.5 mW with a quantum efficiency of about one percent. The laser emission from the surface is very uniform across the rectangular surface emitting area indicating a very effective carrier confinement by the transverse buried heterostructure. The laser beam has a very narrow divergence of about 7 to 8 degree in both directions. This indicates a good spatial coherence in this device.

The laser emission spectrum is shown in Figure 2. The onset of a sharp emission line at 884 nm becomes obvious at the drive current of about 2 mA near the threshold current. However at a higher operation current, two emission peaks occur, one main sharp peak remains at 884 nm and a secondary broad peak around 850 nm. To investigate this characteristic emission spectrum, we have developed a theoretical model using the Bloch wave theory for the distributed feedback multilayer section and consider the laser as an amplifier driven by spontaneous emission. The laser spectrum is then computed theoretically.

Figure 3 shows the computer calculated power spectrum for different carrier concentrations. As is seen in the result, a sharp emission peak at 884 nm and several emission humps are predicted. Based on the theoretical calculation, the lowest effective threshold power gain is about 4 cm^{-1} mode is at 884 nm, while all other modes which appear as the humps in the spectrum have a much higher effective threshold power gain about $1 \times 10^3 \text{ cm}^{-1}$. Thus only the mode at 884 nm is the dominant laser line which agreed fairly well with the experimental cw laser spectrum of Figure 2 and the observed pulsed laser spectra. A slight discrepancy in the mode intensity suppression ratio between the theoretical and experimental results can be attributed to the nonuniform pumping and inhomogeneous broadening of the laser.

This work is supported in part by the Office of Naval Research and Lockheed Missiles & Space Company.

I. M. Ogura et al., Appl. Phys. Lett. 51, 1055, (1987)

FIGURE CAPTIONS

Figure 1 Schematic diagram of the transverse buried heterojunction surface emitting laser diode

Figure 2 CW laser emission spectra at room temperature

Figure 3 Laser emission spectra based on theoretical calculation

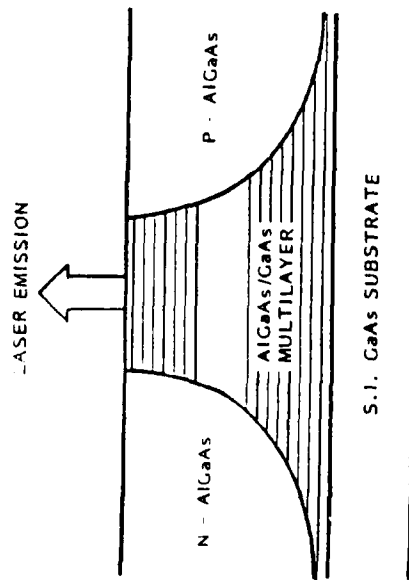


Figure 1 Schematic diagram of the transverse buried heterojunction surface emitting laser diode

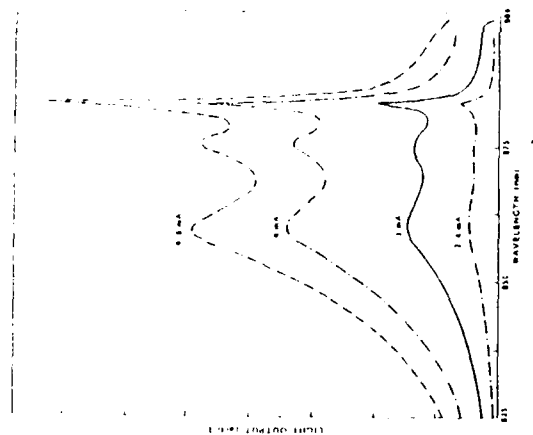


Figure 2 CW laser emission spectra at room temperature

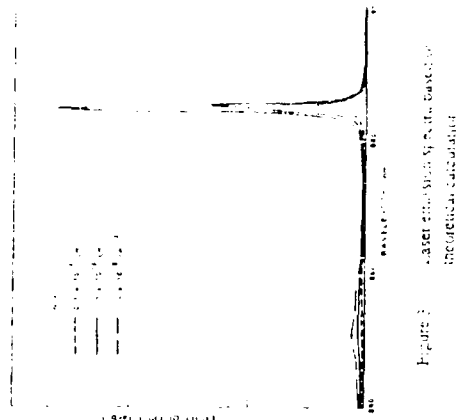


Figure 3 Laser emission spectra based on theoretical calculation

**PROPAGATION OF LIGHT IN PERIODIC
STRUCTURES WITH MATERIAL DISPERSION:
GENERAL THEORY AND APPLICATION TO
THE DFB SURFACE-EMITTING LASER DIODE**

by

Jean-Pierre Weber, Mutsuo Ogura, Wei Hsin,
S. C. Wang, and Shyh Wang

Memorandum No. UCB/ERL M88/63

14 October 1988

ELECTRONICS RESEARCH LABORATORY

College of Engineering
University of California, Berkeley
94720

**Propagation of light in periodic structures with material dispersion:
General theory and application to the DFB surface-emitting laser
diode**

Jean-Pierre Weber

*Mutsuo Ogura **

Wei Hsin

*S.C. Wang ***

Shyh Wang

Department of Electrical Engineering and Computer Science
and Electronics Research Laboratory
University of California, Berkeley, CA 94720

ABSTRACT

We extend the Bloch wave calculation method to the case of a periodic structure where the gain (loss) and the index of refraction depend on frequency. We establish a procedure to find the propagation constants and the reflection and transmission coefficients for the Bloch waves in the general case, which has not been treated previously. We then use the results of this analysis to construct a model for a surface-emitting laser diode (SELD)[2,3], which has a vertical distributed feedback structure. This model considers the laser as an amplifier driven by spontaneous emission to compute the emission spectrum. At the present time it is valid only below threshold. We present experimental results and compare the measured emission spectrum with the theoretical one. The reasons for the discrepancies and possible improvements to the device and to the theory are then discussed.

October 14, 1988

* Electrotechnical Laboratory (ETL), 1-1-4 Umezono, Sakura-mura Niihari-gun, Ibaraki 305, Japan.

** Lockheed Missiles & Space Company, Palo Alto Research Lab, 3251 Hanover Street, Palo Alto, CA 94304.

**Propagation of light in periodic structures with material dispersion:
General theory and application to the DFB surface-emitting laser
diode**

Jean-Pierre Weber

*Mutsuo Ogura **

Wei Hsin

*S.C. Wang ***

Snyh Wang

Department of Electrical Engineering and Computer Science
and Electronics Research Laboratory
University of California, Berkeley, CA 94720

I. Introduction

Propagation of waves in periodic structures has been studied extensively in the past and a great number of methods has been used to solve the problem. (For a good summary and references on the subject, see the review paper by Elachi [1].) There are two main types of such structures that are of practical interest for semiconductor laser diodes (Fig.1): (a) periodic waveguides and (b) multilayers. The second case is encountered in surface-emitting laser-diodes (SELD)[2,3]. These are basically distributed feedback (DFB) semiconductor lasers, with a vertical cavity and lateral p-n junction. The first order grating is formed by alternating layers of GaAs and GaAlAs. This structure is very advantageous for optoelectronic integration, since it does not need cleavage nor backside etching to form a vertical cavity, as some other SELD's require [4].

In most of the previous studies, the material characteristics of the periodic structures were supposed to be constant across the band of frequency of interest. This is a good approximation in usual edge-emitting distributed feedback (DFB) or distributed Bragg

* Electrotechnical Laboratory (ETL), 1-1-4 Umezono, Sakura-mura Niihari-gun, Ibaraki 305, Japan.

** Lockheed Missiles & Space Company, Palo Alto Research Lab, 3251 Hanover Street, Palo Alto, CA 94304.

reflector (DBR) laser-diodes, where we are looking at bands that are 2 to 3 nm wide. However, for SELD's, because of the strong coupling coefficients required, the stop-band has a width of 35 nm or more (in the wavelength region of 850 to 900 nm). When we have such a large bandwidth, material dispersion cannot be neglected anymore. The index of refraction can change appreciably, but the main effect is gain and loss variations with frequency in the semiconductor material. Also, because we have a multilayer where only the GaAs is pumped, we have a simultaneous index and gain grating.

In this paper, we first give a summary of the modified eigenmode theory that takes these effects into account. We also consider briefly what happens when the periodic structure does not have an even symmetry anymore. (Most of the previous studies considered structures with even symmetry only.) Then, we check the results of eigenmode theory by solving exactly the two layers case. Next, we derive the reflection and transmission coefficients for the interface between a periodic waveguide and a uniform waveguide. Using these results, we are able to compute the total reflectivity of the DFB structure used to fabricate the SELD, as a function of wavelength and we compare this result with the measured reflectivity. We then summarize the experimental data of the fabricated device. Next, we compute the theoretical emission spectrum (below threshold) and compare it to the measured emission spectrum. The model used for this calculation considers the laser as an amplifier driven by spontaneous emission. Finally, we discuss possible improvements to the theory and to the device.

We will use an extension of the eigenmode theory for periodic structures, as first developed in [5]. A good exposition can be found in [6]. The advantage over coupled mode theory (see for example [7]) is that we are really working with independent modes, which makes, in our opinion, the boundary conditions much easier to express. (Although this has been much disputed, see [8,9].) Another advantage is that it allows us to get analytical formulas for the output spectrum of a DFB laser. This is not possible with coupled mode theory [10].

II. General Theory

The equation for the propagation of a scalar wave in a one-dimensional infinite periodic medium is:

$$\frac{d^2 E(z, \lambda)}{dz^2} - [g(z, \lambda) - j\beta(z, \lambda)]^2 E(z, \lambda) = 0 \quad (1)$$

where $E(z, t, \lambda) = E(z, \lambda)e^{j\omega t}$ is an electric field component ($\omega = 2\pi \frac{c}{\lambda}$), $g(z, \lambda)$ is the gain (loss) constant and $\beta(z, \lambda)$ is the propagation constant. Both g and β are periodic in z and depend on λ (the free space wavelength). (The dependence on λ will not always be explicit in the rest of this paper.) The usual assumption is that $(g - j\beta)$ is an even periodic function of z . Most of the review paper by Elachi [1] treats this case. Here, we will only assume that g and β are periodic with the same period Λ , i.e., that we can write:

$$g(z, \lambda) - j\beta(z, \lambda) = g_0(\lambda) - j\beta_0(\lambda) + \sum_{q=-\infty}^{q=\infty} (g_q(\lambda) - j\beta_q(\lambda)) \exp(j2q \frac{\pi}{\Lambda} z) \quad (2)$$

(where g_q and β_q are complex in general).

It is well known that the solutions of (1) are of the Floquet-Bloch type [11]:

$$E(z) = A(z) e^{\Gamma z} + B(z) e^{-\Gamma z} \quad (3)$$

where $A(z)$ and $B(z)$ are periodic functions of z and Γ is the propagation constant, which is written as:

$$\Gamma = G - jK \quad (4)$$

where G is the effective gain and K is the effective propagation constant. The usual interpretation of (3) is to say that $A(z)$ corresponds to a forward propagating mode and $B(z)$ corresponds to a backward propagating mode. We shall see below when this interpretation is correct. When the Bragg condition is nearly satisfied (i.e., β_0 close to K_B), the waves reflected at each interface add constructively and the reflectivity becomes high. In a passive medium, this gives a band of frequency in which Γ has a big negative

real part (as we will see below), which means that there is no propagation in that band. Hence the name stop-band is used, which is similar to the forbidden band in semiconductors. The Bragg condition at normal incidence gives for K_B :

$$\beta_0 = K_B = p \frac{\pi}{\Lambda} \quad (5)$$

Since the band around K_B is the one we are interested in, we will look at $A(z)$ and $B(z)$ in that band. Because $A(z)$ and $B(z)$ correspond to independent solutions of (1), we can treat them separately.

We start by expanding $A(z)$ and $B(z)$ in Fourier series (which we can do since they are periodic):

$$A(z, \lambda) = A_0 + \sum_{q=0}^{q \rightarrow \infty} A_q(\lambda) \exp(j2q \frac{\pi}{\Lambda} z) \quad (6.a)$$

$$B(z, \lambda) = B_0 + \sum_{q=0}^{q \rightarrow \infty} B_q(\lambda) \exp(j2q \frac{\pi}{\Lambda} z) \quad (6.b)$$

Then we substitute (2), (3) and (6) in (1) and by neglecting second order terms and equating terms having the same exponential factor, we get after some approximations [6]:

$$A_{+p}(\lambda) = \frac{j\kappa_+}{G + g_0 + j(\delta + \delta_{eff})} A_0 = s_+(\lambda) A_0 \quad (7)$$

$$B_{-p}(\lambda) = \frac{j\kappa_-}{G + g_0 + j(\delta + \delta_{eff})} B_0 = s_-(\lambda) B_0 \quad (8)$$

where:

$$\begin{aligned} \delta &= K_B - \beta_0(\lambda) & \delta_{eff} &= K_B - K \\ \kappa_+ &= \beta_{+p} + j g_{+p} & \kappa_- &= \beta_{-p} + j g_{-p} \end{aligned} \quad (9)$$

(In equations (7), (8), (9) and in the following, p is a positive integer.) The quantities A_{+p} and B_{-p} represent Bragg-scattered waves from A_0 and B_0 respectively. Their amplitude becomes significant only when β_0 is near K_B . We can then neglect the other components,

so that (3) becomes:

$$E(z, \lambda) = A_0 [1 + s_+(\lambda) \exp(j2K_B z)] e^{\Gamma z} + B_0 [1 + s_-(\lambda) \exp(-j2K_B z)] e^{-\Gamma z} \quad (10)$$

Again, the usual interpretation is to say that the part in A_0 is a forward propagating mode and the part in B_0 is a backward propagating mode.

Let us notice that if (2) is an even function of z , we have: $\kappa_+ = \kappa_-$ and $s_+ = s_-$. In general, we have $|s_+| = |s_-|$ only if $f(z) = g(z) - j\beta(z)$ is: (1) an even function of z ($\kappa_+ = \kappa_-$), (2) an odd function of z ($\kappa_+ = -\kappa_-$), or (3) if $f(z) = (g_0 - j\beta_0) + (g' - j\beta')h(z)$, with $h(z)$ a real periodic function of z . This last case gives: $\kappa_+ = (g' - j\beta')c_p$ and $\kappa_- = (g' - j\beta')c_p^*$ (where c_p is the p th Fourier coefficient of $h(z)$ and c_p^* indicates the complex conjugate of c_p), i.e.: $|\kappa_+| = |\kappa_-|$. The last case includes pure index modulation ($g' = 0$) and pure gain modulation ($\beta' = 0$). We will have $|\kappa_+| \neq |\kappa_-|$ (and thus $|s_+| \neq |s_-|$) only if $g(z)$ and $\beta(z)$ have different "profiles", i.e., if $f(z) = (g_0 - j\beta_0) + [g'h(z) - j\beta'p(z)]$ and $p(z)$ is not proportional to $h(z)$ (both are real functions).

Looking at the scattering of A_{+p} and B_{-p} into A_0 and B_0 , respectively, by the same method as for (7) and (8), we get :

$$A_0 = \frac{-j\kappa_-}{(G - g_0) + j(\delta_{eff} - \delta)} A_{+p} = \frac{1}{s_+} A_{+p} \quad (11)$$

$$B_0 = \frac{-j\kappa_+}{(G - g_0) + j(\delta_{eff} - \delta)} B_{-p} = \frac{1}{s_-} B_{-p} \quad (12)$$

Substituting (7) into (11), or (8) into (12), we can now obtain the characteristic equation (which also defines P):

$$P^2 = (G + j\delta_{eff})^2 = (g_0 + j\delta)^2 + \kappa_+ \kappa_- \quad (13)$$

So that, by using (9) and (13) in (4):

$$\Gamma = G + j\delta_{eff} - jK_B = P - jK_B \quad (14)$$

The solutions of equation (13) in the case of even functions ($\kappa_+ = \kappa_-$) are discussed for example in [1],[6] and [8]. However, all these analysis assume either a pure index modulation or a pure gain modulation and no material dispersion (i.e., the refractive index and the gain are independent of frequency). This assumption is usually valid because conventional edge-emitting DFB laser-diodes have stop-bands that are 2 to 3 nm wide, so that index and gain (loss) variations can be neglected. But in the case of our DFB-SELD structure [3], the stop-band is of the order of 35 nm and gain variations cannot be neglected anymore, especially when the gain changes from negative to positive in the stop-band, as we will see below. Also, in the case of our SELD, we have index and gain modulation at the same time (since it is formed by alternating layers of GaAs and GaAlAs and gain exists only in the GaAs: see reference [2] for details).

Looking at (13), one question comes up: Which root do we choose for P ? One of these roots corresponds to the correct assignement of the forward propagating mode to $A(z)$ and the other root makes $A(z)$ the backward propagating mode. This is an important question since the proper definition of the reflection and transmission coefficients depends on the correct assignement of forward and backward propagation to the modes. In the previous analysis [6,8], P was chosen such that G had the same sign as g_0 , or, equivalently, such that δ_{eff} had the same sign as δ . But this doesn't work in the general case and we have to find another way to decide which root defines the forward propagating mode as:

$$E(z) = A_0 (1 + s_+ \exp(j2K_B z)) e^{\tilde{\gamma} z} \quad (15)$$

Intuitively, we see that in the stop band $K=K_B$ (and $\delta_{\text{eff}}=0$), so that the direction of the net power flow can be found by comparing the intensities of the two components (incident and backscattered) in each mode. Looking at (15), it is obvious that the direction is reversed when $|s_+|$ becomes greater than one.

More rigourously, if (15) is the only non-zero electric field component, dividing the average power flow per unit area by the average energy density, we obtain the energy velocity [6]:

$$v_E = \frac{c}{\beta_0} \frac{K - |s_+|^2(2K_B - K)}{1 + |s_+|^2} \quad (16)$$

where $\beta_0 = \bar{n}\omega\sqrt{\mu_0\epsilon_0}$, \bar{n} being the average effective index and c is the speed of light. So, if (15) really represents a forward wave, v_E has to be positive. From (16), we get then the condition:

$$\frac{1 + |s_-|^2}{2|s_+|^2} \geq \frac{K_B}{K} = \frac{K_B}{K_B - \delta_{eff}} = 1 + \frac{\delta_{eff}}{K_B} \approx 1 \quad (17)$$

since in general $\delta_{eff} \ll K_B$. And this gives us:

$$|s_+| \leq 1 \quad (18.a)$$

And similarly, for the term in B_0 to be the backward propagating wave, we need to have:

$$|s_-| \leq 1 \quad (18.b)$$

If we consider only the cases when $|s_+| = |s_-|$, there is no contradiction between (18.a) and (18.b). There is then always a forward propagating mode and a backward propagating mode. But if we look at the general case, it is possible to have, for example (18.a) being satisfied while (18.b) is not satisfied. To see more clearly what happens, let us define: $P_1 = G + j\delta_{eff}$ and $P_2 = -G - j\delta_{eff}$. Then, looking at (7), (8), (11) and (12), we see that:

$$\begin{aligned} (s_+)_{P_1} &= \frac{1}{(s_-)_{P_2}} \\ (s_-)_{P_1} &= \frac{1}{(s_+)_{P_2}} \end{aligned} \quad (19)$$

where the indices P_1 and P_2 mean that the coefficient is computed using that value for P .

Thus, when $|s_+| = |s_-| = |s|$, we have:

$$|s|_{P_1} = \frac{1}{|s|_{P_2}}$$

This shows that in this case, the choice of the root is unambiguous. Indeed, if P_1 gives a $|s|$ greater than one, P_2 will give $|s|$ smaller than one and vice versa. Looking at the physical interpretation of s_+ and s_- from (7) and (8), we see that (18) simply says that the scattered wave amplitude cannot be bigger than the incident wave amplitude, as we found intuitively above.

But in the general case, if $|k_+|$ is different from $|k_-|$, we will have $|s_+|$ different from $|s_-|$ and in a certain frequency range, we could have for example $|s_+| > 1$ and $|s_-| < 1$. Equations (19) then show that this would be true for both roots of (13). If this is not an effect of the approximations used, and there is no reason to believe that it is, what does this mean? From the discussion above about the direction of the energy flow, the interpretation of this result is that both modes have a net energy flow in the same direction (in this case, backward)! This does not mean that there is no energy going in the forward direction, but only that there is more energy going backwards, i.e. that the reflected wave is greater than the incident wave for one of the modes. This is possible since this is an active structure.

The simplest structure that would exhibit this behavior is a three layers periodic structure, for example: GaAs/Ga_{1-x}Al_xAs/ Ga_{1-y}Al_yAs, with $x \neq y$ and current injection to have gain in the GaAs layer only. This is because in this case $g(z)$ and $\beta(z)$ would have a different "profile". We applied the theory to that three layers structure and for some gain curves, we obtained the phenomenon mentioned above, i.e.: in both modes the net energy flow is in the same direction. We used these results to compute the reflectivity and transmittivity of a finite multilayer structure [12]. We then used a transmission matrix method similar to the one developed in [13] to check the reflectivity and transmittivity obtained with the eigenmode theory. The agreement of the eigenmode theory with the exact results was very good.

III. Two layers periodic structure

The case of the two layers periodic structure is interesting for several reasons. First, it is the basic structure of our surface-emitting laser-diode (SELD) [2,3], which we will analyze below. It is also a very common case in applications such as dielectric mirrors. Second, we can get exact analytical solutions without too much difficulty and this will allow us to compare them with those of the approximate theory of section II (which we will call eigenmode theory).

The structure used for the calculation is shown in figure 2. The gain and propagation constants in one period are given by:

$$g(z,\lambda) - j\beta(z,\lambda) = \begin{cases} g_1(\lambda) - j\beta_1(\lambda) = \Gamma_1(\lambda) & \text{if } -z_1 < z < 0 \\ g_2(\lambda) - j\beta_2(\lambda) = \Gamma_2(\lambda) & \text{if } 0 < z < z_2 \end{cases} \quad (20)$$

and $z_1 + z_2 = \Lambda$, the period of the structure. Let us notice that if we put the origin at $z = -\frac{z_1}{2}$, the function $(g(z) - j\beta(z))$ is even in z . However, to simplify the calculations, we will use the coordinate system of figure 2 and correct later when necessary. We will suppose that we have a plane wave propagating in the direction normal to the plane of the layers, with a linear polarization in the y direction, so that equation (1) is the equation for the y component of the electric field.

Several equivalent methods can be used to solve equation (1) in this case. We will outline the one using solutions of the Floquet-Bloch type, i.e.: we start with equation (3). (Another method is used in [14].) Since $A(z)$ and $B(z)$ correspond to two independent solutions, we can work with them independently of one another. We will work out the solutions for $A(z)$, and $B(z)$ can be obtained simply by replacing Γ by $-\Gamma$ everywhere. So, we substitute (3) in (1) and we get, for $A(z)$:

$$\frac{\partial^2 A}{\partial z^2} + 2\Gamma \frac{\partial A}{\partial z} + (\Gamma^2 - (g(z) - j\beta(z))^2)A = 0$$

Which gives us, with $(g(z) - j\beta(z))$ defined in (20):

$$A(z) = \begin{cases} A_{+1} \exp(\gamma_{+1}z) + A_{-1} \exp(\gamma_{-1}z) & \text{if } -z_1 < z < 0 \\ A_{+2} \exp(\gamma_{+2}z) + A_{-2} \exp(\gamma_{-2}z) & \text{if } 0 < z < z_2 \end{cases} \quad (21)$$

where:

$$\begin{cases} \gamma_{+1} = -\Gamma + \Gamma_1 & \gamma_{+2} = -\Gamma + \Gamma_2 \\ \gamma_{-1} = -\Gamma - \Gamma_1 & \gamma_{-2} = -\Gamma - \Gamma_2 \end{cases}$$

and $A(z)$ is a periodic function of z with period $\Lambda = z_1 + z_2$. Using the continuity of the tangential components of the electric and magnetic fields at $z=0$ and between $z=-z_1$ and $z=z_2$ (since $A(z)$ is periodic), we get after some algebra:

$$\begin{bmatrix} 1 & 1 \\ \Gamma_1 & -\Gamma_1 \end{bmatrix} \begin{bmatrix} A_{+1} \\ A_{-1} \end{bmatrix} = \begin{bmatrix} 1 & 1 \\ \Gamma_2 & -\Gamma_2 \end{bmatrix} \begin{bmatrix} A_{+2} \\ A_{-2} \end{bmatrix} \quad (22.a)$$

and:

$$e^{\Gamma\Lambda} \begin{bmatrix} e^{-\Gamma_1 z_1} & e^{\Gamma_1 z_1} \\ \Gamma_1 e^{-\Gamma_1 z_1} & -\Gamma_1 e^{\Gamma_1 z_1} \end{bmatrix} \begin{bmatrix} A_{+1} \\ A_{-1} \end{bmatrix} = \begin{bmatrix} e^{\Gamma_2 z_2} & e^{-\Gamma_2 z_2} \\ \Gamma_2 e^{\Gamma_2 z_2} & -\Gamma_2 e^{-\Gamma_2 z_2} \end{bmatrix} \begin{bmatrix} A_{+2} \\ A_{-2} \end{bmatrix} \quad (22.b)$$

Eliminating A_{+2} and A_{-2} , we get:

$$\begin{bmatrix} A & B \\ C & D \end{bmatrix} \begin{bmatrix} A_{+1} \\ A_{-1} \end{bmatrix} = \mu \begin{bmatrix} A_{+1} \\ A_{-1} \end{bmatrix} \quad (23)$$

where $\mu = e^{\Gamma\Lambda}$ and:

$$A = e^{\Gamma_1 z_1} \left[\frac{1}{2} \left(\frac{\Gamma_1}{\Gamma_2} + \frac{\Gamma_2}{\Gamma_1} \right) \sinh(\Gamma_2 z_2) + \cosh(\Gamma_2 z_2) \right]$$

$$B = e^{\Gamma_1 z_1} \left[\frac{1}{2} \left(\frac{\Gamma_1}{\Gamma_2} - \frac{\Gamma_2}{\Gamma_1} \right) \sinh(\Gamma_2 z_2) \right]$$

$$C = e^{-\Gamma_1 z_1} \left[\frac{1}{2} \left(\frac{\Gamma_1}{\Gamma_2} - \frac{\Gamma_2}{\Gamma_1} \right) \sinh(\Gamma_2 z_2) \right]$$

$$D = e^{-\Gamma_1 z_1} \left[-\frac{1}{2} \left(\frac{\Gamma_1}{\Gamma_2} + \frac{\Gamma_2}{\Gamma_1} \right) \sinh(\Gamma_2 z_2) + \cosh(\Gamma_2 z_2) \right]$$

Which gives for the eigenvalue μ :

$$\mu = e^{\Gamma\Lambda} = \frac{T}{2} \pm \left[\left(\frac{T}{2} \right)^2 - 1 \right]^{\frac{1}{2}} \quad (24)$$

where T is the trace of the matrix and is given by:

$$T = 2\cosh(\Gamma_1 z_1) \cosh(\Gamma_2 z_2) + \left[\frac{\Gamma_1}{\Gamma_2} + \frac{\Gamma_2}{\Gamma_1} \right] \sinh(\Gamma_1 z_1) \sinh(\Gamma_2 z_2)$$

In the case of no loss and no gain, this reduces to the result obtained in [14]. Let us notice that the matrix in (23) is unimodular since $AD-BC=1$. This also means that the two eigenvalues μ_1 and μ_2 will be inverse of one another:

$$\mu_1 = \frac{1}{\mu_2} \quad \text{and} \quad \begin{cases} \mu_1 = e^{\Gamma\Lambda} \\ \mu_2 = e^{-\Gamma\Lambda} \end{cases} \quad (25)$$

We can check that (24) satisfies this condition. This relation was expected for symmetry reasons: One eigenvalue corresponds to the forward mode and the other one to the backward mode. But here again, we have the same problem as we had for the approximate solution: Which one is the forward mode and which one is the backward mode? Since we have only $e^{\Gamma\Lambda}$, Γ is determined only up to a term of the form $(j2m\frac{\pi}{\Lambda})$ (where m is an integer). This means that $(\Gamma \pm j2m\frac{\pi}{\Lambda})$ is also a solution of (25), for all m . The two possible solutions for a forward wave are obtained by choosing m such that the wave vector has a value close to K_B . We get then:

$$\Gamma = G + j\delta_{eff} - jK_B \quad \text{from } \mu_1 \quad (26.a)$$

$$\Gamma = -G - j\delta_{eff} - jK_B \quad \text{from } \mu_2 \quad (26.b)$$

And we use the same notation as in section II. We see that this is totally equivalent to the choice of the root of equation (13).

Hence, we will use the same criterion as in section II: the direction of the net power flow. To do that, we first have to compute the eigenvectors corresponding to the eigenvalues. We start by rewriting (21) as:

$$A(z) = \begin{cases} A_{+1} (\exp(\gamma_{+1}z) + s_1 \exp(\gamma_{-1}z)) & \text{if } -z_1 < z < 0 \\ A_{+1} (s_3 \exp(\gamma_{+1}z) + s_4 \exp(\gamma_{-2}z)) & \text{if } 0 < z < z_2 \end{cases} \quad (27)$$

Then, from (23), we get:

$$s_1 = \frac{A_{-1}}{A_{+1}} = \frac{\mu - A}{B} = \frac{C}{\mu - D} \quad (28)$$

And, with (22.a):

$$\begin{aligned} s_3 &= \frac{A_{-2}}{A_{+1}} = \frac{1}{2\Gamma_2} (\Gamma_1 + \Gamma_2 + s_1(\Gamma_2 - \Gamma_1)) \\ s_4 &= \frac{A_{-2}}{A_{+1}} = \frac{1}{2\Gamma_2} (\Gamma_1 - \Gamma_2 + s_1(\Gamma_2 + \Gamma_1)) \end{aligned} \quad (29)$$

Notice that if we define: $s_2 = \frac{A_{-2}}{A_{+2}} = \frac{s_4}{s_3}$, we get:

$$s_2 = \frac{s_1 + a}{1 + a s_1} \quad \text{with: } a = \frac{\Gamma_2 - \Gamma_1}{\Gamma_2 + \Gamma_1}$$

This is a bilinear transformation in the complex plane, and if $a \neq 0$ (i.e.: $\Gamma_1 \neq \Gamma_2$), it maps the disk $|s_1| < 1$ onto another disk, but with a part that has $|s_2| > 1$. We can thus not rely on s_1 or s_2 alone to get the direction of the power flow, in the way we looked at s in section II.

To find the direction of the power flow, we will look at the Poynting vector's direction. But, because we have gain and/or loss in the structure, the Poynting vector is not constant along z . Therefore, we will take an average over one spatial period (of the time averaged vector):

$$\langle \vec{S} \rangle = \frac{1}{\Lambda} \int_{-z}^{z} \frac{1}{2} \text{Re}(\vec{E} \times \vec{H}^*) dz \quad (30)$$

where we take: $E_y = A(z) \exp(\Gamma z)$ and $A(z)$ is defined in (27). An explicit formula is derived in Appendix A and it shows that the only non-zero component of the Poynting vector is $\langle S_z \rangle$. The sign of $\langle S_z \rangle$ will then give us the direction of the power flow: positive means forward propagation and negative means backward propagation.

Another way to find the direction of the power flow is to find the s coefficient defined in section II. To find s , we compute the first two coefficients of the Fourier series expansion of $A(z)$ and get s as their ratio. We can then look at $|s|$ as in section II. However, we have to be careful about one thing: the point of even symmetry is at $z = -\frac{z_1}{2}$ and that is where we have to put the origin when we compute s . If we do not do that, we will have a phase difference between the s coefficient computed here and the one defined in section II. Also, we would not have $s_+ = s_- = s$. Taking that into account, we get :

$$s = e^{-jK_B z_1} \left[\frac{\int_{-z_1}^{z_2} A'(z) dz}{\int_{-z_1}^{z_2} A(z) dz} \right] \quad (31)$$

where the exponential factor is due to the change of origin, $A(z)$ is given by (27) and $A'(z)$ also, but with the γ_{\pm} replaced by γ'_{\pm} ($i=1,2$):

$$\gamma'_{\pm} = \gamma_{\pm} - j2K_B$$

Explicitely:

$$\int_{-z_1}^{z_2} A(z) dz = \frac{1 - e^{-\gamma_1 z_1}}{\gamma_1} + s_1 \frac{1 - e^{-\gamma_1 z_1}}{\gamma_1} + s_3 \frac{e^{\gamma_2 z_2} - 1}{\gamma_2} + s_4 \frac{e^{\gamma_2 z_2} - 1}{\gamma_2} \quad (32)$$

And the same for $A'(z)$, but with the γ'_{\pm} .

A comparison of the results obtained with $|s| < 1$ and with the average of the Poynting vector on the examples of the next section shows only negligible differences.

IV. Examples and discussion

To illustrate the theory outlined above, we will use the two-layer structure of our surface-emitting laser-diode [2]. The layer structure is shown in figure 2 and the parameters are given in table 1. Basically, we have alternating layers of GaAs and $\text{Ga}_{0.7}\text{Al}_{0.3}\text{As}$. The thickness of each layer is chosen to be $\lambda_0/4n_i$, where λ_0 is the wavelength at which we want maximum reflectivity and n_i is the index of refraction of the layer (at λ_0). The

GaAs layer will be layer number 1 and the GaAlAs layer will be layer number 2. The loss in the GaAlAs layer is taken as independent of frequency and equal to 10 cm^{-1} (intensity loss). The gain in the GaAs layer depends on the carrier density. A semi-empirical model (based on absorption curves in [15]) was developed to get analytical expressions for the gain as a function of carrier density, temperature and wavelength. Figure 3 shows typical gain curves for three different carrier densities at 300 K. These will be used later in the examples.

Notice that the coupling constant for our structure ($\kappa \approx 4500 \text{ cm}^{-1}$) is two orders of magnitude larger than for edge-emitting semiconductor DFB lasers. Also, since only the GaAs layer will be pumped, we have not only a periodic variation of the index of refraction, but also of the gain constant. This structure has even symmetry and thus $s=s_+=s_-$.

Figure 4 shows the effect on G and δ_{eff} of the introduction of gain and then gain modulation in this structure. In fig. 4(a), there is no loss or gain and we see that G is zero everywhere, except in the stop-band, where it is negative (indicating total reflection, not absorption). In fig. 4(b), a constant (independent of frequency and of z) gain of 2000 cm^{-1} is introduced in the structure. And in fig. 4(c), the periodicity of the gain is taken into account (i.e.: we have gain only in the GaAs layer, but with the same average gain). We see that the effect of gain periodicity cannot be ignored.

Figure 5 shows G and δ_{eff} for different carrier densities. In this case, the gain is not constant but depends on the wavelength. The intensity gain in the GaAs layers used for these examples is shown in figure 3. These calculations were done using the approximate (eigenmode) method of section II and the exact method of section III. The results of the two methods for G and δ_{eff} are undistinguishable at the scale of this figure. The most surprising feature of these results is the sudden jump of G from a negative to a positive value when $N=1.0 \times 10^{18} \text{ cm}^{-3}$ (fig. 5(b)). Notice that this jump occurs at the wavelength where the average gain (g_0) changes from negative to positive.

But this is not as surprising as it seems. If we look again at fig. 4(a) and 4(b), we see that when the gain is changed from negative to positive, G (in the stop-band) changes from a large negative value to a large positive value without going to zero. What happens here, in fig. 5(b), is that the gain changes sign in the stop-band and thus G changes sign also. Mathematically, $|s|$ becomes greater than one and thus we have to switch to the other solution of (24) (or equivalently of (13)), which implies a sign change of G . Figure 6 shows a plot of $|s|$ as a function of wavelength for the two possible solutions ((26.a) and (26.b)). Since $|s| > 1$ means that the direction of the power flow is reversed, we see that the eigenmodes exchange their roles at the point where $|s|=1$: The mode that was propagating in the forward direction now becomes the backward propagating mode and vice-versa.

Physically, as we can see from (16), the velocity of energy propagation is very small in the stop-band ($|s|$ is close to one), because of the multiple reflections. Thus a small loss or a small gain will be amplified a lot by the multiple reflections. In fact, we have [6]:

$$G = g_0 \left[\frac{v}{v_E} \right] \quad (33)$$

where v is the velocity of light in the medium (without the periodicity) and v_E is the energy velocity defined in (16). But this jump is only a mathematical artifact due to the method used here. The rate of change of the energy density (which is equal to $g_0 v = G v_E$, see [6]) is a continuous function of wavelength. If we compute the reflectivity or transmittivity of a finite multilayer with these formulas, we get a perfectly continuous curve (as we will see below).

Figures 5 and 6 also show that for $N = 0.2 \times 10^{18} \text{cm}^{-3}$ and $N = 2.0 \times 10^{18} \text{cm}^{-3}$, this phenomenon does not occur. For $N = 0.2 \times 10^{18} \text{cm}^{-3}$, the gain is always negative and we don't have any problem. For $N = 2.0 \times 10^{18} \text{cm}^{-3}$, the sign change of the gain (g_0) occurs outside of the stop-band and we see that G changes sign also, but without any

discontinuity. Figures 5(a) and 5(c) show that, for these cases, there is no exchange of roles between the two modes.

In figure 7, we compare the real and imaginary part of s , as computed by the approximate method (eq.(7)) and by the exact method (eq.(31)). We see that the difference is small and that for $N = 1.0 \times 10^{18} \text{cm}^{-3}$, the discontinuity occurs at exactly the same wavelength. From this and the fact that G and δ_{eff} are correct within a few percents with the approximate method, we can conclude that the approximate method is a good approximation. We are interested in the s coefficient because it will be used in the next section to compute reflection coefficients and the emission spectrum of our DFB-SEL.

V. Reflection and transmission coefficients

We saw above that for a periodic one-dimensional medium with even symmetry, a good approximation of the electric field is given by:

$$E(z) = A_0(1+s_f)e^{\Gamma z} + B_0(1+s_b)e^{-\Gamma z} \quad (34.a)$$

where A_0 and B_0 are the amplitude coefficients for the forward and backward propagating modes respectively and:

$$\begin{aligned} s_f &= s \exp(j2K_B z) \\ s_b &= s \exp(-j2K_B z) \end{aligned} \quad (34.b)$$

Γ , K_B and s have been defined in equations (4), (5) and (7), respectively.

From these definitions, we can immediately find the forward propagation factor from z_1 to z_2 (with $z_1 < z_2$) [6], that is the factor D_f such that $E(z_2) = D_f E(z_1)$:

$$D_f = \frac{1 + s \exp(j2K_B z_2)}{1 + s \exp(j2K_B z_1)} e^{\Gamma L} = \frac{1 + s_{f2}}{1 + s_{f1}} e^{\Gamma L} \quad (35.a)$$

where $L = z_2 - z_1$. Similarly, for the backward propagating factor D_b (from z_2 to z_1), such that $E(z_1) = D_b E(z_2)$, we get:

$$D_b = \frac{1 + s \exp(-j2K_B z_1)}{1 + s \exp(-j2K_B z_2)} e^{\Gamma L} = \frac{1 + s_{b1}}{1 + s_{b2}} e^{\Gamma L} \quad (35.b)$$

One important point when using these formulas is that the origin of the z axis has to be at a point of even symmetry. Otherwise, we would have made a mistake because the s coefficient for the forward and backward modes would have a different phase (see the definitions (7) and (8)).

A. One interface

Let us now look at what happens at the interface between a periodic region and a uniform region (Fig.8). Expression (34) for the electric field in a periodic region is only an approximation, but, as we saw above, it is a good approximation. We will thus suppose in the rest of this paper that the electric field in a periodic region is of the form given by (34). In the uniform region, the electric field will be given by:

$$E_u(z) = A'_0 e^{-j\Gamma_u(z-z_1)} + B'_0 e^{j\Gamma_u(z-z_1)} \quad (36)$$

where Γ_u is the complex propagation constant in the uniform region and A'_0 and B'_0 are the amplitudes of the forward and backward propagating modes respectively. z_1 is the position of the interface, which we can subtract from z in (36) to simplify the calculations, since, for a uniform region, the choice of the origin is arbitrary.

Figure 8 shows the meaning of the different reflection and transmission coefficients we are going to compute. To find these coefficients, we express the continuity of the tangential electric and magnetic fields at $z=z_1$ and we get:

$$\begin{aligned} (1 + s_{f1})A_0 e^{\Gamma z_1} + (1 + s_{b1})B_0 e^{-\Gamma z_1} &= A'_0 + B'_0 \\ (s_{f1} - 1)K_B A_0 e^{\Gamma z_1} + (1 - s_{b1})K_B B_0 e^{-\Gamma z_1} &= -\beta_u A'_0 + \beta_u B'_0 \end{aligned} \quad (37)$$

where the index 1 for s_f and s_b indicates that they are computed at $z=z_1$ and where we used $\Gamma = K_B$ (we are working near the Bragg wavelength) and $\Gamma_u \approx \beta_u$. Now, to find, for example, R_1 , we have to take the ratio of the backward and forward propagating electric fields at the interface in the periodic region:

$$R_1 = \frac{E_{p,back}(z_1)}{E_{p,forw}(z_1)} = \frac{B_0(1 + s_{b1})e^{-\Gamma z_1}}{A_0(1 + s_{f1})e^{\Gamma z_1}} \quad (38)$$

when there is no mode incident from the right ($B'_0=0$). We solve then (37) to find B_0/A_0 and plug the result in (38). The other coefficients are found in a similar way. We get:

$$\begin{aligned} R_1 &= \frac{r-s_{f1}}{1-rs_{b1}} \frac{1+s_{b1}}{1+s_{f1}} & R_2 &= \frac{s_{b1}-r}{1-rs_{b1}} \\ T_1 &= (1+r) \frac{1-s_{f1}s_{b1}}{(1-rs_{b1})(1+s_{f1})} & T_2 &= (1-r) \frac{1+s_{b1}}{1-rs_{b1}} \end{aligned} \quad (39)$$

where r is the reflection coefficient due to the change in propagation constant:

$$r = \frac{K_B - \beta_u}{K_B + \beta_u} = \frac{\bar{n} - n_u}{\bar{n} + n_u} \quad (40)$$

where \bar{n} is the effective index of refraction in the periodic region at the Bragg wavelength ($\bar{n} = K_B/k_0$ and $k_0 = 2\pi/\lambda$). and n_u is the index of refraction of the uniform region at the same wavelength.

We see that in the limit of no periodicity (s going to zero), we recover the usual expressions for the reflection and transmission coefficients. And in the limit r going to zero, we get the same results as in [6]. Now, if the periodic region is on the right instead of on the left as in figure 8, we just have to exchange s_f with s_b , R_1 with R_2 and T_1 with T_2 in (39) to get the formulas for this case. If we call R_3 the new R_1 we obtain in this way, R_4 the new R_2 and so on and if we replace z_1 by z'_2 , we find:

$$\begin{aligned} R_3 &= \frac{s'_{f2}-r'}{1-r's'_{f2}} & R_4 &= \frac{r'-s'_{b2}}{1-r's'_{f2}} \frac{1+s'_{f2}}{1+s'_{b2}} \\ T_3 &= (1-r') \frac{1+s'_{f2}}{1-r's'_{f2}} & T_4 &= (1+r') \frac{1-s'_{b2}s'_{f2}}{(1-r's'_{f2})(1+s'_{b2})} \end{aligned} \quad (41)$$

B. Phase shifter

In the following, we will also need expressions for global reflection (R' , R'') and transmission (T' , T'') coefficients of a phase shifter. By phase shifter, we mean, in this paper, a uniform region between two periodic regions (see figure 9). The R_i 's and T_i 's

($i=1,2,3,4$) are the coefficients given by (39) and (41). Notice that we are using two different coordinate systems. This is necessary because, as mentioned earlier, we have to put the origin at a point of even symmetry in a periodic region. But, in general, it is impossible to have the origin (or its translation by a multiple of the period Λ) at a point of even symmetry in the two periodic regions at the same time. Hence the use of z for the left region and z' for the right region.

The propagation factor for a uniform section of length L_u and with propagation constant $\Gamma_u = \beta_u + j g_u$ is:

$$P_u = \exp(-j\Gamma_u L_u) \quad (42)$$

We will suppose here that the reflection coefficient r is equal to zero (i.e., $\bar{n} = n_u$, which is approximately the case in our laser structure). We get then, using the method of multiple reflections:

$$R' = \frac{P_u^2 s'_{f2} - s_{f1}}{1 - P_u^2 s_{b1} s'_{f2}} \frac{1 + s_{b1}}{1 + s_{f1}} \quad (43.a)$$

$$T' = \frac{P_u(1 - s_{f1} s_{b1})}{1 - P_u^2 s_{b1} s'_{f2}} \frac{1 + s'_{f2}}{1 + s_{f1}} \quad (43.b)$$

$$R'' = \frac{P_u^2 s_{b1} - s'_{b2}}{1 - P_u^2 s_{b1} s'_{f2}} \frac{1 + s'_{f2}}{1 + s'_{b2}} \quad (43.c)$$

$$T'' = \frac{P_u(1 - s'_{f2} s'_{b2})}{1 - P_u^2 s_{b1} s'_{f2}} \frac{1 + s_{b1}}{1 + s'_{b2}} \quad (43.d)$$

The prime on the s indicates that the s coefficient for the right region can be different from the one for the left region.

VI. Reflectivity

Figure 10 and table 1 show the layer structure used for our surface emitting laser diode (SELD). From the top, we have 20 pairs of layers, consisting of one GaAs layer and one GaAlAs layer (each layer is one quarter of a wavelength thick), then we have a

quarter-wavelength GaAs layer acting as phase-shifter and finally 60 more pairs of GaAs/GaAlAs above the GaAs substrate (see [2,3]). This structure was chosen because it allows lasing in the middle of the stop-band [16], and thereby avoids the degeneracy problem of usual DFB lasers. The number of pairs at the top is smaller so that most of the power output is through the surface and not in the substrate. The structure was grown by metallo-organic chemical vapor deposition (MOCVD) for the devices we will present here, but we have also several wafers grown by molecular beam epitaxy (MBE).

In this calculation, we will consider only plane waves at normal incidence, coming from the air. Figure 11 shows the model used to compute the reflectivity. L_1 is the length of the 20 pairs section, L_2 is the length of the phase shifter and L_3 is the length of the 60 pairs section. The R_i 's and the T_i 's we need are given by the formulas derived in the previous section and are summarized in Appendix B.

Using the method of multiple reflections, we find the total power reflectivity to be given by:

$$R_p = |R_T|^2 \quad (44.a)$$

and

$$\begin{aligned} R_T &= R_1 + \frac{T_1 T_2 R_{eff} P_1 P_2}{1 - R_2 R_{eff} P_1 P_2} \\ R_{eff} &= R_3 + \frac{T_3 T_4 R_5 P_3 P_4}{1 - R_4 R_5 P_3 P_4} \end{aligned} \quad (44.b)$$

where the P_i 's are propagation factors of the type given by (35) (D_f and D_b) and R_{eff} is an effective reflection coefficient for the phase-shifter and everything that is to its right (in fig. 11). If we look at the formulas we obtained, we see that a lot of factors of the form $(1+s_f)$ or $(1+s_b)$ can be cancelled out. This can be done by omitting the factors between square brackets in Appendix B.

Before we can compute the power reflectivity of our structure, we need to define two more characteristics: the index of refraction and the absorption as functions of

wavelength. We will assume that the index of refraction is constant and that the absorption coefficient in the GaAlAs layer is constant and equal to 10 cm^{-1} (intensity coefficient). For the GaAs layer, we will use:

$$\alpha(E) = \left[\frac{1}{\beta} + \frac{1}{\gamma} \right]^{-1} \quad [\text{cm}^{-1}]$$
$$\beta = \exp(4.85E + 1.9552)$$
$$\gamma = \exp(118.84E - 159.9106) \quad (45)$$

where E is the photon energy in eV. This formula was obtained by fitting to a measured absorption curve for small p-type doping given in [15].

Now we can compute the power reflectivity of our structure. Figure 12(a) gives the result of the calculation for the structure as defined by figure 10 and Table 1. In Figure 12(b), we see a typical experimental result. The measurements were made using a Perkin-Elmer Lambda 9 spectrometer with the Absolute Reflectance Accessory. In this apparatus, the beam normally reflects twice from the sample at two different positions, with an angle of 8 degrees. Because of the small size of the sample and of its non-uniformity, an aluminium mirror was substituted at the second reflection point. We did a first measurement with the sample, then replaced it with an aluminium reference mirror. This allowed us to compute the absolute reflectivity, knowing the reflectivity of the aluminium. The fact that we were not at normal incidence (but 8 degrees off) slightly increases the apparent thickness of the layers (less than 1%), but can otherwise be neglected.

We can see that the experimental result is similar to the theoretical result of fig. 12(a), but that there are some differences also. The main difference is the double dip in the middle of the stop-band for the experimental result. This can be explained by looking at what happens when the thickness of each layer changes by one lattice constant ($a=5.65$ Angstroms). This gives us a change of thickness of about 0.9 %, which, for an original Bragg wavelength of 890 nm (in vacuum), corresponds to a change of about 8 nm. This

corresponds approximatively to the spacing of the two dips. What happens is that the grown structure is not uniform across the wafer and the spot size for the reflectivity measurement is several millimeters. The measured reflectivity is thus an average of two different thicknesses.

We varied the parameters slightly to try to reproduce the experimental curve. Our best result is the theoretical curve in Fig. 12(b) (but it is not an optimal fit). It was obtained by a weighted average between a Bragg wavelength (λ_0) of 889 nm (70 %) and a $\lambda_0 = 897$ nm (30 %), with the thickness of the top GaAs layer (the one in contact with air) reduced to 37 nm (instead of 67 nm). (This reduction in thickness could happen during wafer processing and handling.)

We did not try to improve the agreement between theory and experiment because it depends on too many unknown parameters, such as the exact dependence of the loss on wavelength, and because the theory used here is only an approximation. We also neglected the variation of the index of refraction with wavelength. However, we get correctly the main characteristics of the curves and this gives us confidence for applying the theory to the calculation of the emission spectrum of the SELD (in section VIII).

VII. The surface-emitting laser diode

As described previously in [2] and [3], the surface emitting laser diodes (SELD) are fabricated by starting from wafers having the layer structure described above (Fig. 10 and Table 1). Mesas with dimensions ranging from 2×8 to $3 \times 17 \mu\text{m}^2$ at the top surface are formed by wet etching. Then a n-type $\text{Ga}_{0.6}\text{Al}_{0.4}\text{As}$ cladding layer is grown around the mesas by selective liquid phase epitaxy (LPE). Finally, a lateral pn junction is formed by selective zinc diffusion through an opening in a silicon nitride film, at a distance of 3 to 4 μm away from the edge of the mesa. Figure 13(a) shows the structure of the laser and Fig. 13(b) is a scanning electron microscope (SEM) picture of a laser. The zinc diffusion region is brighter in this picture. The total thickness of the structure is about 10 μm .

Since the GaAs/GaAlAs multilayer is completely surrounded by GaAlAs, carrier confinement in this structure should be comparable with that of buried heterostructures. Carriers are injected predominantly in the GaAs layers and therefore we will assume in the model that only the GaAs layers are pumped. There is however the possibility of current leakage around the mesa. We believe this happens at high currents.

Figure 14 shows the light output versus dc current characteristics (L-I curve) of a SELD at room temperature. We get what looks like typical threshold currents in the range from 2 to 10 mA and differential quantum efficiencies from 0.3 % to 1.36 %. Powers of 0.5 mW for a current of 50 mA have been observed for CW operation at room temperature. More recently, we obtained quantum efficiencies up to 5 % for some devices. Unfortunately, they were accidentally destroyed before their spectrum could be measured.

Observation of the near-field pattern shows [2,3] that the light-emitting region is confined within the rectangular top surface of the multilayer (at least when the current is not too high). The far-field pattern is circular [2,3] and its beam divergence angle, for a current of 20 mA, is 7 to 8 degrees. However the circular emission pattern is surprising for a device with a rectangular emission surface. The 7 to 8 degrees angle corresponds roughly to a width of about 3 μm for the rectangular opening, but the length of about 15 μm should give a much narrower beam in that direction (about 3 degrees), if it were a diffraction limited beam. Obviously, the beam is not diffraction limited in that direction. A reason for that could be that there is no coherence between points more than 3 μm apart.

Figure 15 shows the spectrum of the SELD at different currents, for CW operation at room temperature. We see that there is a sharp emission line at 884 nm which becomes obvious for a drive current of 1.6 mA. This is consistent with the L-I curve, which shows what looks like a 2 mA threshold current. The half-width is rather large (1.5 to 3 nm) compared to conventional edge-emitting laser diodes. The total width of

the emission spectrum is also large (about 50 nm), compared to edge-emitting lasers.

In view of these results, one might ask whether these devices are really lasing? We think they are. There may be several reasons for the low quantum efficiency: leakage current around the mesa, non-radiative recombination at interfacial defects if the LPE was not very good and a big spontaneous emission component. We explain below how the shape of the mesa can lead to a lot of parasitic spontaneous emission which lower the quantum efficiency and can also affect the spectrum.

VIII. Emission spectrum of the SELD

In this section, we develop a model (figure 16) to reproduce and explain the emission spectrum, at least below threshold. It is very similar to the one used to compute the reflectivity and we make the same assumptions, except that we will now have gain in the pumped section (which is taken as being the zinc diffused region). In addition, we assume that this pumped section has a uniform carrier density (in the GaAs part of the layers) and that the unpumped region is uniform and lossy. These assumptions are rough approximations, but they allow us a relatively easy calculation using what we did in the previous sections.

The reflection and transmission coefficients are given in Appendix B. E_1 , E_4 and E_2 , E_3 are the electric fields amplitudes of the forward and backward propagating modes respectively, at the two interfaces of the phase shifter region (L_2). E_{out} is the amplitude of the electric field of the light output. The S_i 's are the equivalent sources for the electric fields at the interfaces due to the spontaneous emission in sections L_1 and L_3 (we neglect the spontaneous emission in the phase shifter).

If we express the electric fields as functions of one another and of the S_i 's, we get the following system of equations:

$$\begin{aligned} E_1 &= R_2 P_1 P_2 E_2 + R_2 P_1 S_1 + S_2 \\ E_2 &= R_3 E_1 + T_4 E_3 \\ E_3 &= R_5 P_3 P_4 E_4 + R_5 P_4 S_4 + S_3 \\ E_4 &= R_4 E_3 + T_3 E_1 \\ E_{out} &= T_1 P_1 E_2 + T_2 S_1 \end{aligned} \tag{46}$$

If we eliminate the E_i 's, we find:

$$E_{out} = (R_2 T_2 P_1 P_2 \frac{N}{D} + T_2) S_1 + (T_2 P_2 \frac{N}{D}) S_2 + (T_2 P_2 \frac{T_4}{D}) S_3 + (R_5 T_2 P_2 P_4 \frac{T_4}{D}) S_4 \quad (47)$$

where:

$$N = R_3 + R_5 P_3 P_4 (T_3 T_4 - R_3 R_4) \\ D = (1 - R_2 R_3 P_1 P_2)(1 - R_4 R_5 P_3 P_4) - R_2 R_5 T_3 T_4 P_1 P_2 P_3 P_4$$

But what we are interested in is the output power. To convert the relation (47) between the electric fields to a relation between the power in the modes, we have to remember that the S_i 's are really of the form given by (34), i.e.:

$$S_i = S_{i0} (1 + s e^{\pm 2j K_B z_i}) e^{\pm \Gamma z_i}$$

while we have:

$$E_{air}(z) = E_0 e^{-j \frac{2\pi}{\lambda} (z - z_1)} \quad \text{and} \quad E_{out} = E_{air}(z_1) = E_0$$

Then, with the same cancellations of factors as for the reflectivities, we get:

$$|E_{out}|^2 = |R_2 T_2 P_1 P_2 \frac{N}{D} + T_2|^2 |S_{10}|^2 + |T_2 P_2 \frac{N}{D}|^2 |S_{20}|^2 + |T_2 P_2 \frac{T_4}{D}|^2 |S_{30}|^2 \\ + |R_5 T_2 P_2 P_4 \frac{T_4}{D}|^2 |S_{40}|^2 = \sum_{j=1}^4 C_j |S_{j0}|^2 \quad (48)$$

where we have taken into account the fact that the S_i 's are not coherent with one another. This formula is valid with the reflection and transmission coefficients as given in Appendix B when we omit the factors between square brackets. Now, by computing the Poynting vector for a field of the type of (34), we find a relation between the power density p_j and $|S_{j0}|^2$:

$$p_j = \frac{1}{2\omega\mu_0} [K - |s|^2 (2K_B - K)] |S_{j0}|^2$$

And for the output power:

$$P_{out} = \frac{k_0}{2\omega\mu_0} |E_0|^2$$

This gives us then the output power spectral density:

$$P_{out} = \frac{k_0}{K - |s|^2(2K_B - K)} \left\{ \sum_{j=1}^4 C_j p_j \right\} \quad (49)$$

where the C_j 's were defined in (48) and the p_i 's (defined below) are the spectral power densities due to the spontaneous emission.

We see immediately from (48) and (49) that we will have lasing when $D=0$. This condition will give us the wavelengths of the modes and the corresponding gain thresholds. (Do not forget that the reflection and transmission coefficients are wavelength dependent and that the propagation factors depend on the wavelength and on the gain.)

If we solve the equation $D=0$, we get several solutions, each one corresponding to a mode. If we use $\lambda_0 = 890$ nm and a phase shifter thickness reduced to $0.4 \text{ } \mu\text{m}$ (instead of $0.5 \text{ } \mu\text{m}$), we will see below that we get the best spectrum adjustment. This gives us a mode at 884 nm with a threshold intensity gain of about 44 cm^{-1} (for the material gain of GaAs). With the model for the gain developed below, this corresponds, at that wavelength to a threshold carrier density of about $1.6 \times 10^{18} \text{ cm}^{-3}$. We can now estimate the threshold current with:

$$I_{th} = q \frac{tldN_{th}}{\tau}$$

where $t = 2 \text{ } \mu\text{m}$ and $l = 15 \text{ } \mu\text{m}$ are the mesa dimensions and $d = 3 \text{ } \mu\text{m}$ is the active layers' thickness (without the GaAlAs layers) and $\tau = 4 \text{ ns}$ is the spontaneous lifetime (q is the electron charge). This gives us $I_{th} \approx 7.76 \text{ mA}$, which is in the range of observed threshold currents. The other modes, which will give humps in the spectrum, have much higher threshold gains (several thousands cm^{-1} at least).

Let us now find expressions for the p_i 's in terms of the spontaneous emission spectral density rate and the device parameters. To simplify the calculations, we will suppose a uniform spontaneous emission in the whole section (which is consistent with the uniform carrier density) and we correct then for the fact that we have emission only in the

GaAs layers with a factor f . This factor f is equal to the ratio of the thickness of one GaAs layer to one period. Now, to get the p_i 's, we sum incoherently the amplified spontaneous emission in each section. For example, we get for p_1 :

$$p_1 = f \frac{t l}{2} E r_{sp}(E) \gamma \int_0^{L_1} |e^{\Gamma z}|^2 dz$$

where γ is the fraction of the spontaneous emission coupling to the cavity mode, E is the photon energy (in Joules) and $r_{sp}(E)$ is the spontaneous emission spectral density rate per unit volume. The cavity cross-section, $t \times l$, is taken as constant. The factor one half comes from the fact that only one half of the spontaneous emission coupled to the cavity mode goes in one direction. Using equation (14), we have:

$$|e^{\Gamma z}|^2 = e^{2Gz}$$

which gives us:

$$p_1 = p_2 = f \frac{t l}{2} E r_{sp}(E) \gamma \left[\frac{e^{2GL_1} - 1}{2G} \right] \quad (50.a)$$

and:

$$p_3 = p_4 = f \frac{t l}{2} E r_{sp}(E) \gamma \left[\frac{e^{2GL_2} - 1}{2G} \right] \quad (50.b)$$

Putting (49) and (50) together, we find:

$$p_{out} = f \frac{t l}{2} E r_{sp}(E) \left[\frac{\gamma k_0}{K - |s|^2 (2K_B - K)} \right] \left\{ (C_1 + C_2) \left[\frac{e^{2GL_1} - 1}{2G} \right] + (C_3 + C_4) \left[\frac{e^{2GL_2} - 1}{2G} \right] \right\} \quad (51)$$

Finally, let us notice that this is $p_{out}(E)$. If we want $p_{out}(\lambda)$, since $E = hc/\lambda$, we have to use:

$$p_{out}(\lambda) = p_{out}(E) \left| \frac{dE}{d\lambda} \right| = p_{out}(E) \frac{E^2}{hc}$$

The factor between square brackets in (51) has to be examined carefully. It can be shown [17] that in a periodic waveguide, γ becomes dependent on wavelength and contains a factor that cancels the denominator. The expression between square brackets is

then equal to the γ in an uniform waveguide times a factor of order unity depending on wavelength. In this paper, we will neglect that factor, although it modifies somewhat the spectrum [17].

Now, only two factors remain to be specified before we can compute the emission spectrum. These are the spontaneous emission rate $r_{sp}(E)$ and the GaAs material gain $g_1(E)$. Both will be functions of the carrier density. For the spontaneous emission rate, we know [15] that for the non-thermal equilibrium case, we have:

$$r_{sp}(E) = \frac{1}{\pi^2 \hbar^2 v^2} \frac{-E^2 g(E, N)}{e^{(E - \Delta E_F)/k_B T} - 1} \quad [J^{-1} m^{-3} s^{-1}] \quad (52)$$

where v is the light's velocity in the material, E is the photon energy, k_B is Boltzmann's constant and T is the temperature. The difference between the electron and hole quasi-Fermi levels (ΔE_F) can be computed from the carrier density N by using the Fermi-Dirac distribution and the parabolic approximation for the band extrema. Using this and experimental absorption curves from [15], we developed a semi-empirical model for the gain as a function of E , N , T and N_A , where N_A is the acceptor concentration (zinc gives a p-type doping). Figure 17(a) shows typical gain curves for different carrier densities, at constant temperature, and figure 17(b) for different temperatures, at constant carrier density.

At this point, we have not yet incorporated rate equations in our model to allow us to compute the L-I characteristic. Therefore, we will postulate a carrier density and compute the shape of the emission spectrum, but we will not try to get the absolute values. Thus we do not need to worry about the constants in (50) and (51). The final result is shown in figure 18(a) and can be compared with the experimental spectra shown in figure 15 and 18(b). The resolution of the measurements in figure 18(b) is 0.7 nm. Figure 18(b) was measured at much higher currents, in pulsed mode operation. We see that the theory and the experiment are similar (with reasonable values of the parameters), but that the relative intensities of the peaks are not reproduced. This may be due to the fact that our

model is linear and cannot go above threshold since, as mentioned above, we do not use a rate equation. Another problem is that we assumed a uniform carrier density in the pumped section. This is most probably not true because the carrier injection is not uniform and the field in the cavity is not uniform either. The field is maximum at the phase shifter and decreases exponentially above and below (see [16]). This will introduce a non-uniformity in the carrier distribution that cannot be compensated for by the carrier diffusion because of the layered structure. So, in the regions of low field, we will have more spontaneous emission. Also, the bottom of the mesa, which is a low field region, is much wider than the top (fig. 13(b)). This means that the light emitted on the sides sees a different vertical structure and may alter the emission spectrum.

Notice in figure 18 the slight shift in peak position with increasing carrier density. This is due to the change in the index of refraction of the GaAs layers with the carrier density. In our model, we used [6]:

$$\Delta n = 2.2 \times 10^{-8} N^{1/3} - 1.6 \times 10^{-14} N^{2/3} - 9.75 \times 10^{-22} N \quad (20)$$

where Δn is the index change and N is the carrier density in cm^{-3} . We also incorporated a dependence on temperature [15]:

$$\Delta n = 4 \times 10^{-4} (T - 300) \quad (21)$$

where T is the absolute temperature in Kelvins. We assumed that the change in index of refraction was the same for the GaAs and the GaAlAs layers.

This effect of the temperature on the index of refraction is responsible for the shift in peak positions that we observe in figure 19, which shows the emission spectrum at several temperatures (with the carrier density kept constant). Figure 19(a) shows the theoretical calculations and figure 19(b) shows the experimental result. Once again, the agreement is good, except for the relative peak amplitudes. We notice that when the temperature changes, the relative peak amplitudes change also. This is due in part to the modification of the gain spectrum with temperature, as shown in figure 17(b). This

modification is due to a number of factors, the main ones being the change of the bandgap and that of the density of states with temperature. We see that the wavelength of maximum gain changes and so does the value of that maximum gain. When the mode position coincides with the maximum gain, the peak amplitude is maximum. This occurs around 300K for the peak at 884 nm (at 300K). When we change the temperature, the maximum gain and the mode shift at different rates and, as a result, the peak amplitude decreases.

IX. Conclusions

In this paper, we have developed a way to compute the propagation constants of the modes in a one-dimensional periodic structure over a certain band of frequency, when material dispersion is present. The correct interpretation of the solutions is based on the direction of the power flow. This led us to discover that, for a structure with even symmetry, the backward and forward propagating modes exchange their roles when the gain changes sign in the stop-band. These results were checked in the two layers case by obtaining an exact solution. We then derived the formulas for the reflection and transmission coefficients at the interface between a periodic and a uniform section.

Using these results, we developed a model to compute the emission spectrum of the surface-emitting laser diode (SELD) below threshold. We made several assumptions in this model. The main ones are: (1) The Bloch wave description for the electric field is accurate. (2) The carrier density is uniform in the pumped region. (3) The horizontal cross-section (parallel to the layers) is constant from the top to the bottom. We think that the first assumption is a good approximation, but that the second and third ones are partially responsible for the discrepancies between the theory and the experimental results. Our confidence in the first assumption comes from the good agreement between theory and experiment for the reflectivity of the layered structure (section VI).

As mentioned in section VIII and in the previous paragraph, the assumption of a uniform carrier density is probably not a good one. A variation in carrier density will result in a longitudinal gain non-uniformity, which may change the threshold gain for the modes and hence explain the difference in the relative peak amplitudes between theory and experiment. The fact that the cavity is really trapezoidal (and not rectangular, as implied by the third assumption) may give a significant contribution to spontaneous emission and modify the spectrum, since the light emitted on the sides sees a different vertical structure (see fig. 13).

In conclusion, we can say that our model is sufficient to explain a lot of the observed characteristics of the spectrum. To get a better agreement, we need to extend its validity above threshold. To do that, we need to incorporate rate equations for the carrier density. The next step would be to take into account the longitudinal non-uniformity of the carrier density, but that is much more difficult and can probably not be done using the theory developed in this paper. One way to do it would be to use a transfer matrix for each period (see for example [13]) and solve self-consistently.

On the experimental side, we are now working on several improvements, such as using reactive ion-beam etching to get vertical side-walls to the cavity, which would avoid the problems due to a trapezoidal cavity. We are considering replacing the zinc diffusion, which is difficult to control, by a two steps LPE process. We grow first n-type GaAlAs on one side of the mesa, then p-type GaAlAs on the other side, so that we still get a transverse p-n junction. We are also working on distributed Bragg reflector (DBR)-type structures, where we have a relatively long uniform active region (3-5 μm) between a bottom unpumped multilayer and a top dielectric multilayer.

Acknowledgments

The authors acknowledge contributions from Jane J. Yang of Space and Technology group, TRW, from Lillian Z. Gacusan and Larry Dries of the Lockheed Missiles & Space Company. We would also like to thank Professor John R. Whinnery for his continuous support and Mike Werner, Daryoosh Vakshoori and Myra Boenke for their suggestions and stimulating discussions.

This work is supported by Lockheed Missiles & Space Company, by a grant from the California State Micro program and in part by the Office of Naval Research (ONR).

Appendix A

In this appendix, we derive the exact expression of the average over one period of the time averaged Poynting vector. We start with an electric field of the form:

$$E_y = \left[c_1 e^{(g-j\beta)z} + c_2 e^{-(g-j\beta)z} \right] e^{j\omega t} \quad (A.1)$$

Using Maxwell's equations, this gives:

$$H_x = -\frac{j}{\omega\mu_0} (g-j\beta) \left[c_1 e^{(g-j\beta)z} - c_2 e^{-(g-j\beta)z} \right] e^{j\omega t} \quad (A.2)$$

The time averaged Poynting vector is:

$$\vec{S} = \frac{1}{2} \text{Re}(\vec{E} \times \vec{H}^*) = -\frac{1}{2} \text{Re}(E_y H_x^*) \vec{e}_z \quad (A.3)$$

Which gives us:

$$S_z = \frac{\beta}{2\omega\mu_0} \left[|c_1|^2 e^{2gz} - |c_2|^2 e^{-2gz} \right] + \frac{g}{\omega\mu_0} \text{Im} \left[c_1^* c_2 e^{j2\beta z} \right] \quad (A.4)$$

Now, for $E_y = A(z)e^{j\Gamma z}$, where $A(z)$ is given by (27), the average of S_z over one spatial period is given by:

$$\begin{aligned} \langle S_z \rangle &= \frac{1}{\Lambda} \int_{-z_1}^{z_2} S_z dz \\ &= \frac{|A_1|^2}{\omega\mu_0\Lambda} \left\{ \frac{\beta_1}{2} \left[\frac{1-e^{-2g_1 z_2}}{2g_1} + |s_1|^2 \frac{e^{2g_1 z_2}-1}{2g_1} \right] \right. \\ &\quad \left. + \frac{\beta_2}{2} \left[|s_3|^2 \frac{e^{2g_2 z_2}-1}{2g_2} + |s_4|^2 \frac{1-e^{-2g_2 z_2}}{2g_2} \right] \right. \\ &\quad \left. + \text{Im} \left[g_1 s_1 \frac{1-e^{-j2\beta_1 z_1}}{j2\beta_1} + g_2 s_3^* s_4 \frac{e^{j2\beta_2 z_2}-1}{j2\beta_2} \right] \right\} \quad (A.5) \end{aligned}$$

Appendix B

This appendix gives the expressions for the reflection and transmission coefficients and for the propagation factors used to compute the reflectivity, in (44), and the emission spectrum, in (46)-(51). With $L_1 = z_2 - z_1$ and $L_3 = z'_4 - z'_3$ (fig. 11 and 16), we have:

$$\begin{aligned}
 R_1 &= \frac{s_{f1} - r}{1 - r s_{f1}} & T_1 &= \frac{1 - r}{1 - r s_{f1}} [1 + s_{f1}] \\
 R_2 &= \frac{r - s_{b1}}{1 - r s_{f1}} \left[\frac{1 + s_{f1}}{1 + s_{b1}} \right] & T_2 &= (1 + r) \frac{1 - s_{f1} s_{b1}}{1 - r s_{f1}} \left[\frac{1}{1 + s_{b1}} \right] \\
 R_3 &= \frac{P_u^2 s_{f3} - s_{f2}}{1 - P_u^2 s_{b2} s_{f3}} \left[\frac{1 + s_{b2}}{1 + s_{f2}} \right] & T_3 &= \frac{P_u (1 - s_{f2} s_{b2})}{1 - P_u^2 s_{b2} s_{f3}} \left[\frac{1 + s_{f3}}{1 + s_{f2}} \right] \\
 R_4 &= \frac{P_u^2 s_{b2} - s_{b3}}{1 - P_u^2 s_{b2} s_{f3}} \left[\frac{1 + s_{f3}}{1 + s_{b3}} \right] & T_4 &= \frac{P_u (1 - s_{f3} s_{b3})}{1 - P_u^2 s_{b2} s_{f3}} \left[\frac{1 + s_{b2}}{1 + s_{b3}} \right]
 \end{aligned} \tag{B.1}$$

where

$$\begin{aligned}
 P_u &= \exp(g_2 - j\beta_2)L_2 \quad \text{and} \quad r = \frac{K_B - k_0}{K_B + k_0} \\
 P_1 &= D_f = \left[\frac{1 + s_{f2}}{1 + s_{f1}} \right] e^{\Gamma L_1} & P_2 &= D_b = \left[\frac{1 + s_{b1}}{1 + s_{b2}} \right] e^{\Gamma L_1} \\
 P_3 &= \left[\frac{1 + s_{f4}}{1 + s_{f3}} \right] e^{\Gamma L_3} & P_4 &= \left[\frac{1 + s_{b3}}{1 + s_{b4}} \right] e^{\Gamma L_3}
 \end{aligned} \tag{B.2}$$

The coefficients s_f and s_b are defined in (34). The numerical index indicates at which position z_i they are computed (and $k_0 = 2\pi/\lambda$).

For the reflectivity calculation (44), we have (fig. 11):

$$R_5 = -s_{f4} \left[\frac{1 + s_{b4}}{1 + s_{f4}} \right] \quad T_5 = (1 - s_{f4} s_{b4}) \left[\frac{1}{1 + s_{f4}} \right] \tag{B.3}$$

Notice that for the emission spectrum calculation, L_3 is different from the L_3 in the reflectivity calculation. For the spectrum (46)-(51), we get (fig. 16):

$$R_5 = R_6 + \frac{T_6 T_7 P_5 P_6 R_8}{1 - R_7 R_8 P_5 P_6} \quad (B.4)$$

where R_5 is an effective reflection coefficient, for everything to the left of the L_3/L_4 interface in figure 16. And we use (with $L_4 = z'_5 - z'_4$):

$$\begin{aligned} R_6 &= \frac{s_{f4}^u - s_{f4}}{1 - s_{f4}^u s_{b4}} \left[\frac{1 + s_{b4}}{1 + s_{f4}} \right] & T_6 &= \frac{1 - s_{f4} s_{b4}}{1 - s_{f4}^u s_{b4}} \left[\frac{1 + s_{f4}^u}{1 + s_{f4}} \right] \\ R_7 &= \frac{s_{b4} - s_{b4}^u}{1 - s_{f4}^u s_{b4}} \left[\frac{1 + s_{f4}^u}{1 + s_{b4}^u} \right] & T_7 &= \frac{1 - s_{f4}^u s_{b4}^u}{1 - s_{f4}^u s_{b4}} \left[\frac{1 + s_{b4}}{1 + s_{b4}^u} \right] \\ R_8 &= -s_{f5}^u \left[\frac{1 + s_{b5}^u}{1 + s_{f5}^u} \right] & P_5 &= \left[\frac{1 + s_{f5}^u}{1 + s_{f4}^u} \right] e^{\Gamma_5 L_4} & P_6 &= \left[\frac{1 + s_{b4}^u}{1 + s_{b5}^u} \right] e^{\Gamma_6 L_4} \end{aligned} \quad (B.5)$$

The superscript u for s indicates here that it is the s of the unpumped section (L_4) that has to be used.

References

- [1] C. Elachi, *"Waves in active and passive periodic structures: A review"*, Proc. of the IEEE, vol 64 (12), pp 1656-1698 (1976).
- [2] M. Ogura *et al*, *"Surface emitting laser diode with vertical GaAs/GaAlAs quarter-wavelength multilayers and lateral buried heterostructure"*, Appl. Phys. Lett., 51(21), pp 1655-1657, 23 November 1987.
- [3] Wei Hsin *et al*, *"GaAs/GaAlAs surface emitting laser diode with vertical distributed feedback cavity and transverse junction buried heterostructure"*, IEDM 1987 Technical Digest, paper 34.3, Washington DC (1987).
- [4] F. Koyama, K. Tomomatsu and K. Iga, *"GaAs surface emitting lasers with circular buried heterostructure grown by metalorganic chemical vapor deposition and two-dimensional laser array"*, Appl. Phys. Lett., 52(7), pp 528-531, 15 February 1988. See also the references therein.
- [5] S. Wang, *"Principles of distributed feedback and distributed Bragg-reflector lasers"*, IEEE J. Quantum Elec., QE-10 (4), pp 413-427 (1974).
- [6] S. Wang, *"Integratable active and passive optical devices"*, in: Semicond. and Semimetals, vol 22, part E (W.T.Tsang editor), 1985, see pp 52-64
- [7] A. Yariv, *"Quantum Electronics (2nd Edition)"*, Wiley, New York, 1975.
- [8] S. Wang, *"Thin-film Bragg lasers for integrated optics"*, Wave Electronics, vol 1, pp 31-59 (1974-1975).
- [9] A. Yariv and A. Grover, *"Equivalence of the coupled-mode and Floquet-Bloch formalism in periodic optical waveguides"*, Appl. Phys. Lett., vol 26, pp 537-539 (1975).
- [10] H. Soda and H. Imai, *"Analysis of the Spectrum Behavior Below the Threshold in DFB Lasers"*, IEEE J. Quantum Elec., QE-22 (5), pp 637-641 (1986).

- [11] L. Brillouin, "*Wave propagation in periodic structures*", Mc Graw-Hill, New-York, 1946.
- [12] Jean-Pierre Weber, unpublished.
- [13] G. Björk and O. Nilsson, "*A new exact and efficient numerical matrix theory of complicated laser structures: Properties of asymmetric phase-shifted DFB lasers*", J. Lightwave Techn., LT-5 (1), pp 140-146, January 1987.
- [14] A. Yariv and P. Yeh, "*Optical waves in crystals*", Wiley, New York, 1984.
- [15] H.C. Casey and M.B. Panish, "*Heterostructure Lasers*", Part A, Academic, New York (1978).
- [16] H.A. Haus, "*Waves and fields in optoelectronics*", Prentice-Hall, Englewood Cliffs, N.J., 1984.
- [17] Jean-Pierre Weber, unpublished.

Figure captions

Figure 1: Examples of periodic structure that give a one-dimensional wave equation: (a) waveguides, (b) multilayers.

Figure 2: Definition of the parameters for the two-layers structure.

Figure 3: Intensity gain in GaAs, as a function of free space wavelength for three different carrier densities: (1) $N=0.2 \times 10^{18} \text{ cm}^{-3}$, (2) $N=1.0 \times 10^{18} \text{ cm}^{-3}$, (3) $N=2.0 \times 10^{18} \text{ cm}^{-3}$.

Figure 4: G and δ_{eff} for the structure of table 1: (a) without gain or loss, (b) with 2000 cm^{-1} average gain, but neglecting gain periodicity, (c) as in b, but with gain periodicity (see text).

Figure 5: G and δ_{eff} for the structure of table 1 and the intensity gains of figure 3, corresponding to three different carrier densities: (a) $N=0.2 \times 10^{18} \text{ cm}^{-3}$, (b) $N=1.0 \times 10^{18} \text{ cm}^{-3}$, (c) $N=2.0 \times 10^{18} \text{ cm}^{-3}$.

Figure 6: $|s|$ as a function of wavelength for the two solutions of eq. (13), at three different carrier densities (Fig. 3): (a) $N=0.2 \times 10^{18} \text{ cm}^{-3}$, (b) $N=1.0 \times 10^{18} \text{ cm}^{-3}$, (c) $N=2.0 \times 10^{18} \text{ cm}^{-3}$.

Figure 7: $\text{Re}(s)$ and $\text{Im}(s)$ as functions of wavelength, at three different carrier densities (Fig. 3): (a) $N=0.2 \times 10^{18} \text{ cm}^{-3}$, (b) $N=1.0 \times 10^{18} \text{ cm}^{-3}$, (c) $N=2.0 \times 10^{18} \text{ cm}^{-3}$.

Figure 8: Definition of the transmission and reflection coefficients at a periodic/uniform regions interface (equation (39)).

Figure 9: Definition of the transmission and reflection coefficients at a phase shifter (equation (43)).

Figure 10: Model used for reflectivity and emission spectrum calculations. One pair consists of a quarter-wavelength layer of GaAs and a quarter-wavelength layer of GaAlAs. Dimensions are given in Table 1.

Figure 11: Definition of the coefficients for the reflectivity calculation (44).

Figure 12: (a) Result of the reflectivity calculation, with a center wavelength of $\lambda_0 = 893$ nm. (b) Comparison of experiment with best theoretical result (see text).

Figure 13: (a) Structure of the surface-emitting laser diode (SELD). (b) Scanning electron microscope picture of a SELD.

Figure 14: L-I characteristic of a SELD at room temperature, CW operation.

Figure 15: Emission spectrum of a SELD at different drive currents, room temperature, CW operation.

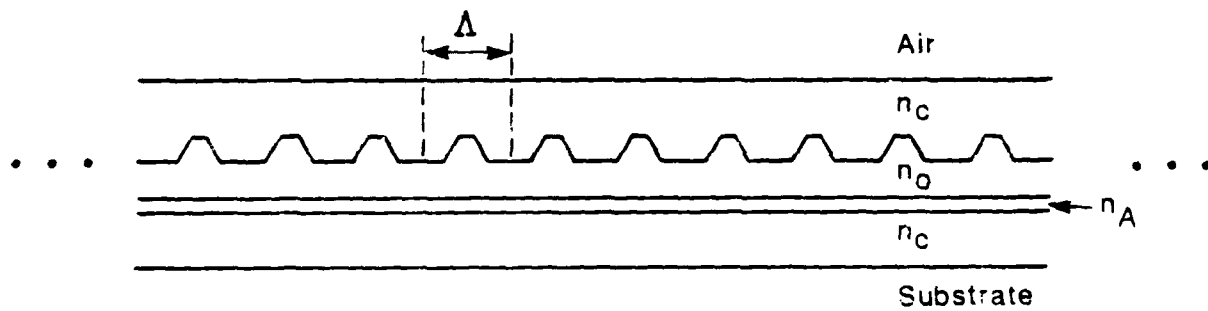
Figure 16: Definition of the coefficients for the emission spectrum calculation (equations (46-51)).

Figure 17: GaAs intensity gain curves ($N_A = 2 \times 10^{18} \text{ cm}^{-3}$): (a) at $T = 300\text{K}$, for several carrier densities, (b) at $N = 1.0 \times 10^{18} \text{ cm}^{-3}$ and several temperatures. These were obtained with the same model as for figure 3.

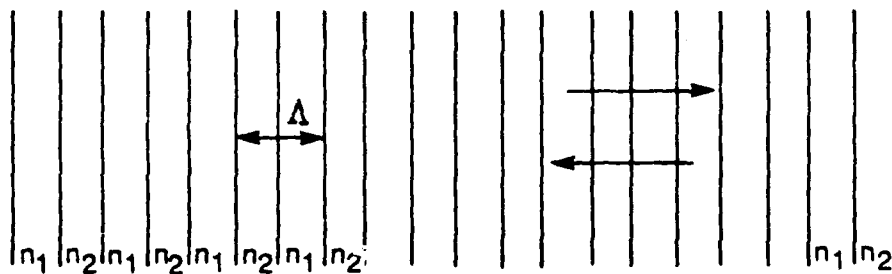
Figure 18: Emission spectrum for several carrier densities (currents) at 300K: (a) theory ($\lambda_0 = 890 \text{ nm}$, phase shifter thickness = $0.4 \text{ }\mu\text{m}$), (b) experiment (pulsed mode operation).

Figure 19: Emission spectrum for several temperature, at constant carrier density (current): (a) theory ($N = 1.0 \times 10^{18} \text{ cm}^{-3}$, same parameters as in figure 18), (b) experiment ($I = 320 \text{ mA}$, pulsed operation).

Table 1	
λ_0	890 nm
$n(\text{GaAs})=n_1$	3.59
$n(\text{Ga}_{0.7}\text{Al}_{0.3}\text{As})=n_2$	3.394
\bar{n} (average index)	3.494
z_1	62 nm
z_2	65.6 nm
Λ	127.6 nm
K_B	$2.467 \times 10^7 \text{ m}^{-1}$
$\kappa=\beta_1=\beta_{-1}$	$4.4 \times 10^5 \text{ m}^{-1}$
	Amplitude gains
g_1	1/2 of fig. 3 or 17
g_2	$- 500 \text{ m}^{-1}$



(a)



(b)

FIGURE 1

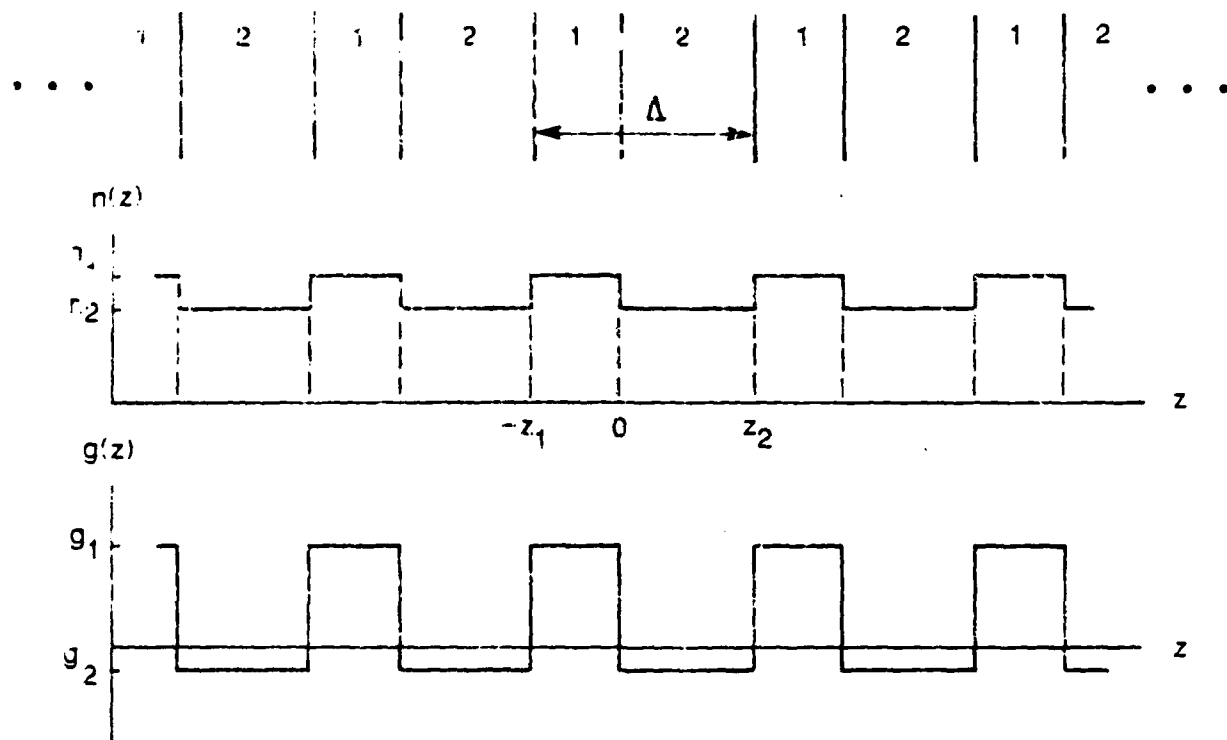


FIGURE 2

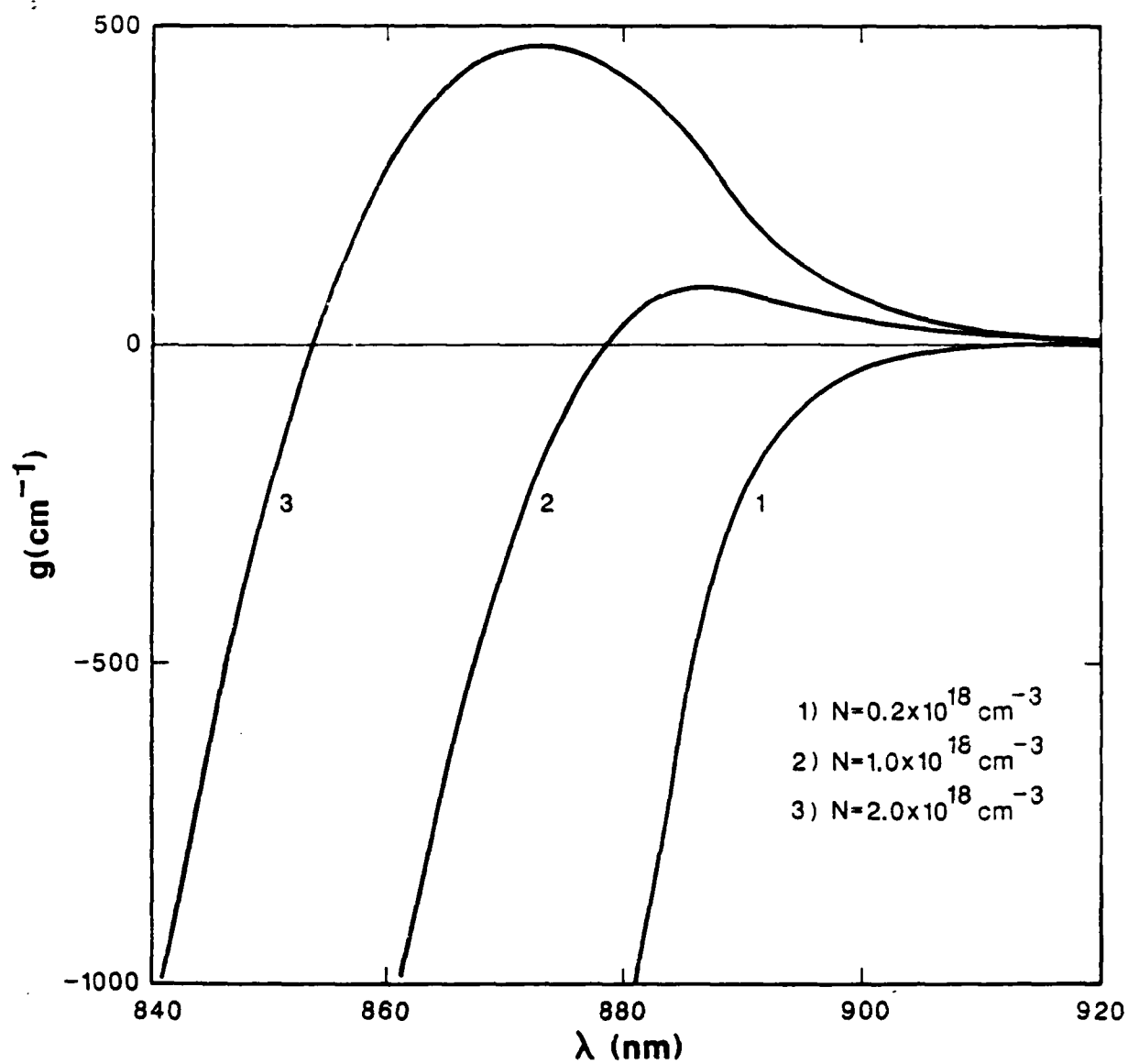
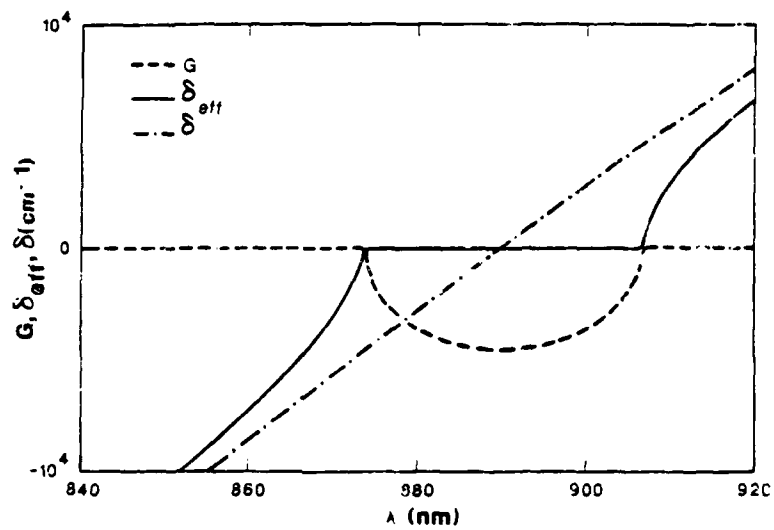
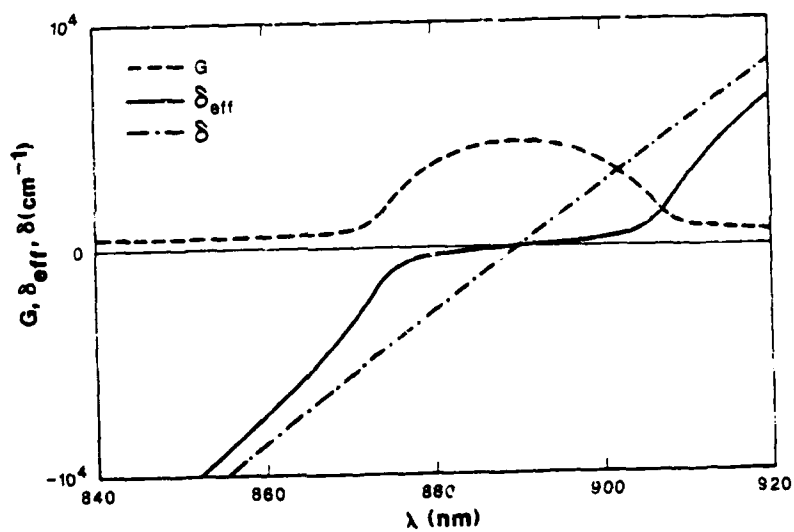


FIGURE 3

(a)



(b)



(c)

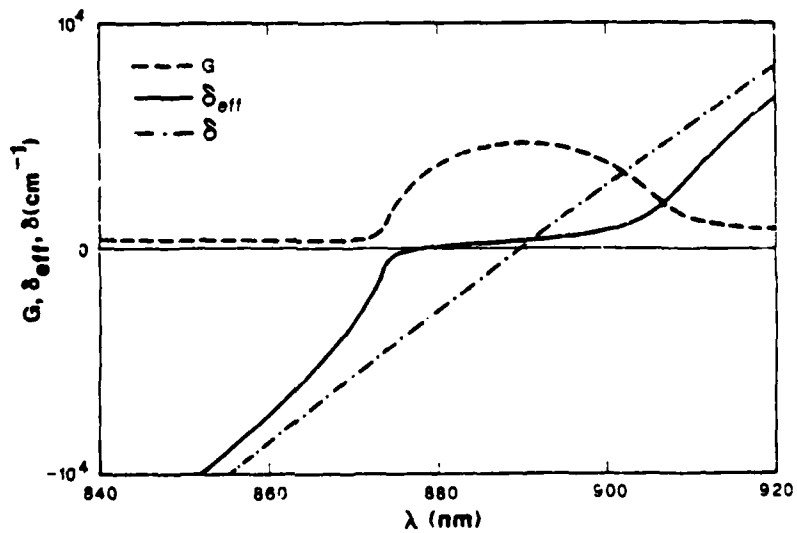
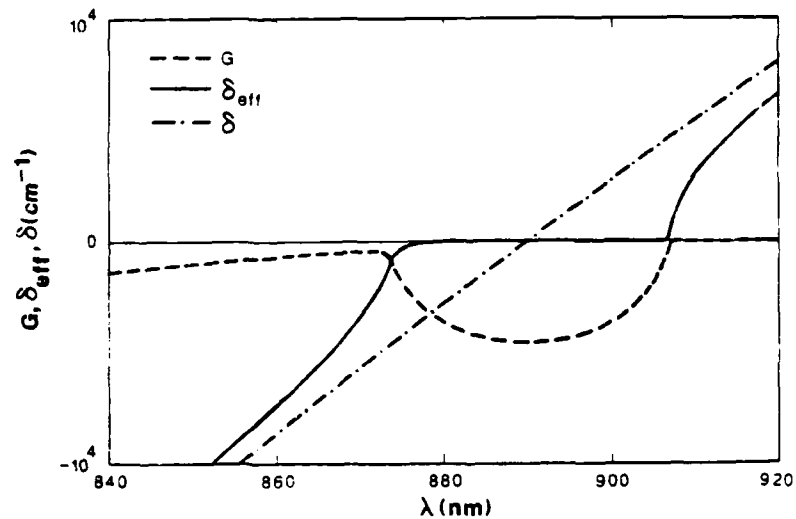
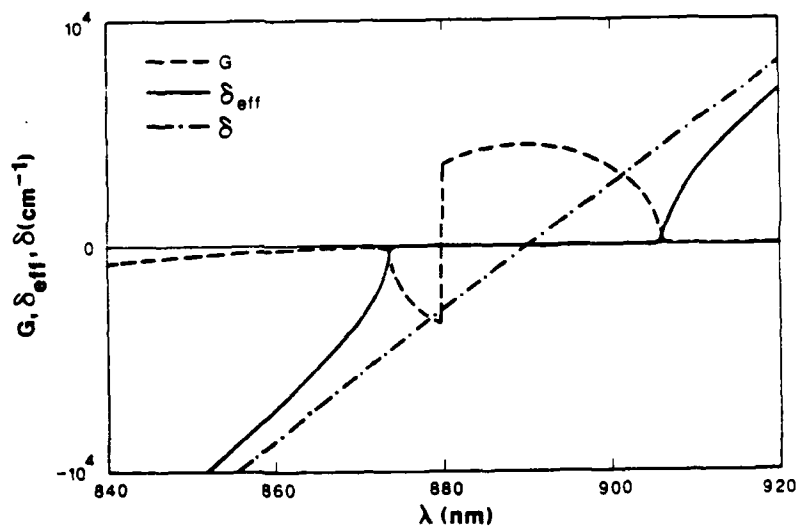


FIGURE 4

(a)



(b)



(c)

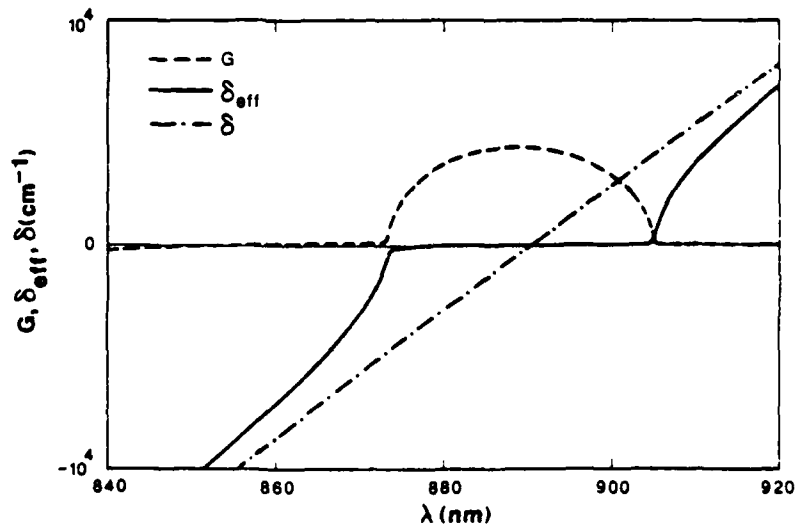
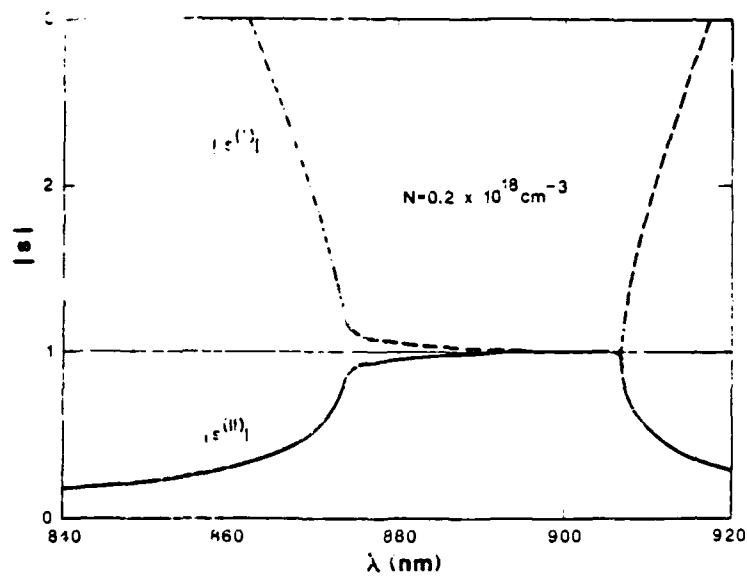
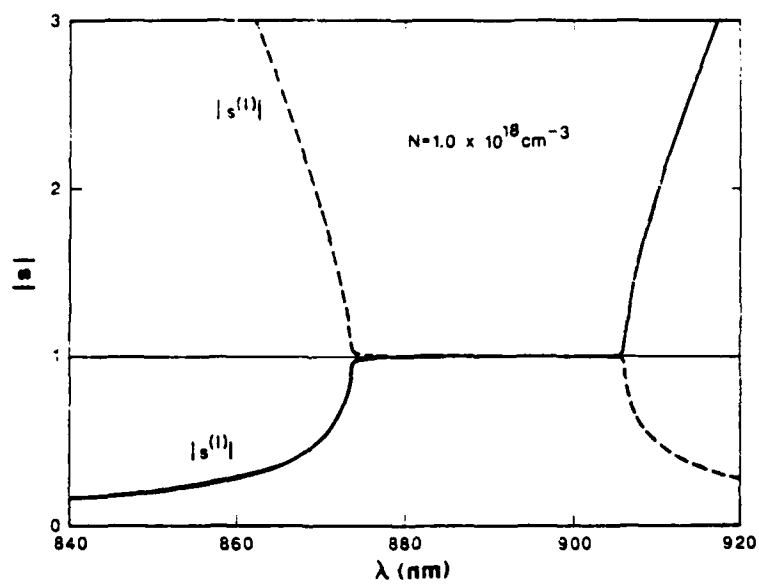


FIGURE 5

(a)



(b)



(c)

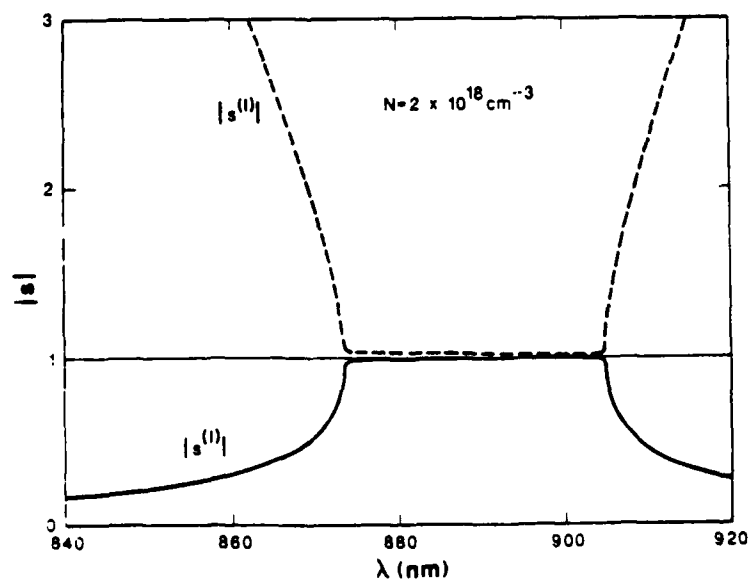
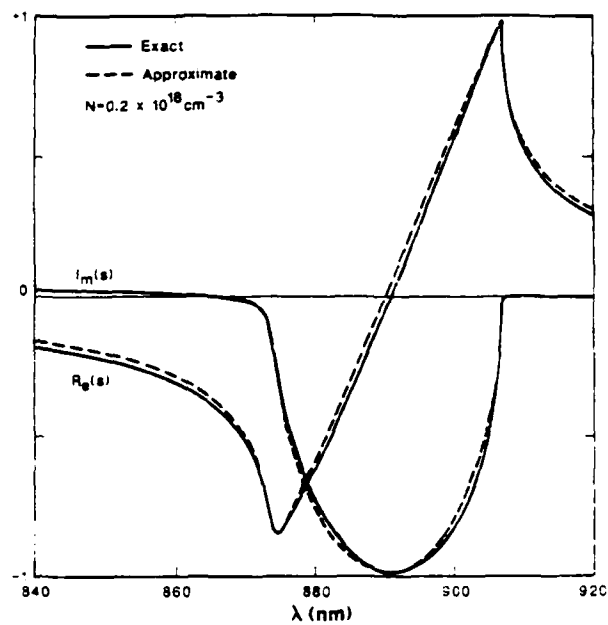
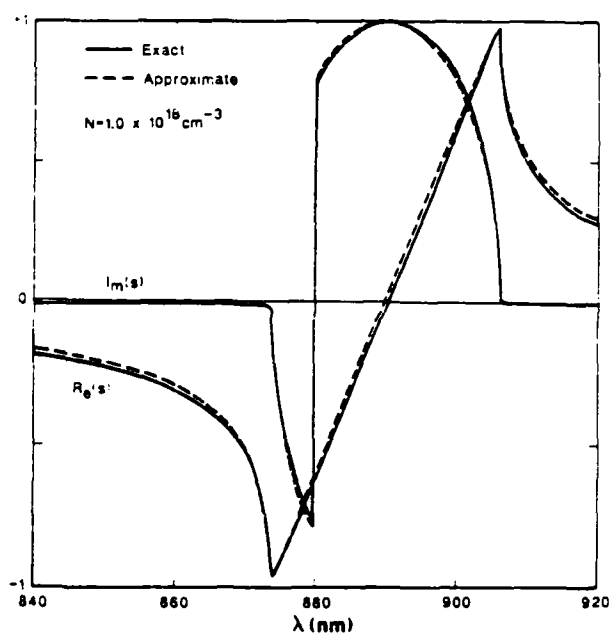


FIGURE 6

(a)



(b)



(c)

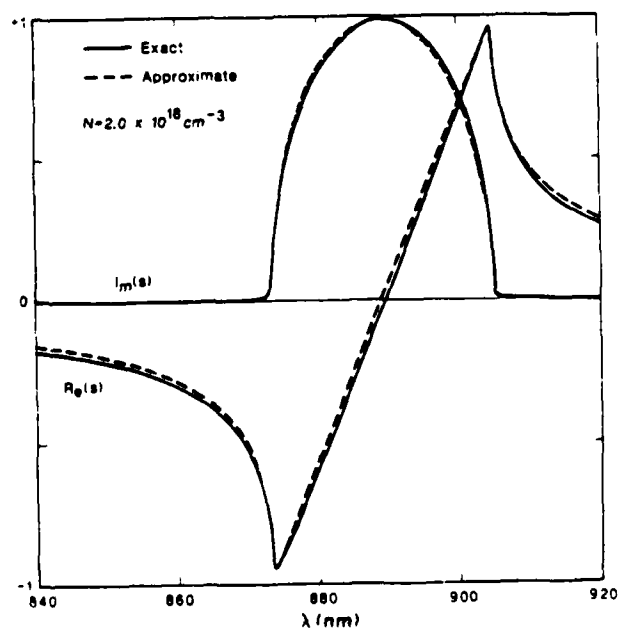


FIGURE 7

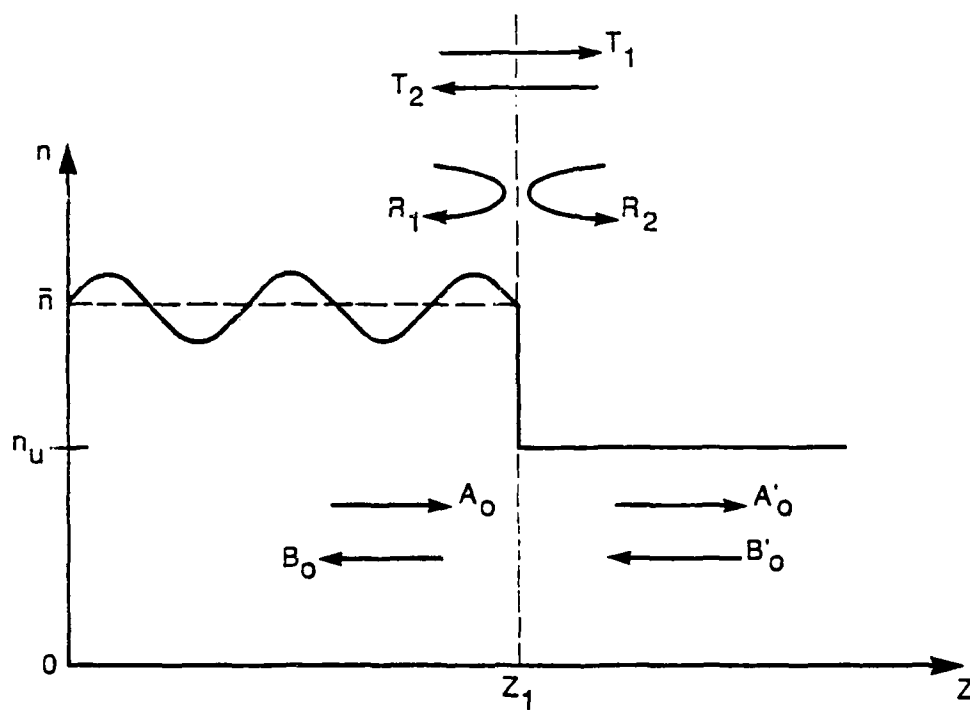


FIGURE 8

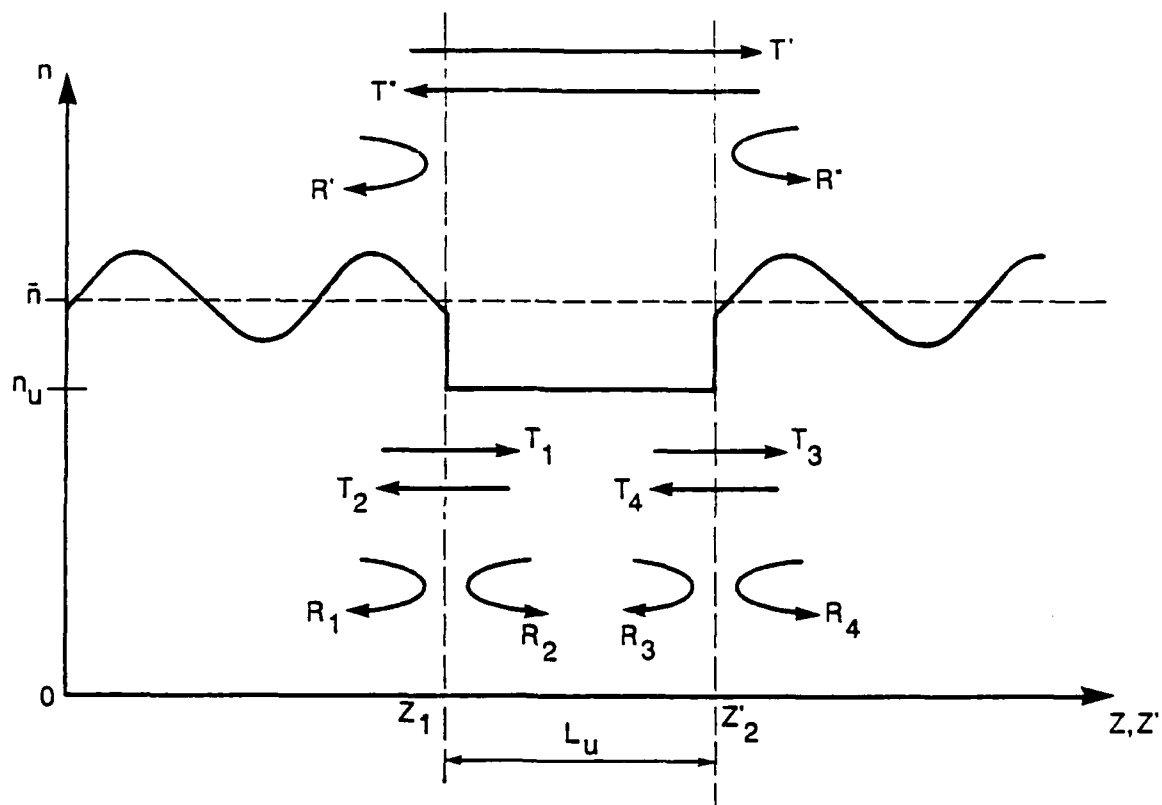


FIGURE 9

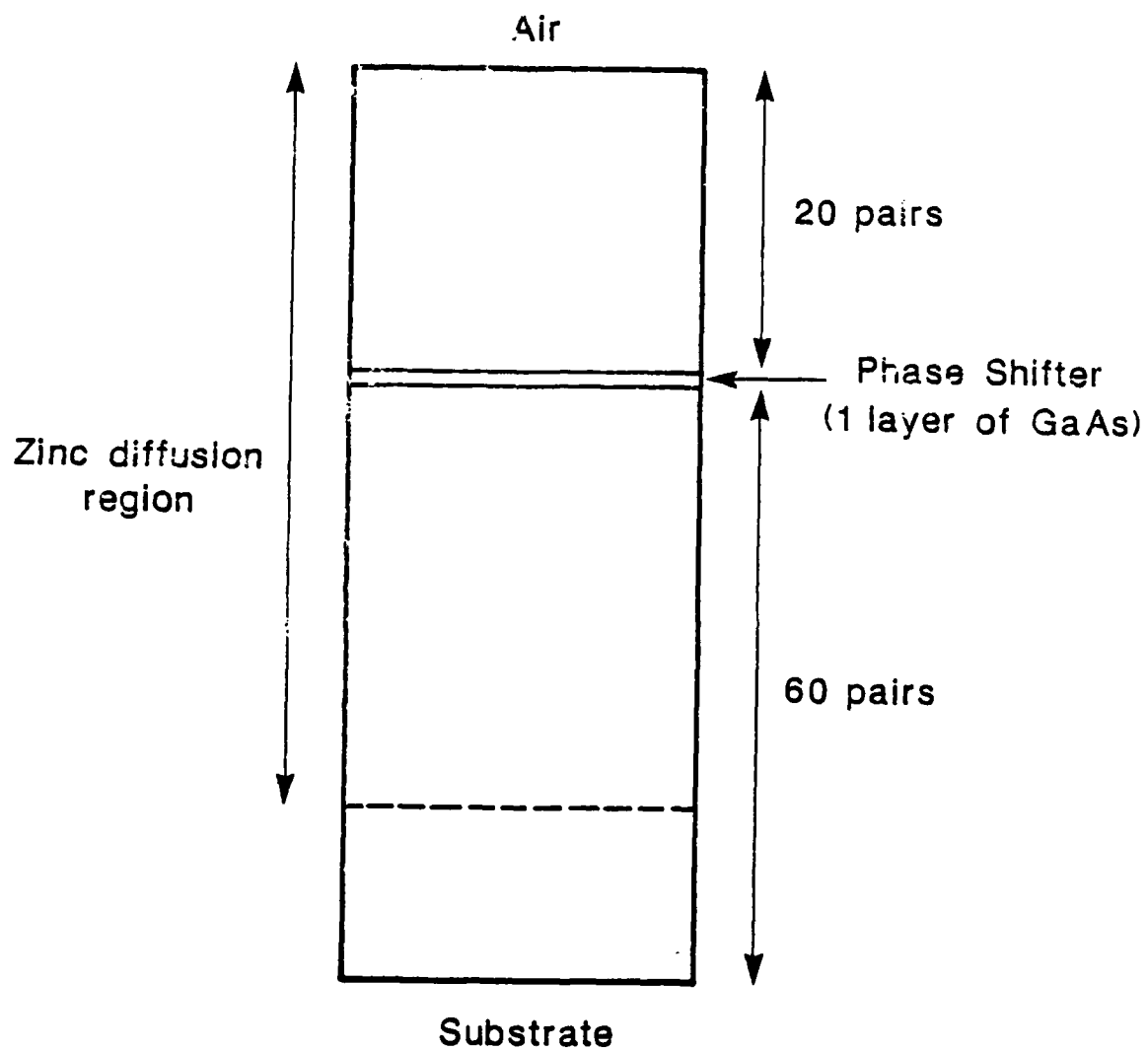


FIGURE 10

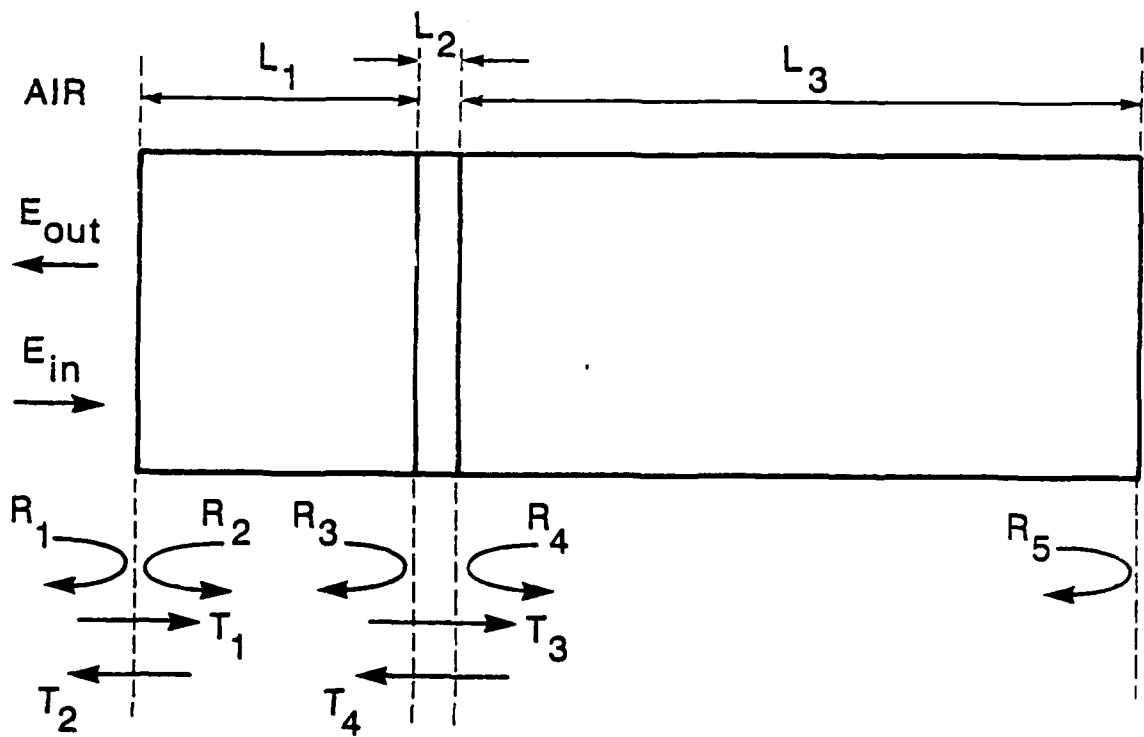


FIGURE 11

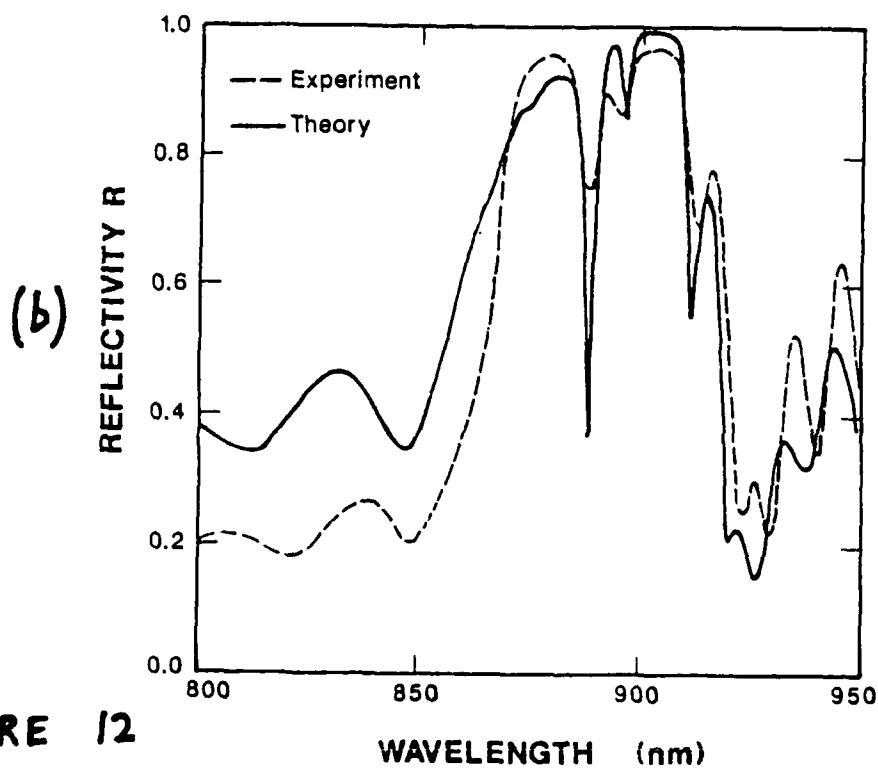
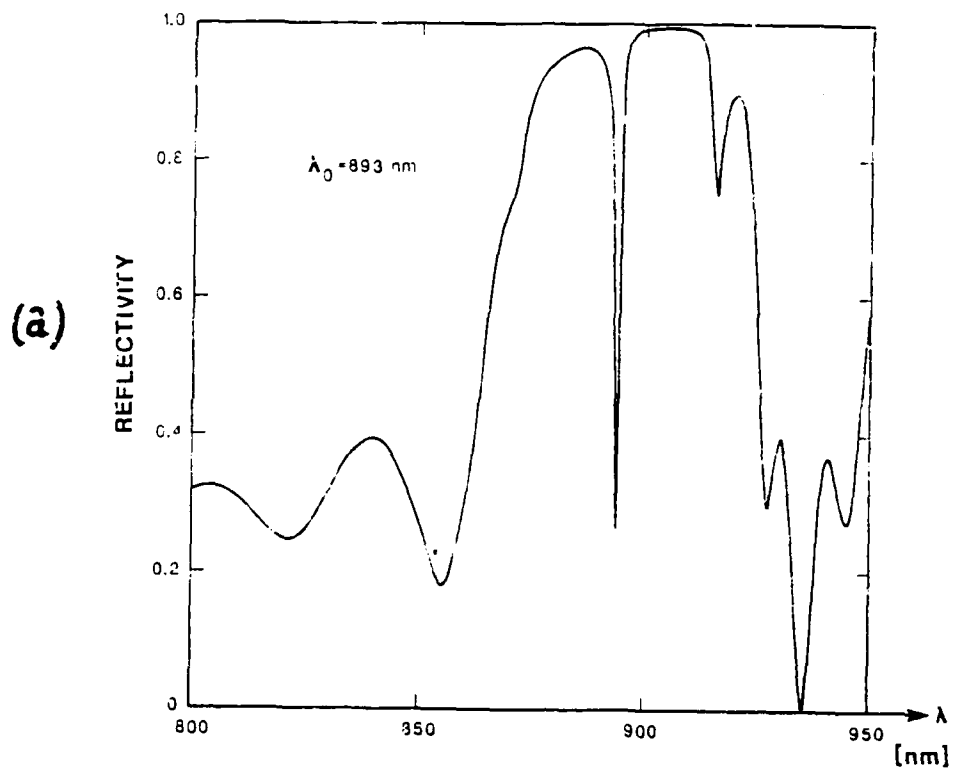


FIGURE 12

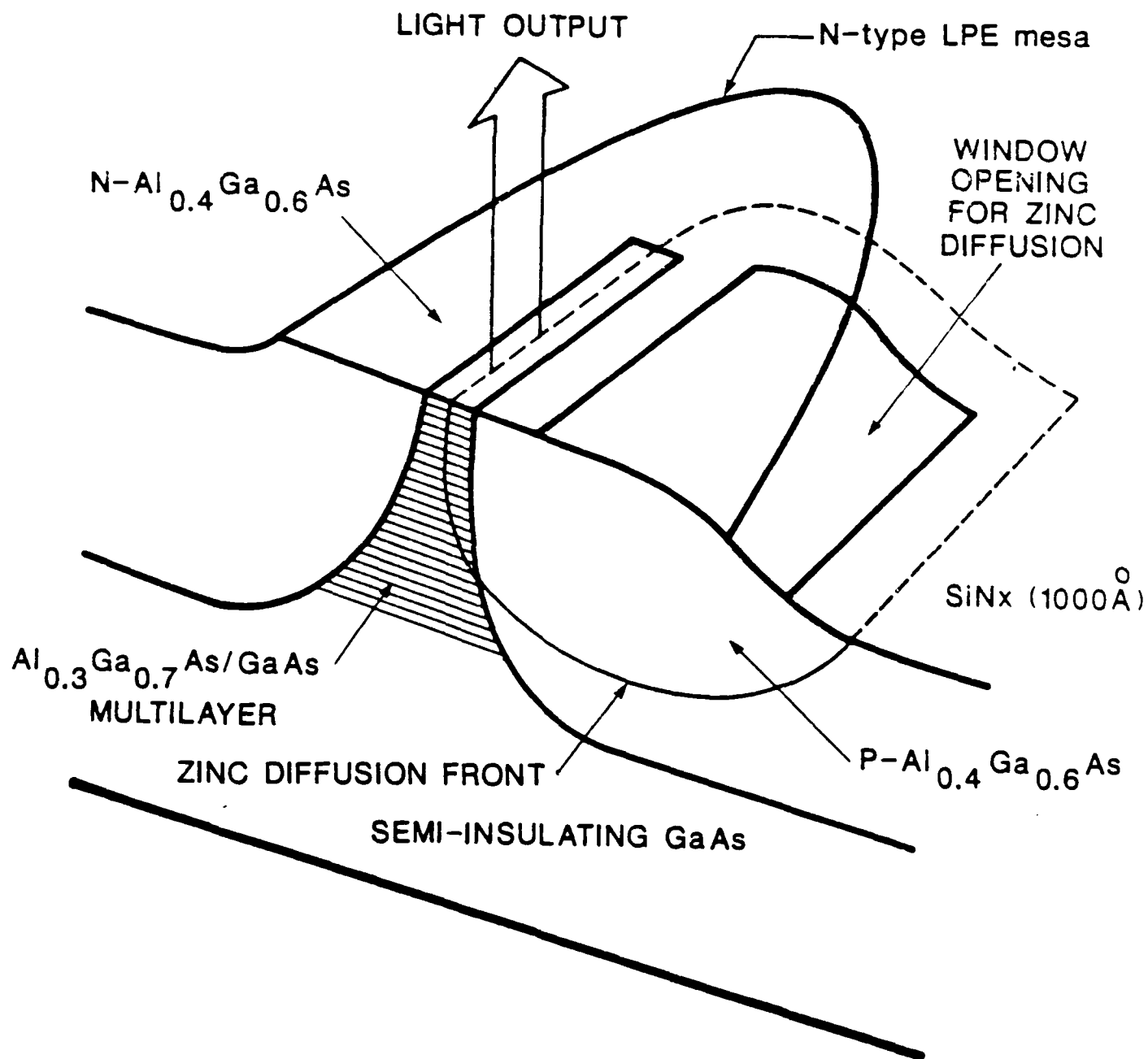


FIGURE 13 (a)

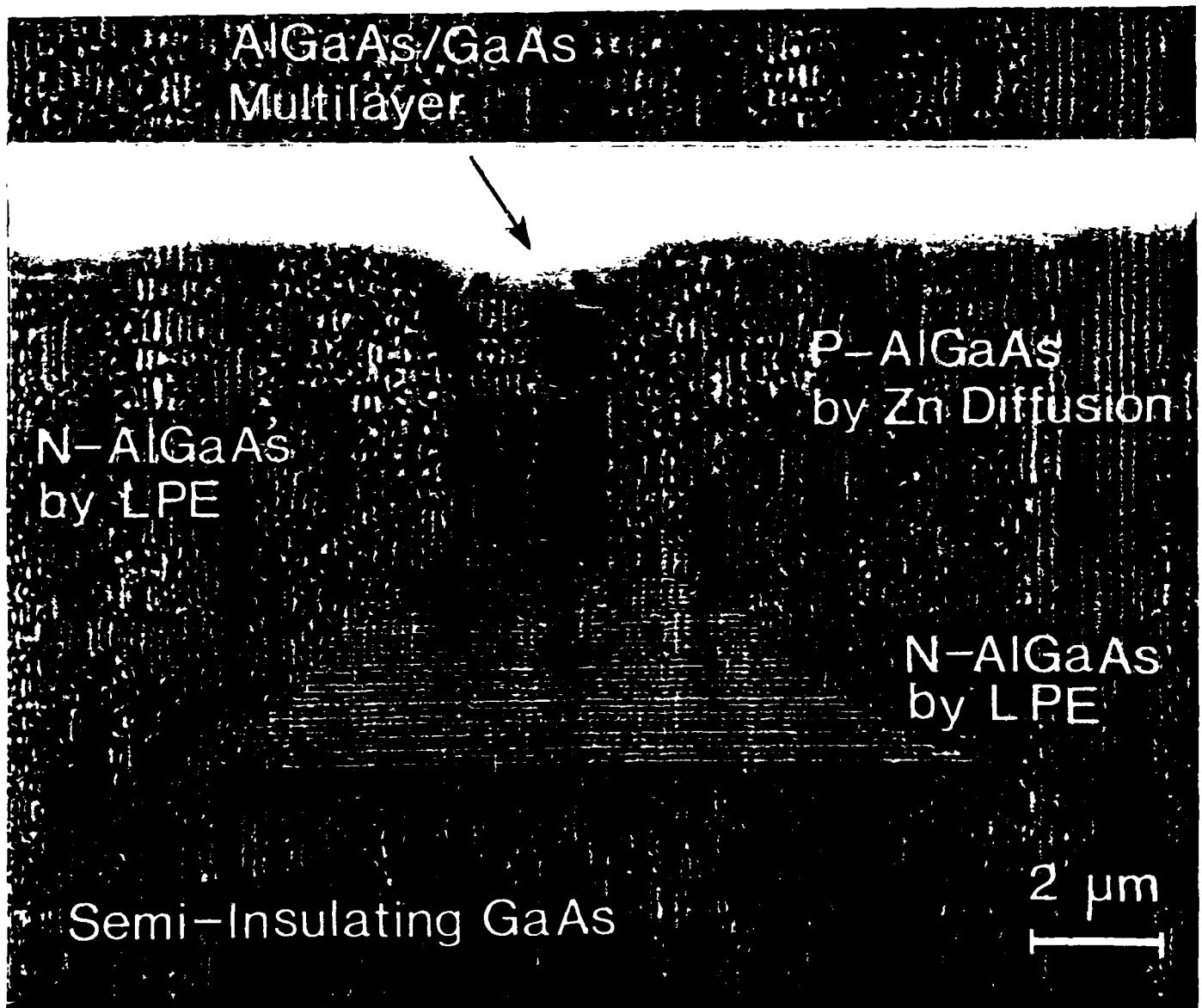


FIGURE 13 (b)

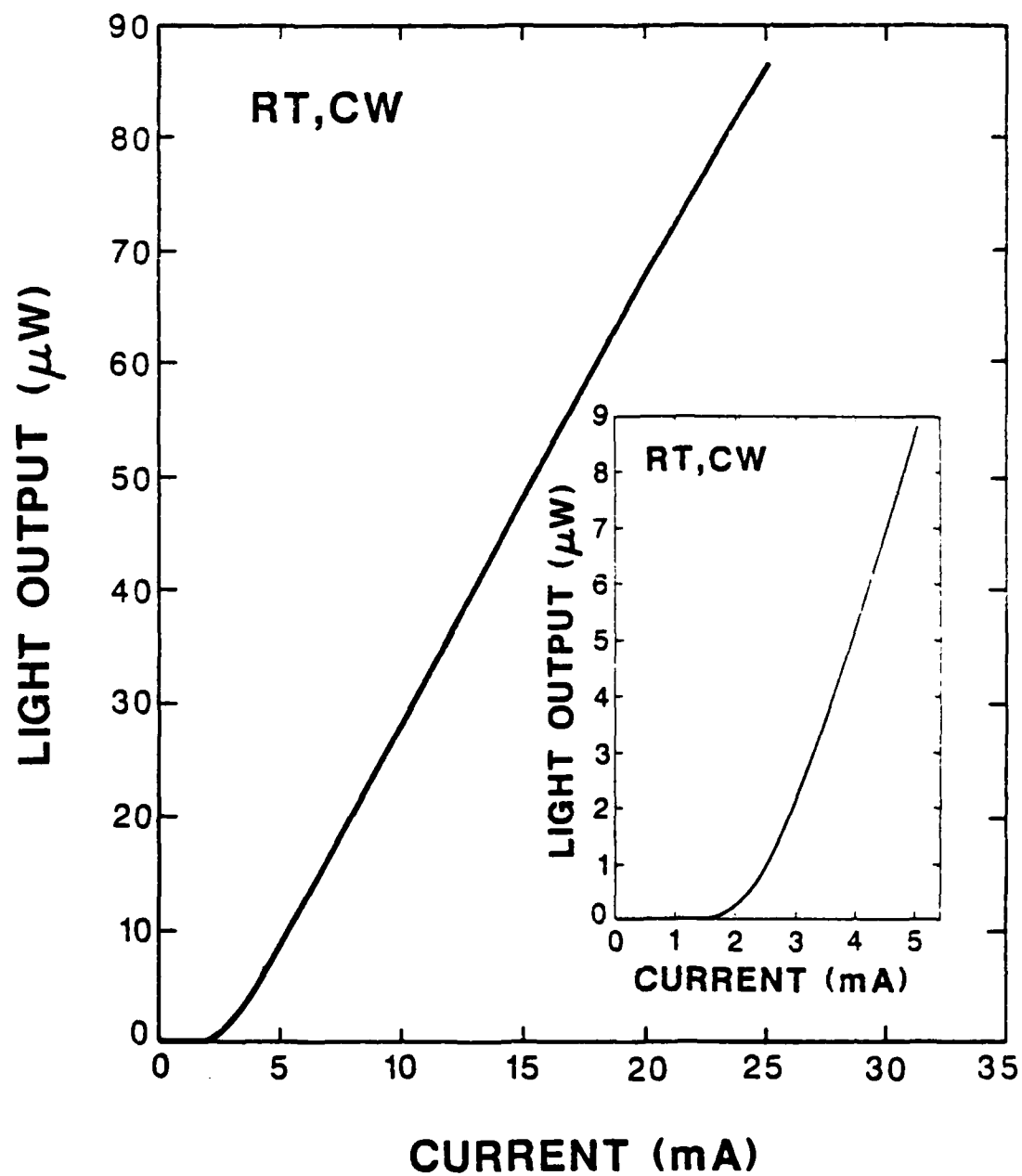


FIGURE 14

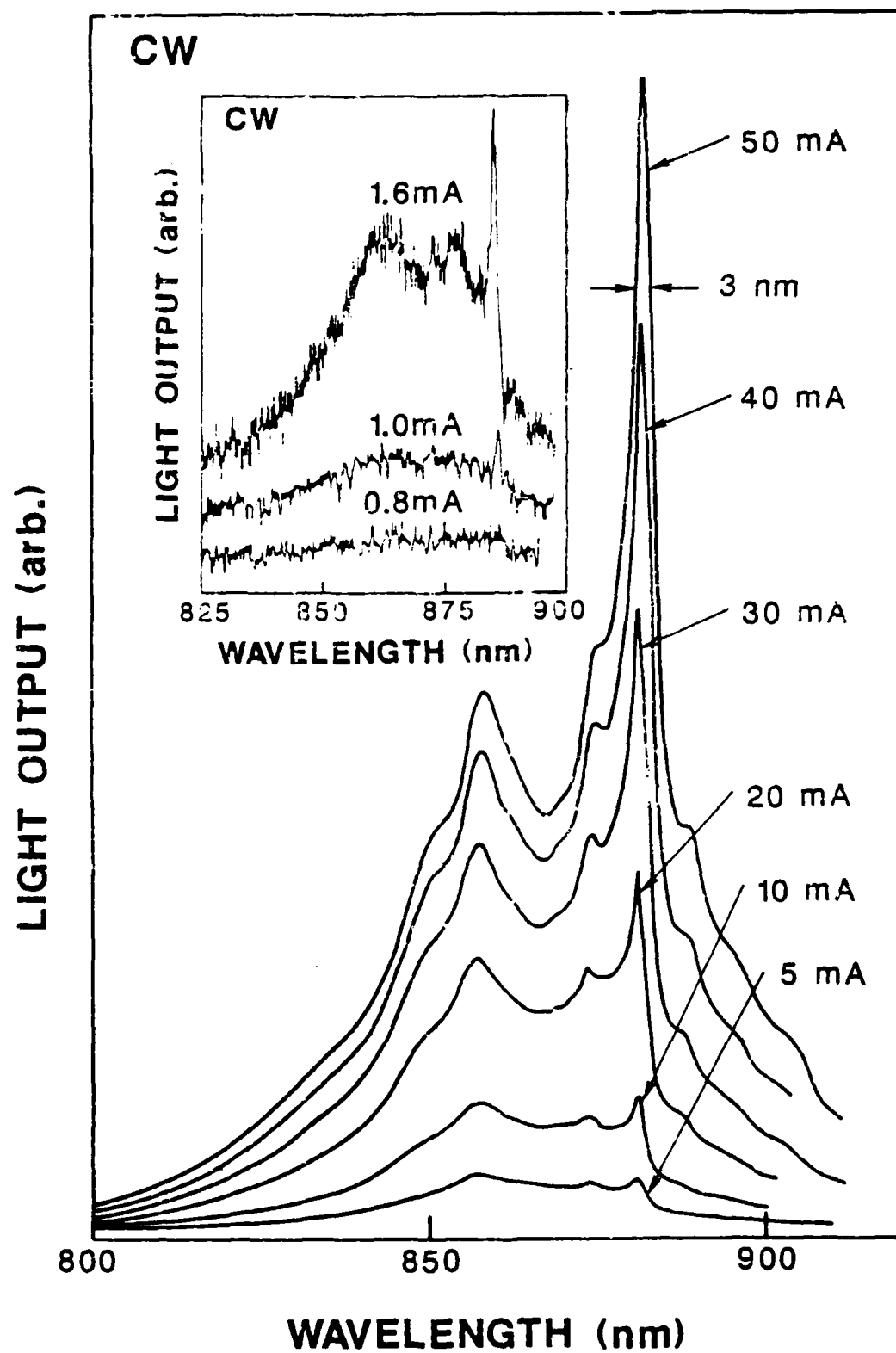


FIGURE 15

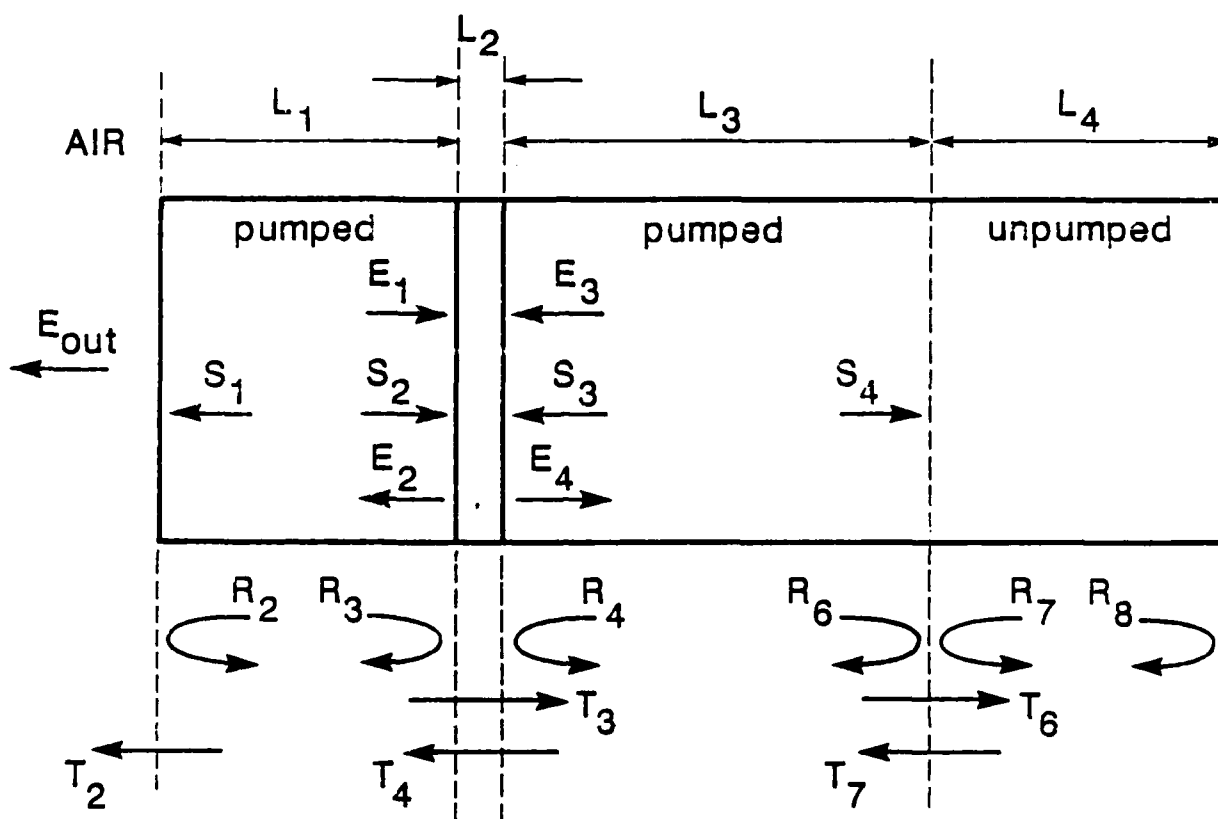


FIGURE 16

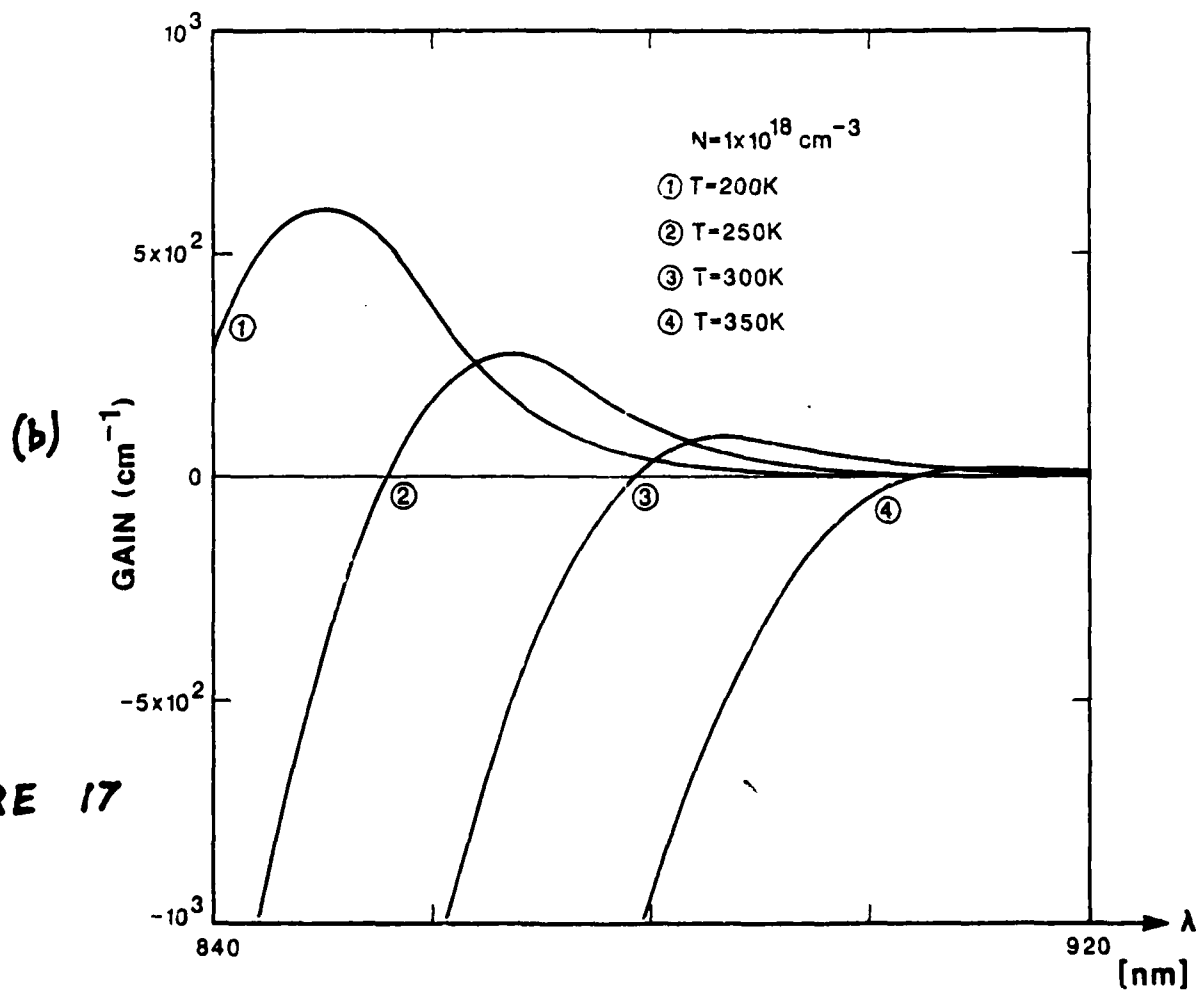
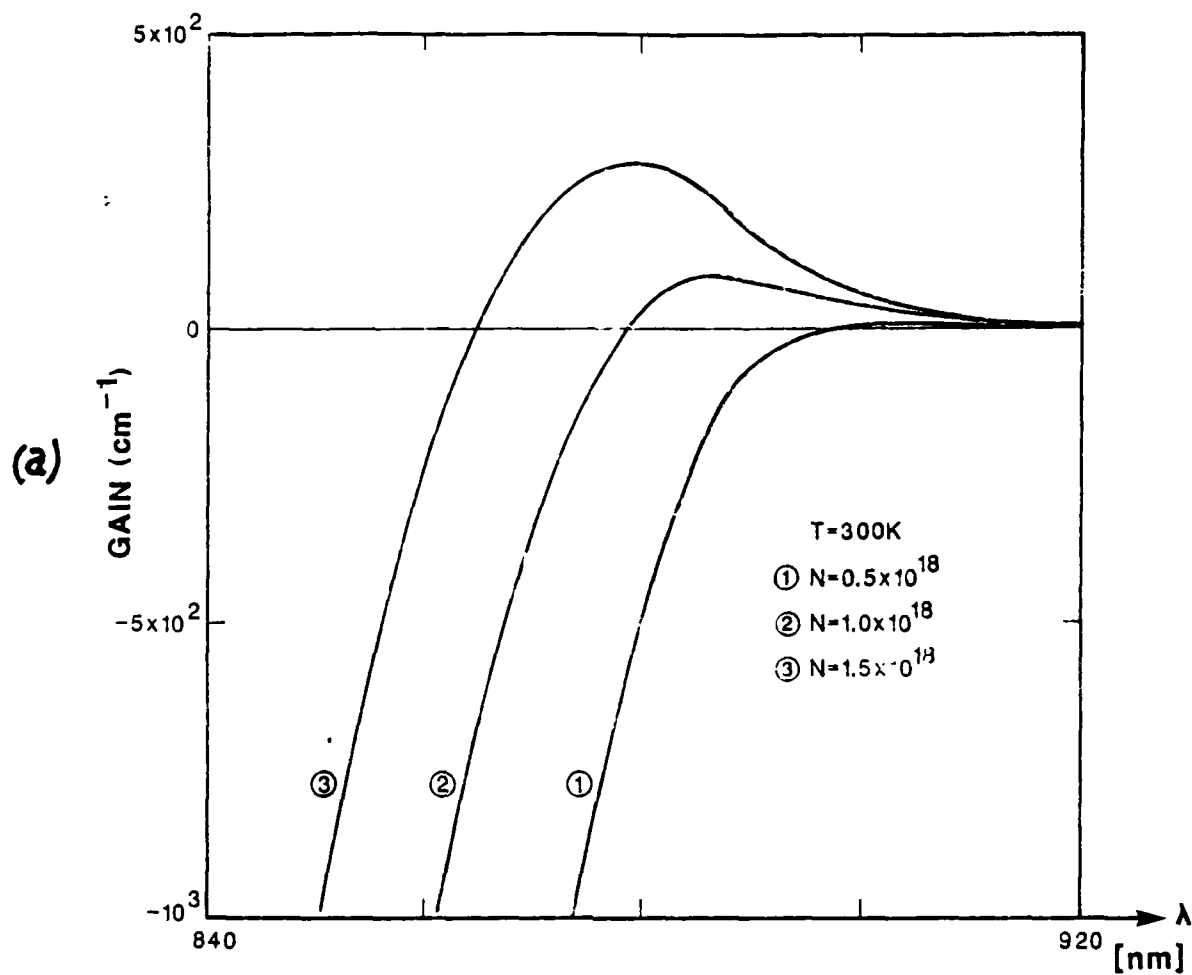


FIGURE 17

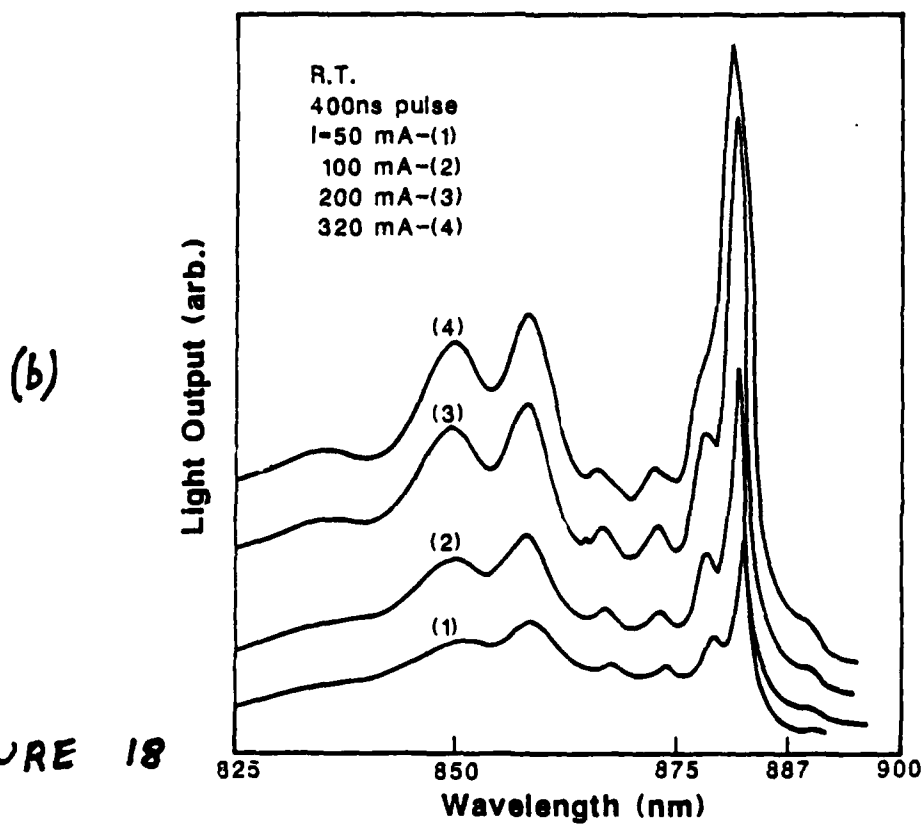
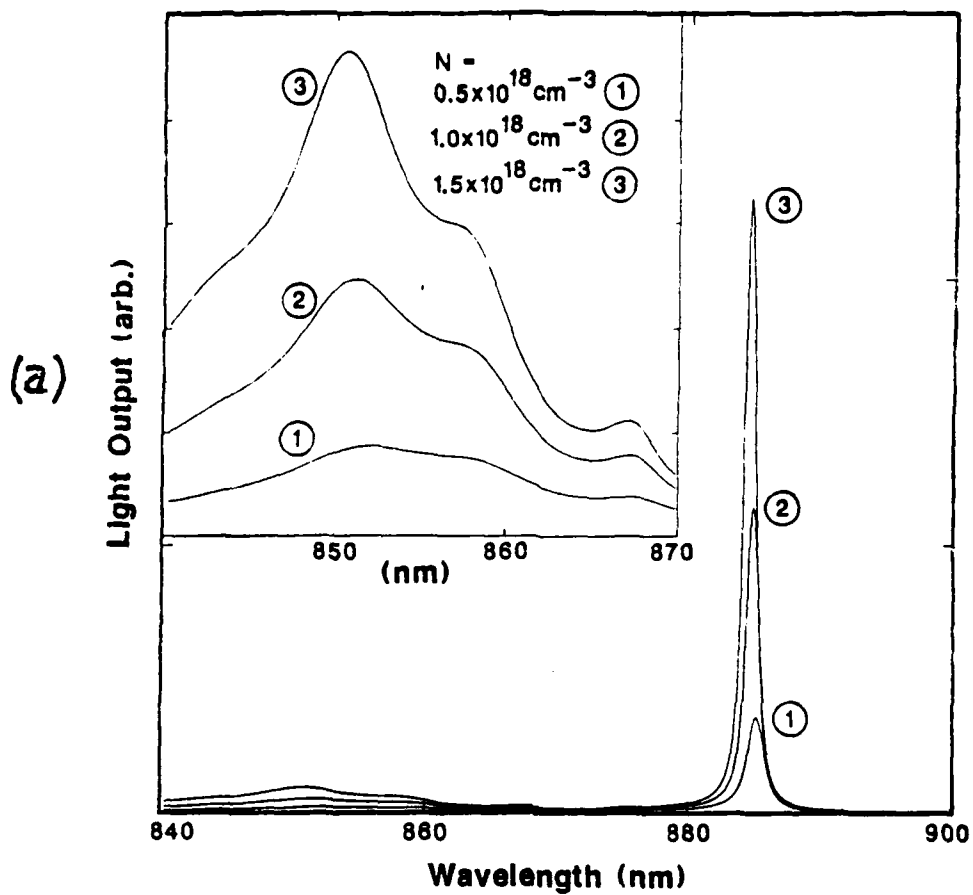
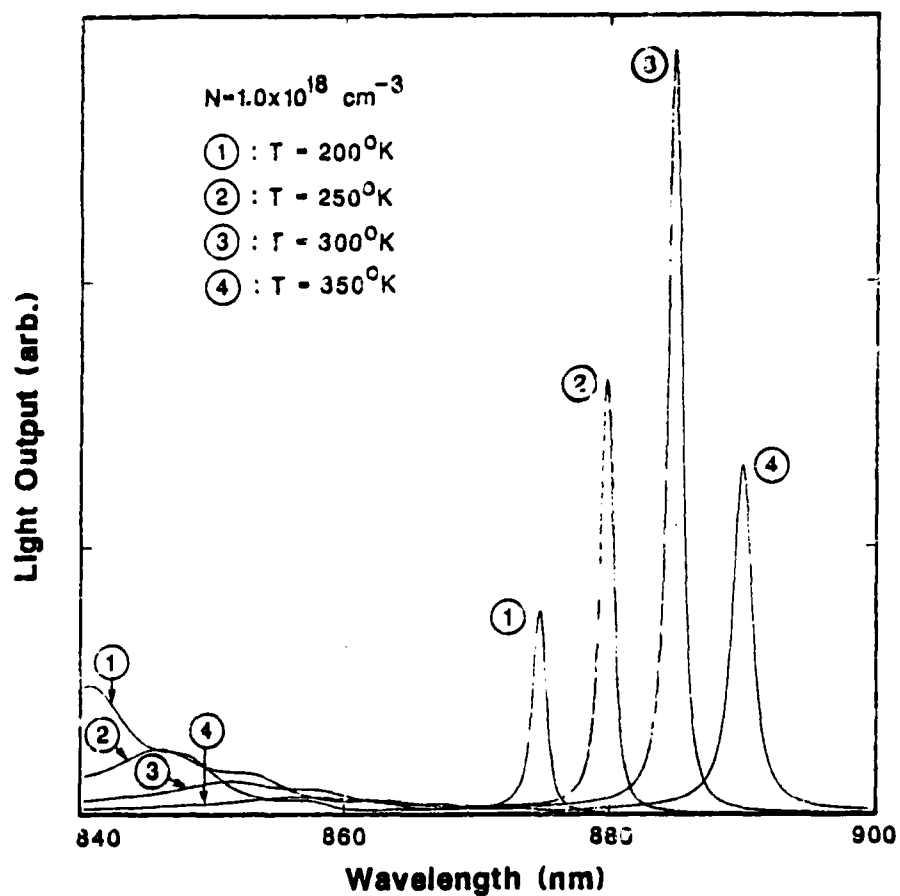


FIGURE 18

(a)



(b)

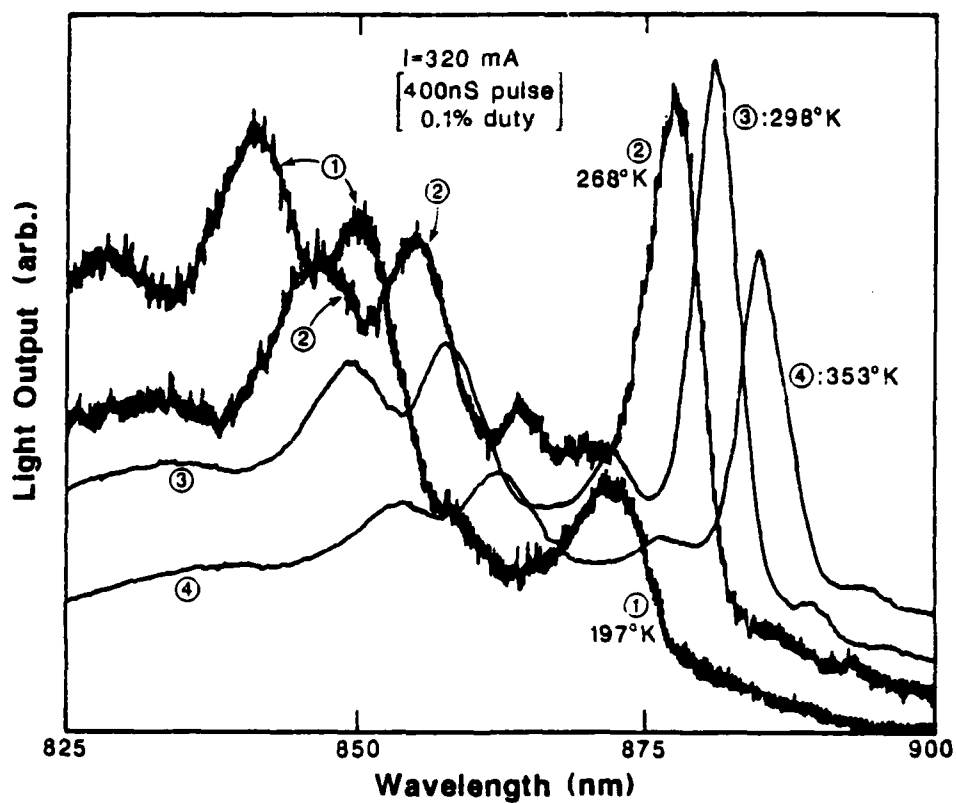


FIGURE 19

On The Emission Properties of Surface-Emitting DFB and DBR
Semiconductor Lasers

T.G. Dziura and S.C. Wang
Lockheed Palo Alto Research Laboratory
3251 Hanover Street
Palo Alto, CA 94304

We use a single mode transfer equation model to study the performance of vertical-cavity surface-emitting DFB and DBR semiconductor lasers above threshold. We find that DBR lasers exhibit less envelope spatial hole burning than both single and double phase-shifted DFB lasers and therefore may achieve more stable single longitudinal mode operation.

Surface-emitting semiconductor lasers are being developed for two dimensional array applications and may eventually be useful in optoelectronic integrated circuit technology. The designs can be distinguished according to whether the resonator feedback is in the plane of the wafer¹⁻⁴ or normal to it⁵⁻⁸; Fabry-Perot, distributed feedback (DFB), distributed Bragg reflector (DBR), and mixed Fabry-Perot-DBR-type devices have been demonstrated. The threshold current of these lasers must be minimized to reduce heating effects, total array power requirements, and the size of on-chip drive electronics, but a high output efficiency is also desirable. A model intended to determine the optimum structure should be capable of calculating the output characteristics above threshold. Several authors have used coupled mode theory to analyze DFB lasers in the above threshold regime. Hill and Watanabe⁹ constructed a numerical treatment and considered the problems caused by parasitic losses. Haus¹⁰ derived analytical formulas for the output power of overcoupled lasers, and Szczepanski¹¹ extended these results to the undercoupled case. These authors did not consider the effect of phase shift layers, and the effect of facet reflections was considered only in Ref. 11. Also these results are more appropriate to edge-emitting lasers; the coupled mode formalism assumes weak coupling between the counterpropagating waves, and surface emitting lasers nominally operate in the strong coupling regime. Typically the distributed feedback coefficient $K \sim 5000-10000 \text{ cm}^{-1}$ for surface emitters, and $K \sim 50 \text{ cm}^{-1}$ for edge emitters. In order to take this strong coupling effect into consideration and to include the effects of gain saturation, we have extended the discrete propagation techniques of Björk and Nilsson¹² and have applied this model to a comparison of vertical cavity surface-emitting

DFB and distributed Bragg reflector (DBR) lasers. We also analyze the performance of a structure we have recently developed⁷. The methods of Ref. 12 are particularly amenable to computer calculation and well suited to analyzing resonators having a multilayer structure. They are also flexible enough to be used in cases involving facet reflections, phase shift layers, amplifying regions, and dielectric coatings.

The type of laser we will consider employs a multilayer heterostructure for distributed feedback and a buried heterostructure waveguide for optical mode confinement. Phase shift layers or amplifying layers may be placed anywhere along the resonator length. The equations we use to model such a laser comprise two sets. The first set treats the free propagation of the forward and backward waves within a layer according to

$$A_i(z_i + l_i) = A_i(z_i) \exp[i\beta_i l_i + (1/2) g_i(A_i, B_i) l_i] \quad (1)$$

$$B_i(z_i + l_i) = B_i(z_i) \exp[-i\beta_i l_i - (1/2) g_i(A_i, B_i) l_i] \quad (2)$$

$$g_i(A_i, B_i) = g_0 / (1 + |A_i(z_i)|^2 + |B_i(z_i)|^2) \quad (3)$$

where A_i and B_i are the normalized forward and backward wave amplitudes in the i -th layer, z_i is the axial position of layer i , β_i is the propagation constant, l_i is the i -th layer thickness, and g_i and g_0 are the saturated and unsaturated intensity gain coefficients respectively. In Eq. (3) we have assumed that carrier diffusion effectively eliminates any longitudinal spatial hole burning within a layer; we also ignore the transverse variation in the laser mode and homogeneously saturated gain.

The fields are propagated across an interface between layers i and j

using the equation set

$$A_j = F_{ij} \left[\frac{(\beta_i + \beta_j)}{2\beta_j} A_i + \frac{(\beta_i - \beta_j)}{2\beta_j} B_i \right] \quad (4)$$

$$B_j = F_{ij} \left[\frac{(\beta_j - \beta_i)}{2\beta_j} A_i + \frac{(\beta_i + \beta_j)}{2\beta_j} B_i \right] \quad (5)$$

$$F_{ij} = \left(\frac{\beta_j}{\beta_i} \right)^{(1/2)} \frac{H_{ij}}{(H_{ii}H_{jj})^{(1/2)}} \quad (6)$$

$$H_{ij} = \sum \int \int dx dy w_i w_j^* \quad (7)$$

where w_i is the waveguide mode field function in layer i , and the sum in Eq. (7) is over polarization. Eqs. (4-7) have been derived following results by Wang¹³. The overlap integrals in Eq. (6) account for the mismatch in mode profile between two layers. It is assumed that the power scattered into higher order waveguide modes is negligible; this is a good approximation for the surface emitting lasers demonstrated to date. In the case of an interface between a waveguiding region and a non-waveguiding region, we assume that to first order and for short propagation distances the transverse mode profile in the free space region is the same as that in the waveguide; we also use the plane wave propagation constant for the non-waveguide region. Eqs. (1-7) are used repetitively to calculate the field amplitude in all layers; the boundary conditions are satisfied only for a particular set of values of g_0 , λ , B_1 , and A_{n+2} (n is the number of layers). We use a quasi-Newton optimization routine to efficiently calculate the solution for each value of the output power¹⁴.

We show in Fig. 1 the forward and backward output power versus

pumping calculated for the lowest order longitudinal mode (at 882.6 nm) of the structure of Ref. 7. The resonator consists of 80 pairs of $\text{Al}_{0.3}\text{Ga}_{0.7}\text{As}/\text{GaAs}$ tuned to 883 nm. The quarter-wave phase shift layer is used to ensure oscillation at the Bragg mode; its placement 20 pairs from the output facet effectively diverts most of the power in that direction. The slight superlinearity in the output curve can be explained by examining the axial distribution of the intensity, plotted in Fig. 2a, at a pumping twice the threshold pumping. It is seen that the intensity is maximized at the phase shift layer, and the gain is saturated only in the front portion of the resonator. This mode will not tend to oscillate coherently since spontaneous emission processes dominate in the back portion of the resonator. In fact the gain there is available for extraction by the next mode with shorter wavelength (at 860.8 nm), since its intensity is maximized in that section of the structure (Fig. 2b). For this laser the threshold gain of the mode at 860.8 nm is roughly four times that of the Bragg mode, and therefore its contribution to the output spectrum will likely be as a broad amplified spontaneous emission background. A similar effect was noted by Usami et al.¹⁵ in a study of edge-emitting lasers; the large coupling coefficients used here ($K \sim 5400 \text{ cm}^{-1}$, $KL \sim 5.4$) exacerbate this problem. The large oscillation linewidth and multimode spectrum observed in Ref. 7 may possibly be explained by these considerations.

It has been suggested recently¹⁶⁻¹⁸ that the use of multiple phase shift layers can help reduce the problems associated with spatial hole burning. We examine by way of example a distributed feedback design with 75 pairs of $\text{Al}_{0.9}\text{Ga}_{0.1}\text{As}/\text{GaAs}$ tuned to 839 nm, and with phase shift layers inserted at the 25-th and 55-th pairs from the back facet. Both

shifters are 0.425 waves in thickness, and the estimated KL for this structure is 12.5. These parameters were chosen to smooth the saturated gain distribution as well as force lasing near the GaAs spectral gain maximum. The axial intensity distribution for the first lasing mode at 875 nm is shown in Fig. 3a, again at twice the threshold. The intensity is a maximum at both phase shift layers, and the fraction of the resonator experiencing gain saturation and coherent emission is larger than in the single phase shifter design. The large detuning of the mode from the Bragg wavelength aids in smoothing the intensity distribution between the phase shift layers. Unfortunately this mode is still susceptible to gain competition from neighboring modes as is confirmed by examining the axial distribution of the higher threshold mode at 892 nm (Fig. 3b). This mode can extract the spatial gain that is unused by the main lasing mode.

Simple DBR lasers do not in general suffer from these problems. The boundary conditions imposed by the two endmirrors cause the axial intensity to be a maximum in the amplifying layer, leading to efficient gain conversion. This is illustrated in Fig. 4 for a representative DBR structure (for one endmirror $KL \sim 3.50$, for the other $KL \sim 1.66$; the amplifying layer is 2 μm thick). For the higher order longitudinal modes the increased detuning from the Bragg wavelength causes the intensity distribution to be a maximum in the DBR reflector and outside the amplifying layer, reducing the gain extraction and ensuring good mode discrimination. Mixed DBR-Fabry-Perot lasers have exhibited high mode selectivity and narrow linewidth^{5,8}, lending credence to these conclusions. Our theory can be used to model these lasers by assuming plane wave propagation in the dielectric mirror, as discussed above. A prediction of the oscillation linewidth of single mode emitters is outside the scope of our present

treatment, as it is determined in part by factors such as layer thickness fluctuations which we have not included.

In conclusion, we have applied discrete propagation methods to analyze the emission properties of DFB and DBR surface emitting lasers. For DFB lasers with either one or two phase shifting layers the mode discrimination can be rather poor due to competition for the spatially varying gain. Our results suggest that DBR lasers are less susceptible to these spatial hole burning effects.

This research was supported in part by the Office of Naval Research and the Air Force Rome Air Development Center.

References

1. N.W. Carlson, G.A. Evans, J.M. Hammer, M. Lurie, L.A. Carr, F.Z. Hawrylo, E.A. James, C.J. Kaiser, J.B. Kirk, W.F. Reichert, D.A. Truxal, J.R. Shealy, S.R. Chinn, and P.S. Zory, CLEO '88 (25-29 April 1988, Anaheim, CA), paper WO4.
2. Z.L. Liao, J.N. Walpole, and V. Diadiuk, IGWO '88 (28-30 March, 1988, Santa Fe, NM), paper WA1-1.
3. S. Noda, K. Kojima, K. Kyuma, J. Ohta, K. Hamanaka, and T. Nakayama, CLEO '88 (25-29 April 1988, Anaheim, CA), paper WO1.
4. S.H. Macomber, J.S. Mott, R.J. Noll, G.M. Gallatin, E.J. Gratrix, S.L. O'Dwyer, and S.A. Lambert, Appl. Phys. Lett. **51**, 472 (1987).
5. S. Kinoshita, K. Morito, F. Koyama, and K. Iga, Electron. Lett. **24**, 699 (1988).
6. A. Ibaraki, K. Kawashima, K. Furusawa, K. Ishikawa, T. Yamaguchi, and T. Niina, 11th IEEE Int. Semiconductor Laser Conf. (29 August-1 September, 1988, Boston, MA), paper N-2.
7. M. Ogura, W. Hsin, M.-C. Wu, S. Wang, J.R. Whinnery, S.C. Wang, and J.J. Yang, Appl. Phys. Lett. **51**, 1655 (1987).
8. D. Botez, L.M. Zinkiewicz, L.J. Mawst, and T.J. Roth, 11th Int. Semiconductor Laser Conf. (29 August-1 September, 1988, Boston, MA), paper N-1.
9. K.O. Hill and A. Watanabe, Appl. Opt. **14**, 950 (1975).
10. H.A. Haus, Appl. Opt. **14**, 2650 (1975).
11. P. Szczepanski, J. Appl. Phys. **63**, 4854 (1988).
12. G. Björk and O. Nilsson, J. Lightwave Tech. **LT-5**, 140 (1987).
13. S. Wang, J. Appl. Phys. **44**, 767 (1973).
14. IMSL routine UMINF.

15. M. Usami, S. Akiba, and K. Utaka, IEEE J. Quantum Electron. **QE-23**, 815 (1987).
16. T. Kimura and A. Sugimura, Electron. Lett. **23**, 1014 (1987).
17. G.P. Agrawal, J.E. Geusic, and P.J. Anthony, Appl. Phys. Lett. **53**, 178 (1988).
18. J. Kinoshita and K. Matsumoto, 11th Int. Semiconductor Laser Conf. (29 August-1 September, 1988, Boston, MA), paper H-4.

Figure Captions

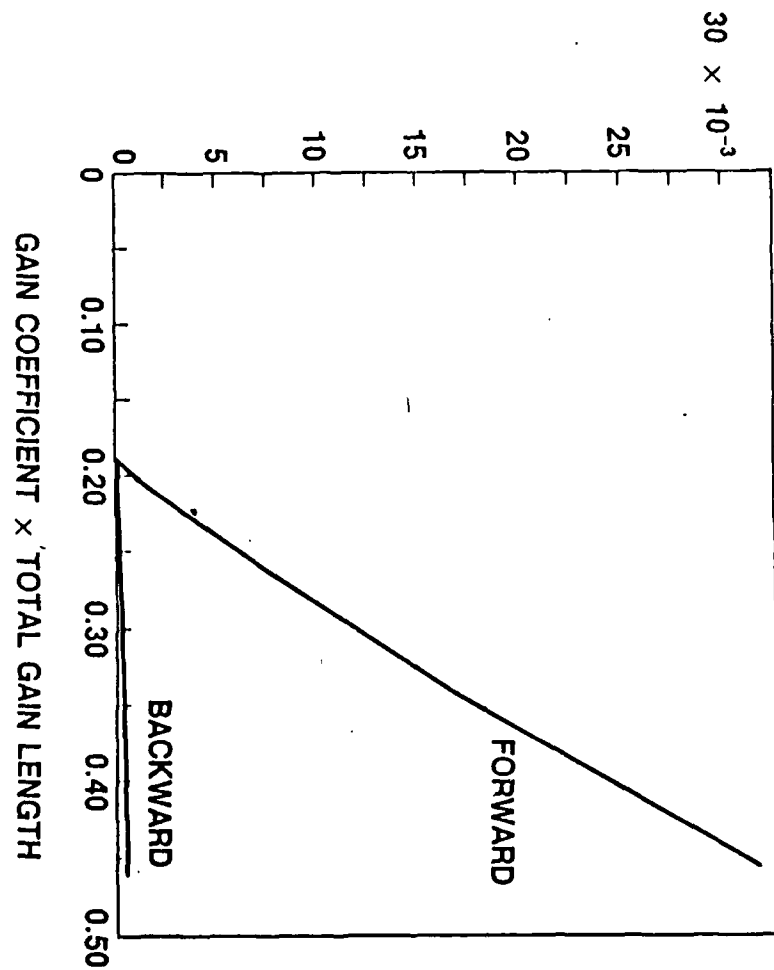
Fig. 1. Power output versus pumping parameter.

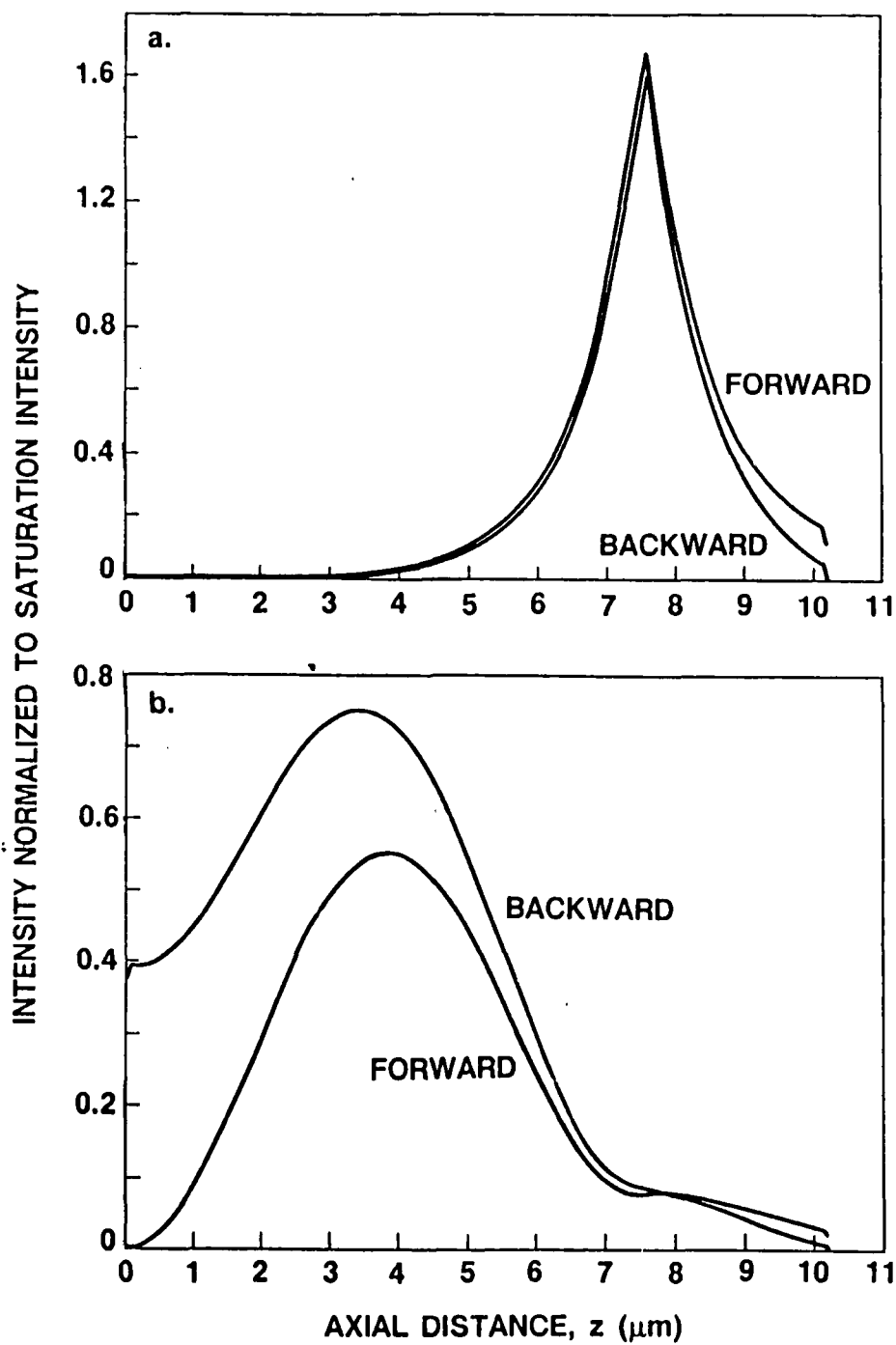
Fig. 2. Single phase-shift laser axial intensity distribution for the Bragg mode (a), and next higher order longitudinal mode (b) .

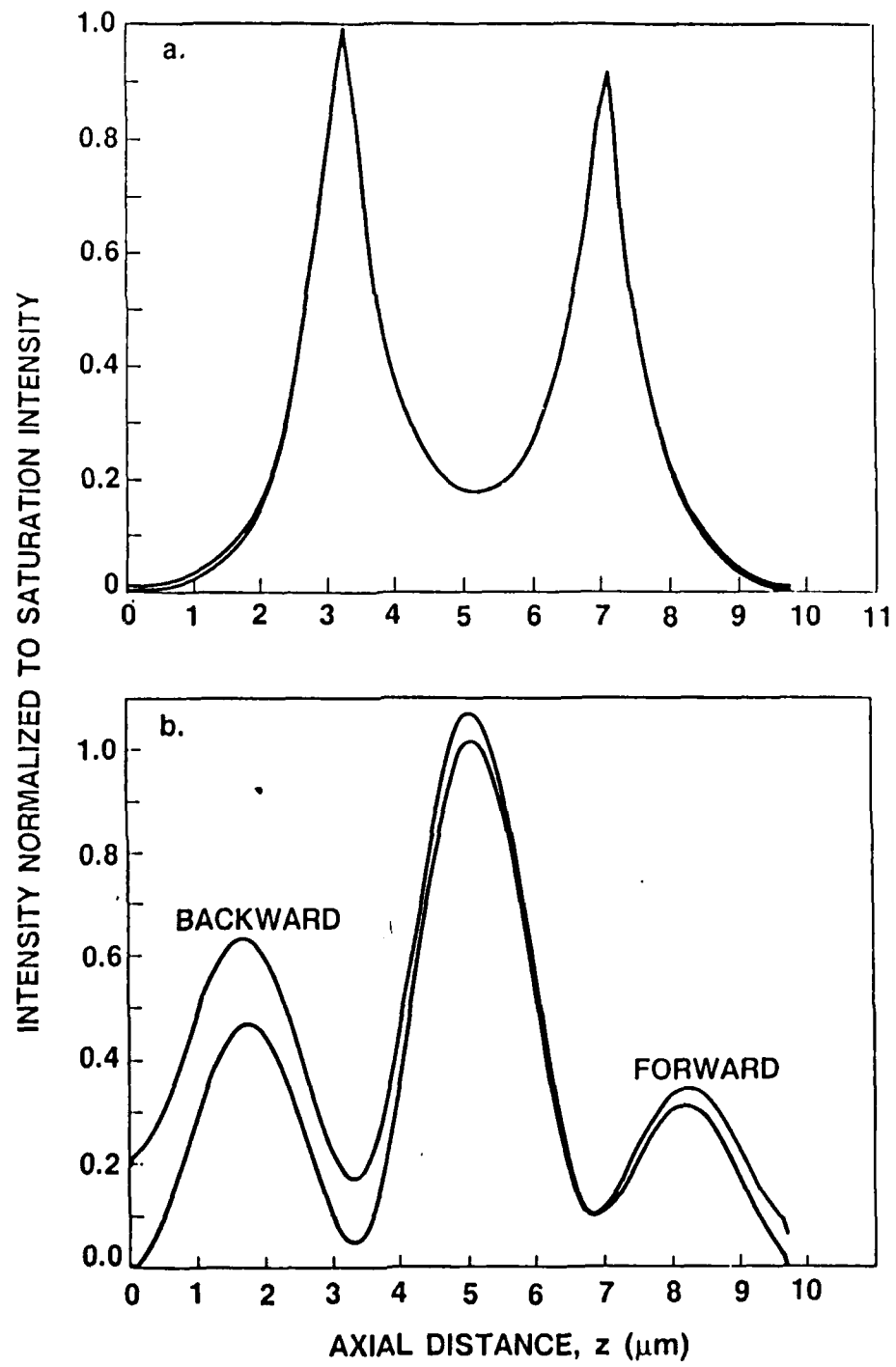
Fig. 3. Double phase-shift laser axial intensity distribution for the lowest order (a) and next to lowest order (b) axial modes.

Fig. 4. Axial intensity distribution of the fundamental mode of a DBR laser.

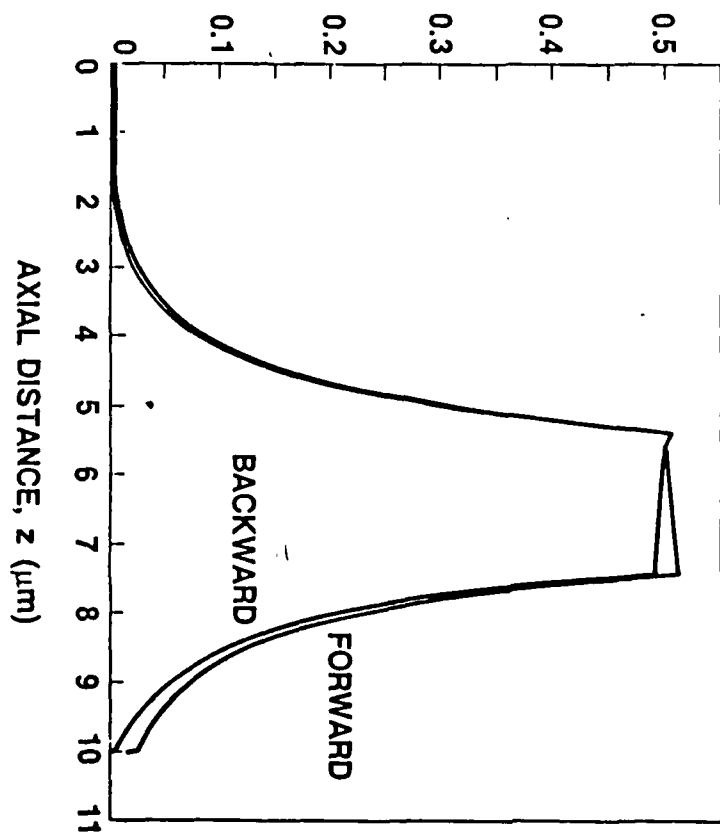
OUTPUT POWER NORMALIZED TO SATURATION POWER







INTENSITY NORMALIZED TO SATURATION INTENSITY



High modulation rate laser array for microwave optics

S. C. Wang and T. G. Dziura

Lockheed Palo Alto Research Laboratory
3251 Hanover Street, Palo Alto, California 94304

ABSTRACT

The structure and performance characteristics of a GaAs surface emitting laser (SEL) diode and a 2-D array of SELs is reported. The SEL has a very short optical cavity with a distributed feedback structure, and emits light perpendicular to the wafer surface. The laser shows low threshold current and has an estimated high frequency response of tens of GHz. A 2-D array of SELs with 6 x 16 elements was designed and demonstrated.

1. INTRODUCTION

A two dimensional (2-D) array of laser diodes is desirable for many applications including optical signal processing, optical interconnect, and optical computing. In particular, a 2-D array with high modulation rate capability and individually addressable control can have application in microwave optics such as an optically controlled phased array microwave system. In this paper we report on a new type of 2-D array made of surface emitting laser diodes we demonstrated earlier.¹ The SEL diode has many unique features including vertical emission, short optical cavity, low threshold current, and the potential for very high rate modulation. Most importantly, it can be scaled into a 2-D array easily without the rack and stack technique used in assembling conventional laser diode arrays.

In the following sections, we briefly describe the structure of this laser diode and present the key performance characteristics. The modulation response of the SEL diode is also discussed. Finally we illustrate the configuration and demonstration of a 2-D laser array made of the SEL diodes.

2. LASER DIODE STRUCTURE

A schematic sketch of the SEL is shown in Figure 1. The laser diode structure is a surface emitting type in which the light emission is perpendicular to the wafer surface instead of parallel to the wafer surface as in conventional edge emitting laser diodes. The SEL utilizes a transverse buried heterojunction structure to inject current laterally and to confine the injected carriers, and has a distributed feedback (DFB) vertical cavity type resonator. The active region is a multilayer structure which is made of multiple pairs of $\text{Al}_{0.3}\text{Ga}_{0.7}\text{As}$ and GaAs layers with quarter-wavelength optical thickness per layer. Typically, the multilayer structure has 20 pairs of these

thin layers at the top and 60 pairs at the bottom, and a GaAs phase shifting layer of about quarter-wavelength thickness in between. The phase-shifting layer allows the laser to lase at the Bragg wavelength of the multilayer structure. This multilayer structure also acts as a DFB optical cavity for the laser diode. The buried heterostructure with a transverse junction is formed by the N- and P-AlGaAs heterojunction cladding layers surrounding the active region.

Because of the lower turn-on voltage for the GaAs junction than that of the AlGaAs junction, the carriers are predominantly injected into the GaAs part of the active region. The radiative recombination of these carriers in the active region and the feedback effect of the DFB cavity produce vertical laser emission perpendicular to the junction and the wafer surface as shown in Fig. 1.

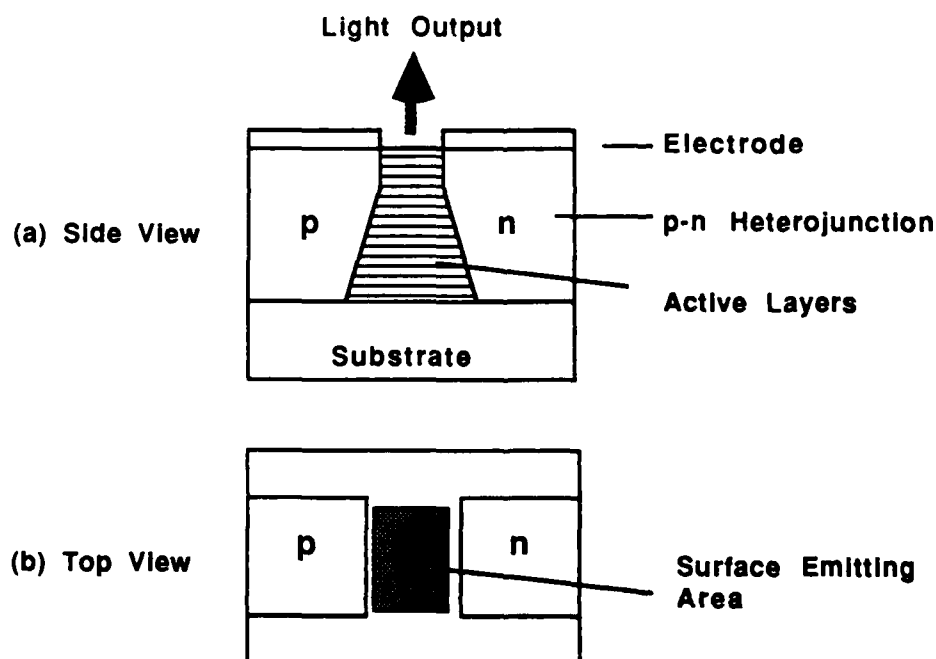


Figure 1. Schematic diagram of surface emitting laser diode

3. TYPICAL SEL PERFORMANCE CHARACTERISTICS

A typical SEL has a rectangular emitting area of about $3 \times 15 \mu\text{m}$ and an electrode on each side (p- and n-junction) providing for lateral current injection. With this type of structure and arrangement, the SEL can be tested as grown on the wafer without the cleavage process required for the conventional laser diodes. It also makes 2-D array formation and optoelectronics integration easier. The following performance characteristics

of SEL were measured on the wafer basis and under the normal room-temperature operation.

One of the distinct characteristics of this SEL is its emission pattern. Figure 2 shows a near-field emission pattern as viewed with a photomicroscope. The emission pattern is tightly confined within the rectangular emitting surface area, and is fairly uniform across the area as shown by the intensity profile. The far-field typically shows a nearly circular beam pattern with a beam divergence angle of about 8 deg. The laser emission wavelength of this SEL is typically around 884 nm near the GaAs bandgap.

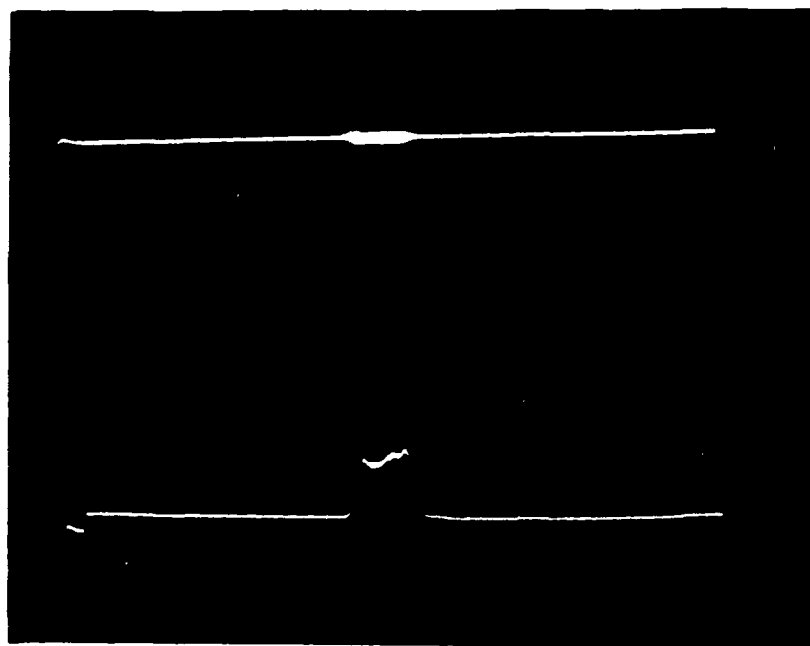


Figure 2. Near-field emission pattern

Another characteristic of this SEL that is very important for high speed modulation and optical signal processing is the relatively low threshold current operation requirement and linear light output dependence on the driving current. Figure 3 shows a typical light output versus driving current relation of the SEL tested under cw operating conditions. The light output increases linearly with the current up to 25 mA. This linearity is desirable for distortion free analog modulation. The output power of the SEL is about 90 uW at 25 mA for this case, a higher output of up to 0.5 mW was obtained at higher operating current. The threshold current is about 2 mA based on this data, which is substantially lower than the conventional laser diode. This low threshold current characteristic together with the short laser cavity configuration promise a very high speed modulation capability.

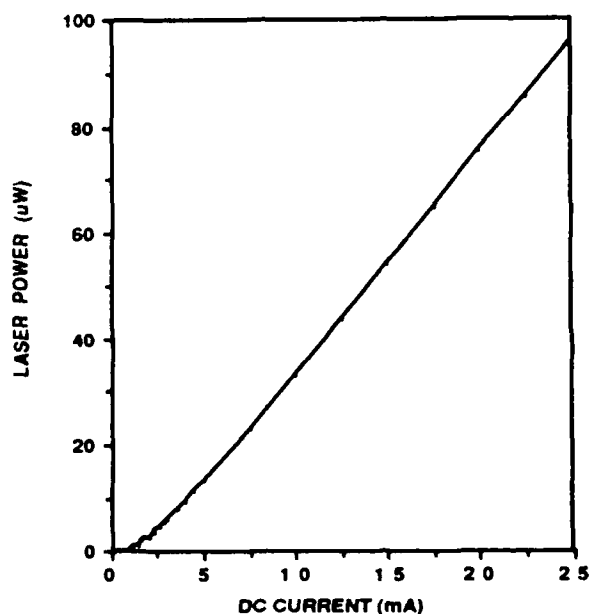


Figure 3. Light output vs driving current characteristics

4. MODULATION RESPONSE OF SEL

The modulation bandwidth of a laser diode is typically limited by the relaxation oscillation of the laser diode. The relaxation oscillation frequency, f , is related to the laser device parameters through the following approximate expression:

$$f = \frac{1}{2\pi} \sqrt{\frac{1}{\tau_e \tau_p} \left(\frac{J}{J_0} - 1 \right)}$$

Where τ_e and τ_p are lifetime of carriers and photons, J_0 is the threshold current density and J is the operating current density. For the SEL, the threshold current is about 2 mA and the cavity length is about 5 μm . If we assume the confinement factor is 0.5, internal loss is 10 cm^{-1} , a cavity of effective length 5 μm , and reflectivity of 70 %, then the photon lifetime is about 8×10^{-14} sec. For a carrier lifetime of 2 nsec (typical for GaAs), the relaxation frequency is about 25 GHz for an operating current of 10 mA. Therefore, high speed modulation can be expected from this type of SEL.

Preliminary investigation of the pulse response characteristics of the SEL diode was conducted, using a 50 nsec current pulse at 1 KHz repetition rate and a 40 psec rise time photodetector. Figure 4 shows the initial result of the light output response to the current pulse taken by a sampling scope of 20 GHz bandwidth. From this initial data, the rise time of the light emission seems to follow that of the current pulse, which has a risetime of about 5 nsec. A slight relaxation oscillation is observable on the light output response but is not very pronounced. Further investigation using faster rise time current pulse is planned. In addition, a new improved SEL structure to reduce the parasitic capacitance and series resistance is contemplated. Further results on this will be reported later.

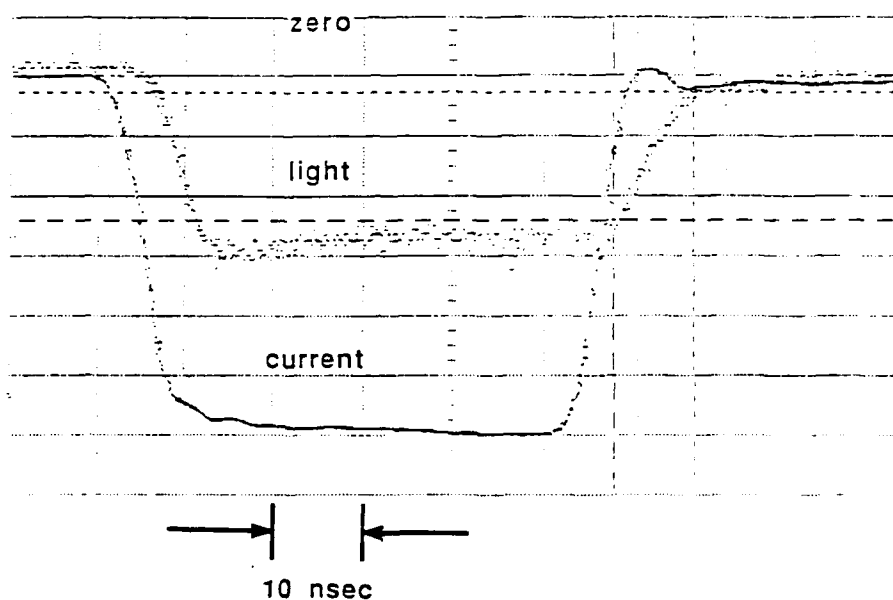


Figure 4. Response of light output to current pulse

5. SEL ARRAY CONFIGURATION AND EMISSION

Because of the planar structure and surface emission of SEL, formation of 1-D and 2-D array is relatively simple to accomplish. For example, a 3 x 3 of SEL array can be formed easily as illustrated schematically in Figure 5. By properly design of the masks for the array, the SEL array can be fabricated using the same sequence of processing step as the fabrication of individual SELs.

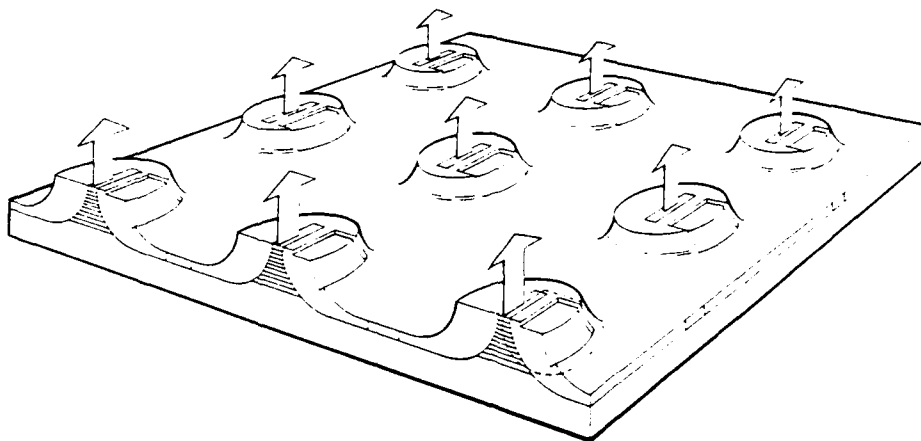


Figure 5. Schematic configuration of a 3 x 3 SEL array

Using the DFB type SEL diode structure described previously, we fabricated a number of arrays with 1-D and 2-D configurations. Figure 6 shows the photomicroscopic picture of a 2-D SEL array with 6 x 16 elements on a GaAs chip of about 2 mm x 2 mm. The light emitting area is adjacent to the bright shining rectangular region of Au electrode pads. The spacing between each SEL element is about 100 μm , limited by the electrode pad size which is about 80 μm x 80 μm . The light emitting area varies from 3 μm x 15 μm to 3 μm x 20 μm .

The array chip was mounted on a standard multiple pin chip carrier for testing. Figure 7 shows the emission pattern of the SEL array under cw operation. Because of the different emission area of SEL elements in the array and possible nonuniformity in the wafer and fabrication process, the threshold current for each SEL varies widely between a few mA to a few tens of mA. Therefore, the array emission pattern was taken by adjusting the driving current of each SEL to provide a nearly uniform emission intensity. As can be seen from the emission pattern, the overall array has a fairly good yield with about 95 % of the SELs in the array emitting radiation.

This array configuration allows each SEL element in the array to be addressed individually as demonstrated by the emission pattern shown in Figure 7 and provides possibility of modulating each SEL element independently. Furthermore, 2-D optoelectronic integration of the SEL with other electronic components such as a MESFET driver to provide very high speed operation is also possible for this type of SEL.

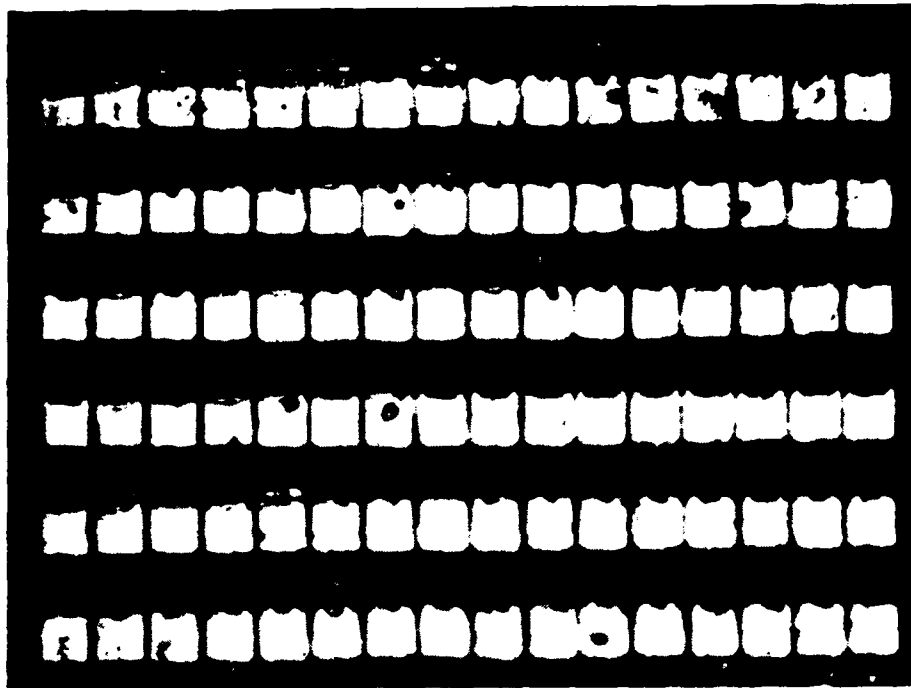


Figure 6. Photomicroscopic view of a 6 x 16 SEL array

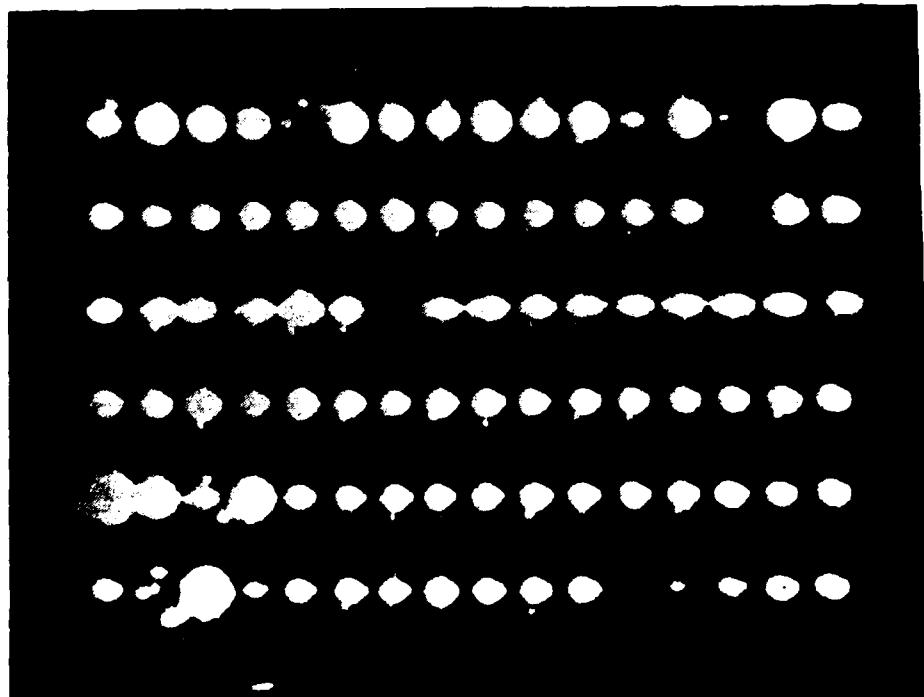


Figure 7. Emission pattern of a 6 x 16 SEL array

6. CONCLUSIONS

We report a new type of 2-D laser array made of SEL diodes. The SEL diode has a transverse buried heterojunction structure with a short distributed feedback laser cavity, and emits vertical radiation perpendicular to the wafer surface. The laser shows very low threshold current in the order of a few mA. These key features together with the preliminary data and estimation suggest that the SEL and its array can be modulated at a very high rate in the order of tens of GHz. We describe the design of 2-D laser array based on the SEL and demonstrate the operation of a 6 x 16 2-D SEL laser array. The result indicates that a 2-D SEL array is scalable and individually addressable. With many unique features of the SEL and 2-D array, we believe the SEL and SEL array will be very attractive for use in microwave optics, optical signal processing, and optical interconnect applications in the future.

7. ACKNOWLEDGMENTS

The authors wish to acknowledge the contributions of Professor Shyh Wang and Wei Hsin of University of California, Berkeley. They also appreciate the technical assistance of Patricia Marafino. This work is supported in part by the Office of Naval Research and the Rome Air force Development Center.

8. REFERENCES

1. W. Hsin, M. Ogura, Jean-Pierre Weber, S.C. Wang, J.J. Yang, M.C. Wu, Shyh Wang, and J.R. Whinnery, "GaAs/GaAlAs surface-emitting laser diode with distributed feedback optical cavity and transverse junction buried heterostructure", Proc. IEDM, pp 792-795, (1987).